UNIVERSITY OF CALIFORNIA,
IRVINE

Design, Build, & Analysis of a Multirotor Vehicle with Cyclic-Collective Pitch Control

DISSERTATION

submitted in partial satisfaction of the requirements
for the degree of

DOCTOR OF PHILOSOPHY

in Mechanical & Aerospace Engineering

by

Colin Alexander Sledge

Dissertation Committee:
Haithem E. Taha, Chair
Adjunct Professor Robert H. Liebeck
Professor Peter J. Burke

2021

DEDICATION

To my family, friends, and especially my parents, Brian & Shayne, for their continuing patience, support, and encouragement during every step of the way. I cannot thank you enough for everything you have done to help me and I owe all of my success to you.

A beautiful aircraft is the expression of the genius of a great engineer who is also a great artist.

Nevil Shute
No Highway

Contents

List of Figures

List of Tables

List of Symbols

β	blade flap angle
γ	Lock number
κ	induced power empirical correction factor
μ	rotor advance ratio, $V \cos \alpha / \Omega R$
ν	rotor downwash velocity in the near wake ft/s, structural deflection ft, fundamental flap frequency
Ω, ω	angular frequency, vibrational frequency, rad/s
ω_n	vibrational natural frequency, Hz
ρ	density, $slug/ft^3$
σ	rotor solidity
θ	angular deflection, blade feathering angle, blade angle as a control, rad
$\theta_{(\ )}$	control input, rad
θ_{tw}	linear twist rate, $\deg / R$
ζ	damping ratio
A	rotor disk area, ft^2
a	lift slope C_{l_α}
B	blockage ratio
c	damping constant, $lb_f/ft/s$
C_D, C_d	coefficient of drag
C_L, C_l	coefficient of lift
C_Q	coefficient of torque
C_T	coefficient of thrust

E elastic modulus, psi

G dimensional gravitational constant, ft/s^2

G shear modulus, psi

g non-dimensional gravitational constant $\frac{G}{\Omega R^2}$

I area moment of inertia, in^4

$I^*_{(\ )}$ non-dimensional moment of inertia

I_{xx} moment of inertia about x-axis, $slug - ft^2$

I_{yy} moment of inertia about y-axis, $slug - ft^2$

I_{zz} moment of inertia about z-axis, $slug - ft^2$

k, k_B, k_τ spring constant lb_f/ft, equiv. bending spring constant lb_f/ft, equiv. torsional spring constant $ft - lb/rad$

k_x, k_y, k_z non-dimensional radius of gyration for lateral, longitudinal, and directional axes, respectively

l rotor-rotor spacing, ft

$L_{(\ )}$ dimensional rolling moment derivative $\frac{1}{I_{xx}}\frac{\partial L}{\partial(\ )}$, $1/s$

M figure of merit

m mass, $slug$

M^* non-dimensional mass

$M_{(\ )}$ dimensional pitching moment derivative $\frac{1}{I_{yy}}\frac{\partial M}{\partial(\ )}$, $1/s$

$N_{(\ )}$ dimensional yawing moment derivative $\frac{1}{I_{zz}}\frac{\partial N}{\partial(\ )}$, $1/s$

P power, $Watts$

P structural load, lb_f

p angular velocity about x-axis, rad/s

q angular velocity about y-axis, rad/s

r angular velocity about z-axis, rad/s

R rotor radius, ft

T thrust, lb_f

T torsional load, $ft - lb$

u velocity along x-axis, ft/s

v velocity along y-axis, ft/s

W weight, lb_f

w velocity along z-axis, ft/s

X force along x-axis, lb_f

$X_{(\ )}$ dimensional x-force derivative $\frac{1}{m}\frac{\partial X}{\partial(\ )}$, $1/s$

Y force along y-axis, lb_f

$Y_{(\ )}$ dimensional y-force derivative $\frac{1}{m}\frac{\partial Y}{\partial(\ )}$, $1/s$

Z force along z-axis, lb_f

$Z_{(\ )}$ dimensional z-force derivative $\frac{1}{m}\frac{\partial Z}{\partial(\ )}$, $1/s$

Subscripts

0 collective control

s longitudinal cyclic control

c lateral cyclic control

Ω RPM control

ACKNOWLEDGMENTS

I would like to express the deepest appreciation and gratitude to my committee chair, Professor Haithem Taha. Professor Taha is one of the most hard working and driven people I know. He is not only extremely brilliant but also extremely caring. His door is always open if you need to talk about your latest idea or need some advice about life. As an advisor he recognised my optimal learning environment and gave me the freedom to explore my passions while providing me with guidance and steering me toward the goal. His passion for teaching and learning resonates with anyone lucky enough to work with him. I sincerely appreciate his patience and compassion.

I would like articulate my sincere admiration for Professor Robert Liebeck. Professor Liebeck has been a major advocate for me since he convinced me to attend graduate school in March 2012. It has been an honor to have him as a mentor and advisor. One of my favorite memories is visiting China with Professor Liebeck to deliver a presentation at a Boeing event. At some point on a rainy day Professor Liebeck, his wife, Cindy, and myself were stuck in a coffee shop where we had to chance to sit and talk. When I wanted to return to pursue a doctorate degree, Professor Liebeck gladly wrote me a recommendation and has continued to encourage me throughout. Professor Liebeck's stories show a remarkable career of deep passion for engineering and teaching. It has been an honor working with him.

I sincerely want to thank Professor Peter Burke for his involvement and guidance on the committee. During my first year at UC Irvine, I took a class with Professor Burke and quickly learned he is not only extremely talented, but also extremely kind. We would often see Professor Burke at the flying field testing his autonomous aircraft while we were testing ours. This demonstrates his passion for his research projects and teaches us how research can be very fun, engaging, & exciting.

I have immense respect and gratitude for Professor Kenneth Mease, my advisor during my Master's degree. After finishing my Master's degree 'too quickly', I asked if he would temporarily hold off passing me for the last units of research so I could stay at school one more year. I learned a tremendous amount in that last year and this time, he said I must obtain the degree. Knowing that I wanted to stay and letting me know that I could not put off graduating any longer, he developed a special role for me that allowed me to stay and work, at UC Irvine, with the senior design projects, for the next two years. At this point, I wanted to return to pursue a doctorate degree and he enthusiastically wrote me a recommendation letter. Without his advocacy and support, I would not be here today.

I would like to give a special thank you to Professor David Dimas who has been a great mentor and friend. Not only has he continued to request me as a teaching assistant, making sure that I have funding, but he has provided great support both professionally and personally. He has selflessly provided time helping me prepare for the qualifying exam, prepare research, and guiding me through the process. He has a passion for teaching that really resonates with all the students that take his classes.

In addition, I want to express extreme gratitude to Professor Liu (Jessica Chen) and Professor Hsieh (Ruohmei Hsieh) in the Chinese Language department. During my time as a doctorate student, they graciously and enthusiastically accepted me to be part of the Chinese languages courses. While this was not a requirement for my studies, it was exceedingly important for my development. Not only did this allow me to engage in my passion for learning Chinese, it helped me to incorporate a different way of thinking and learning into my daily life. Their compassion and support for me being part of the language class was, in no small part, one of the reasons I was able to make it through the doctorate program.

I would like to thank Professor John Larue and Professor Edwin Peraza Hernandez for sharing their passion with me as well as providing guidance and feedback during the qualifying examination.

I would like to thank The AIAA (American Institute of Aeronautics and Astronautics) for permission to incorporate our 2021 AIAA Scitech conference paper into this dissertation.

I would like to express gratitude to UC Irvine for helping provide funding as a teaching assistant during graduate school.

I would like to offer a special thank you to Moses Choi, Nathan Yeung, and Marlon Sevilla for assisting in aspects of manufacturing and flight testing. I would also like to extend a more broad thank you to everyone I had the chance to work with for the past 10 years at UC Irvine. Being a part of and helping advise numerous projects allowed me the opportunity to learn more than I could have ever imagined. I am extremely lucky to have had a major role in the aircraft design lab at UC Irvine. This small lab has so much potential for not only designing and building great things, but vast potential for learning. Without this resource I could have never experimented with and learned the many skills that have led me to where I am now. I sincerely hope that there are others who will be fortunate enough to work with numerous exciting, passionate people and who will have to opportunities I had. It has been a unique experience that I would not trade for anything!

VITA

Colin Alexander Sledge

EDUCATION

Doctor of Philosophy in Mechanical & Aerospace Engineering **2021**
University of California, Irvine *Irvine, California*

Master of Science in Mechanical & Aerospace Engineering **2014**
University of California, Irvine *Irvine, California*

Bachelor of Science in Mechanical Engineering **2012**
University of California, Irvine *Irvine, California*

Bachelor of Science in Aerospace Engineering **2012**
University of California, Irvine *Irvine, California*

RESEARCH EXPERIENCE

Graduate Student Researcher **2016–2017**
University of California, Irvine *Irvine, California*

TEACHING EXPERIENCE

Teaching Assistant **2013–2021**
University of California, Irvine *Irvine, California*

REFEREED CONFERENCE PUBLICATIONS

Design and Flight Testing of a Multirotor Vehicle with Cyclic-Collective Pitch Control **Jan 2021**
AIAA Scitech 2021 Forum

ABSTRACT OF THE DISSERTATION

Design, Build, & Analysis of a Multirotor Vehicle with Cyclic-Collective Pitch Control

By

Colin Alexander Sledge

Doctor of Philosophy in Mechanical & Aerospace Engineering

University of California, Irvine, 2021

Haithem E. Taha, Chair

Multirotor vehicles are a common type of unmanned aerial vehicle typically consisting of fixed-pitch propellers, each attached directly to a single motor and each motor attached to a frame appendage. This study explores an alternative configuration where each rotor has actuators that can modulate blade pitch in both a collective and cyclic manner, in addition to varying the rotor RPM. While this type of configuration has potential performance benefits, it also has potential airframe vibration challenges. A flight test vehicle was designed and constructed. During flight testing, the vehicle encountered severe vibrations that caused multiple instances of airframe damage. Structural modifications of the frame helped to mitigate vibration issues with the fuselage but came at the cost of weight and reduced aircraft performance. A mathematical reduced-order model that couples the structural response of the airframe with the inherent aerodynamic damping of the rotors is developed. The results show that out-of-plane vibration modes more heavily damped than in-plane modes, making in-plane modes more susceptible to damage. This study also presents an active method of vibration attenuation, using excess control power due to the over-actuated nature of the configuration. This is not in lieu of, but in conjunction with passive methods of vibration attenuation, such as damping elements incorporated in the frame. Stability analysis of the vehicle shows that the stability characteristics are similar to convention rotorcraft. This over-actuated vehicle enjoys multiple control allocation strategies. The control allocation problem

is analyzed through the volume of the reachable set from each control allocation scheme. The control allocation analysis shows that the addition of blade pitch control significantly increases the size of the reachable sets of the vehicle, when compared to RPM control as the only method of control. While cyclic pitch only had a modest impact on the size of the reachable sets, it can be argued the cyclic-pitch control would be integral to expanded flight envelope operations, such as autorotation flight. Regardless of the commercialization of this exact configuration, this study builds intuition that can be extended to various multirotor aircraft designs.

Chapter 1

Introduction

Most multirotor vehicles are combinations of 4, 6, or 8 fixed-pitch propellers (rotors) driven by electric motors at the end of appendages or booms. The central frame holds the flight controller, propulsion battery, additional flight critical electronics, and payload. While the simplicity of the system is a highly appealing aspect of the design, introducing some complexity may be acceptable if the system can be more maneuverable and robust. The eVTOL (Electric Vertical Take-off and Landing) market is currently limited by electric battery energy density and a focus on system safety is paramount. In preliminary rotorcraft design, the designer realizes that disk loading, solidity, and airfoil performance govern the hover power. If the mission requirements do not require large segments of forward flight or speed constraints, then the trade offs become simpler. By reducing the disk loading, the rotorcraft induced power will also be reduced. Assuming the number of rotor blades and blade geometry remain fixed, the profile power can be reduced by operating the blades at a C_l where the section C_l/C_d is maximized. For a given amount of energy on board, lower power required increases the endurance of the aircraft. With fixed-pitch rotor systems, varying the RPM of the rotor is the only means of control for thrust and torque. This, in turn,

is the only means of control for the entire aircraft. Most multirotor vehicles feature fixed-pitch propellers and vary RPM for control. By introducing an additional degree of freedom for blade pitch change, the RPM and collective blade-pitch control the thrust. Different combinations of these control inputs can yield a similar output. This allows the possibility of choosing an 'optimal' combination of control inputs for different flight conditions, loading conditions, and desired flight maneuvers. Additionally, the blade pitch control can reduce control latency. Conventional rotorcraft generally do not use differential thrust for control, as multirotor configurations do, but rather by varying the blade angles at specific locations in the cycle of rotor's rotation. This cyclic control is the main means of pitch and roll control for the aircraft. Using this type of control for multirotor vehicles has the potential to expand the flight envelop and provide new control allocation schemes that can be beneficial for certain flight missions.

While this alternative configuration has some potential benefits, significant challenges exist in terms of airframe vibration, control allocation, and characterization of the stability and control of the vehicle. During testing, the vehicle sustained damage several times from severe airframe vibrations. Common multirotor frames have the rotors as the end of cantilever rods. This can act like a tuning fork and be susceptible to vibrations at multiple frequency. This is made especially challenging if the vehicle is operated at a spectrum of main rotor frequencies. The frame may also be sensitive to high-frequency control inputs from the flight controller for stability and control. The rotors have inherent aerodynamic damping that can affect the vibration characteristics of the airframe. The coupling of the rotor and structural members acts like a mass-spring-damper system and characterization of the system provides insight into what frame modes are sensitive to be excited during operation and what methods can be used to attenuate vibrations. Because the vehicle is over-actuated and there is the ability to provide forces and moments on multiple axes of the frame appendages, both passive and active vibration attenuation methods can be used. Developing the stability & control

characteristics of the single rotor can be extended the entire vehicle and provides a basis for active vibration attenuation.

This research aims to explore the new flight regime of auto-rotation and methods to overcome the engineering challenges required to make a stable and robust flight vehicle.

1.1 Multiple Helicopter Lift Systems

An early concept by Piasecki Aircraft devised "A multiple helicopter lift system of two or more helicopters of the conventional type normally operating independently that are rigidly connected together in a spaced relationship by structural beam members to form an integral unit with the rotor drive systems of the attached helicopters interconnected so that the engines of each of the interconnected helicopters rotate at the same speed, as do the rotors." [1]. This patent (US3656723) describes the various structural arrangements of both conventional helicopters and tandem rotor helicopters to provide a heavy cargo lift system. The patent also details control arrangement and control mixing necessary for these arrangements. The patent does not include details about vibration concerns, vibration attenuation, flight performance, or autorotation capabilities. The patent authors describe the heavy lift concept to be related to another patent from Frank Piasecki (US3008665) in which the rotorcraft configuration is supplemented by a lighter-than-air component for additional lift capabilities [11].

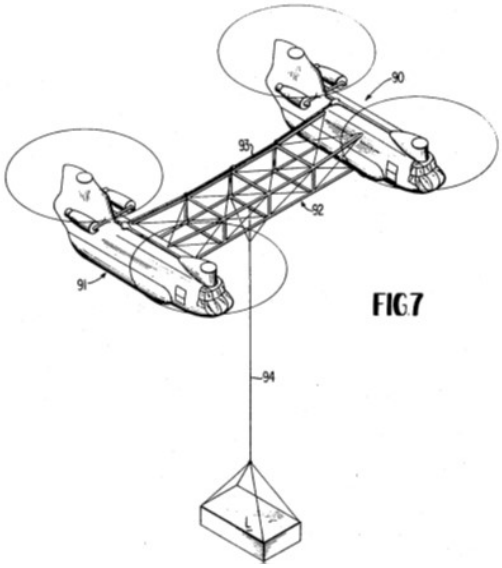

Figure 1.1: Piasecki multiple helicopter lift system [1]

These configurations appear to have evolved into another patent by Piasecki Aircraft (US4591112) which details a Vectored Thrust Airship using large conventional-type helicopters, without tail rotors, in a configuration described in the previous patents [12]. Figure 1.1 shows the configuration detailed in the patent. The control scheme is similar to the multiple helicopter lift system. This seems to have been realized as the Piasecki PA-97 Helistat (1986) which was constructed, and test flown as a heavy-lift contract to the US Navy. On July 1, 1986, the PA-97 Helistat took off and immediately after takeoff, the aircraft began vibrating violently, breaking apart, and killing one of the test pilots [13].

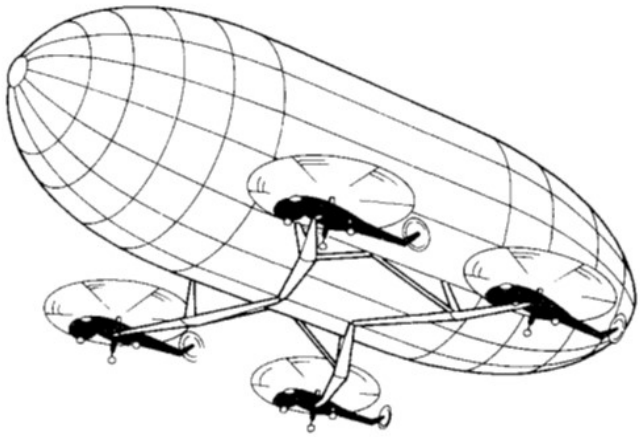

Fig. 1 Hybrid heavy lift airship—approximate configuration.

Figure 1.2: Hybrid Heavy-Lift Aircraft configuration [2]

The PA-97 Helistat test flight and failure can provide guidance for similar configurations and possible failure modes. As the NTSB report details, inadequate control and vibration were contributing factors to the incident. The PA-97 Helistat test flight and failure can provide guidance for similar configurations and possible failure modes. As the NTSB report details, inadequate control and vibration were contributing factors to the incident. Prior to the first flight, numerous NASA contracted studies were performed on the Hybrid Heavy Lift concept. In 1977, Brewer [14] examined the structural response due to collective input. In 1981, Browning [15] developed a comprehensive preliminary analysis on the design of a Hybrid Heavy Lift aircraft research vehicle. Venkatesan & Friedmann began assessing the aeromechanical-stability of a hybrid multirotor vehicle based on the configuration of the Piasecki PA-97 Helistat. In their first NASA report, Venkatesan & Friedmann [16] [2] [17] explore the coupling of the rotor mechanics with the

airframe structural dynamics. This provides a useful guideline for exploring the vibration characteristics of a multirotor with cyclic-collective pitch control and validation of results obtained. A two-part report by the authors [16] [17] details the methods described in the journal article and provides validation of the results. There are many similarities between Venkatesan & Friedmann and this current work, such as the decoupling of the model and approach to calculating the natural frequencies of the structure. An obvious difference is the configuration of the vehicle. The PA-97 is a hybrid rotorcraft-airship, shown in fig. 1.2 This changes the aircraft rigid body dynamics and some of the considerations taken for the structural analysis. For more information, the reader is referred to Venkatesan & Friedmann [2].

1.2 Variable-Pitch Quadrotor

An unpublished paper [18] from the University of Michigan, Ann Arbor discusses the viability and design of a multirotor hovering vehicle. According to the report, work on their flying vehicle named 'Hoverbot' began in 1992 and discussed the potential benefits of a such a configuration and the control systems required to make the vehicle flyable, with acceptable handling qualities. Interestingly, their configuration is built up from 4 model helicopters and used variable pitch for control. The configuration was tested, in hover, in a test apparatus that constrained the vehicle from translation. The report does not detail any more information regarding the flight characteristic or vibration issues.

In 2016, Pang, Peng, Lin, and Chen [3], from the National University of Singapore (NUS), designed and developed a large variable-pitch quadrotor, with the goal of substantially increasing the endurance of multirotor vehicles. The design incorporated variable-pitch rotors and an internal combustion engine as opposed to batteries and electric motors to benefit from the high energy density of fuel. Additionally, large main rotors with variable-pitch

would reduce the power required. Variable-pitch would allow the blades to operate at the best C_l/C_d for different flight conditions and rotor RPM, allowing for a larger operating envelope. One significant challenge of the project was the development of the drivetrain with the centrally located powerplant. Flight testing showed significant airframe vibrations which prohibited the validation of endurance estimates.

Author Pang Tao contacted Sledge, after publication of [19], indicating that work on the project continued after the paper was published. A video was shared that shows a full flight of the vehicle near the predicted endurance time. Pang indicated that vibrations were not a significant problem for the test flight. It was not clear what changes were made; however, the video shows a similar airframe to what was published in the paper. The source of this video and more details regarding the work are found in Pang [20]

Figure 1.3: NUS Variable-pitch quadrotor [3]

In 2018, Wu [21] detailed the design of a large variable-pitch quadrotor similar to the vehicle from NUS. The design builds upon earlier work at OSU from 2013 - 2014. Wu indicates that the test vehicle from 2013 suffered vibration problems similar to the NUS vehicle. Wu's work also suffered vibration problems during early testing, damaging drivetrain components. Premature wear of the gearboxes prohibited significant endurance testing and validation of predicted performance.

1.3 Variable-Pitch versus Fixed-Pitch Quadrotor

In 2012, Cutler [22] compared the flight characteristics of fixed-pitch versus variable-pitch quadrotors, specifically for agile flight. For the experiment, Cutler designed and developed a small-scale quadrotor with variable pitch rotors. The author compared the thrust response to changing RPM versus changing the blade pitch, including the actuator response. The results showed that the variable-pitch vehicle could follow a reference trajectory with much lower error when compared with the fixed-pitch variant. The research also showed the variable-pitch vehicle performing numerous aerobatic maneuvers, included stable, sustained inverted flight. The author mentions vibrations beyond certain RPM thresholds but states that vibration problems were not significant during operations. Video of this flight shows stable and agile flight [23]. A similar analysis was performed by Porter, Shirinzadeh, & Choi [24]. The researchers confirm that variable-pitch rotors can vary thrust more rapidly than fixed-pitch rotors. Interestingly, this was more pronounced when the commanded input is to reduce thrust. The fixed-pitch rotor must reduce RPM to reduce thrust, however, a variable pitch rotor can modulate the blade angle while maintaining RPM. Another interesting result is that the researchers state the control bandwidth increased with increases in rotor RPM. This would be important to consider in developing a control allocation strategy.

1.4 Non-Planar and Over-Actuated Vehicles

In 2011, University of Manchester developed a non-planar vehicle to achieve "... fully independent control of both vehicle position and orientation in three-dimensional space, at least during hover or slow forward flight (within the saturation limits of the actuators)" [25]. This configuration provides the possibility of increased control authority and manipulation of the vehicle orientation. As the authors discuss, this additional control comes at a weight

penalty that could significantly impact the utility for specific missions. The authors also note that vehicles with cyclic pitch control of the rotors were not considered in this study. A similar vehicle configuration was developed in 2018 by Brescianini & D'Andrea from ETH Zurich [4]. Their vehicle used "reversible fixed-pitch rotors that can generate positive and negative thrust, enabling the vehicle to independently control its thrust and torque in all three dimensions." Their test vehicle proved successful. The authors noted that the enhanced control came at a cost to the hover efficiency and increased vehicle mass. In 2013, a researcher at the Norwegian University of Science and Technology developed a multirotor with collective and cyclic controllable rotor heads [26]. In addition, the design allows for the frame arms to be rotated about their axis. Despite the addition of the cyclic and collective control, the thesis mainly focuses on the tilt-rotor function of the vehicle. Numerical simulations performed to assess the performance of the configuration address the maximum forward speed using body tilt angle, rotor tilt angle, and blade tip flapping angle. This, however, lacks the actual physics of the vehicle and dynamics of the system, so the validity of the results seems questionable. A prototype vehicle was built but never flight tested, however one rotor assembly was bench tested to measure the maximum thrust capability. The author notes that the test article had vibration problems.

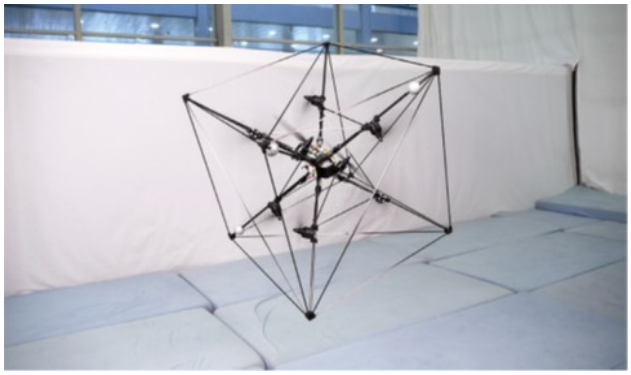

Figure 1.4: ETH Zurich Omni-directional multirotor vehicle [4]

In 2014, researchers at University of Toledo conducted an analysis of an over-actuated quadrotor vehicle with tilting frame arms [27]. The motivation behind this design was to utilize over-actuation to create a "... design [that] makes the quadcopter a fully-controlled system which can track any arbitrary trajectory." A prototype vehicle was not built; however, simulations were performed to assess the performance. This study focuses on trajectory fol-

lowing as opposed to the flight speed. This configuration was also explored by Segui-Gasco et al.[28]. They address control allocation and the 'fault tolerance' during a rotor failure. Their analysis shows the possibility to 'reconfigure' the vehicle to maintain control during system failures.

Figure 1.5: KU Leuven Over-Actuated Vehicle [5]

In 2018, researchers at KU Leuven developed an over-actuated quadrotor vehicle [5]. As the authors state, "Conventional quadcopters are under-actuated mechanical systems possessing less control inputs than Degrees of Freedom (DOFs)." This vehicle allows tilting of each of the rotors in two directions; the frame arm has an axial degree of freedom and the motor mount itself can tilt toward or away with respect to the vehicle vertical axis. Simulations of the over-actuated vehicle were performed showing enhanced maneuverability. The researchers then built a prototype and compared the mission performance of the vehicle using only RPM variations for control as a conventional multirotor with the actuation of the tilting mechanisms. The vehicle was able to follow a proposed flight path with greater precision, making sharper turns and negotiating through obstacles with smaller clearances. While it was not included in this research, the team proposes the ability for this over-actuated platform to be more tolerant to the loss of one or more of the rotors when compared with a conventional quadrotor vehicle.

1.5 Control System Methods

In 2014, Muller & D'Andrea presented a method to address the robustness of a quadrotor vehicle. Instead of focusing on the physical configuration, the researchers developed a control

strategy that allows the flight controller to reconfigure itself in the case of loss of a propeller or thrust from one or more of the rotors [29]. In their experiment, the propeller is either removed or allowed to come off in flight. When this occurs, the vehicle enters a spin around its body axis. The controller then provides cyclic inputs to control the vehicle. The vehicle position can be controlled with remarkable precision and perform a safe landing. Video of the experiment shows the vehicle take off, translate, and land with one and two propellers removed [30]. Lanzon, Freddi, & Longhi[31] performed a similar analysis and arrived at a similar conlusion as Muller & D'Andrea. Lanzon, Freddi, & Longhi also discuss constraints such as thrust required to maintain adequate control with the loss of a rotor. While this is a remarkable achievement, it would likely prove to be an unsuitable method if the vehicle were carrying a payload that is sensitive to high accelerations.

1.6 Patents

In 2015, Vladimir Kvitnevskiy filed for a patent for a method to control multirotor vehicles using collective and cyclic controls [32]. The main claims are a vehicle that uses collective and cyclic control for enhanced robustness, control, and to provide the ability to autorotate. While this appears to be identical to the current research being explored in this paper, there is no evidence that any prototype vehicle was designed and tested. The patent merely lays out the claim of the ability but provides few details to accomplish this task. It should be noted that the inventor does not mention vibration, which would likely suggest that a prototype was not built and tested. In 2019 the US patent application was withdrawn and in 2020 the European patent application was withdrawn for this patent.

In 2017 a patent was filed for the use of collective pitch for multirotor autorotation [33]. This patent provides few details except for the claim that collective pitch can be used on

multirotor vehicles for autorotation. Similar to patent [32], there is no evidence of a prototype or testing of this vehicle.

1.7 Other Notable Works

In 2010, Joseph D'Angelo and Roberto Navoni developed a variable-pitch quadrotor vehicle powered by a small petrol engine [34]. Videos of system tests and flight show a successful vehicle. It should be noted that two test videos appear to show noticeable frame vibrations. In 2010, a video from National Cheng Kung University in Taiwan shows a successful autonomous flight of a variable-pitch quadrotor vehicle [35]. The vehicle is shown to perform aerobatics and a variety of other maneuvers.

In 2016, Curtis Youngblood's company, who build UAVs and other products related to the model helicopter hobby industry, developed a variable-pitch multirotor product, the Stingray 500 [6]. Flight demonstrations show a very stable and agile aircraft. It is not clear if this product is still available or if there are other similar products available, although the company alludes to a larger vehicle in development.

Figure 1.6: Curtis Youngblood Stingray 500 [6]

1.8 Dissertation Outline

The literature review presented in this section describes the current state of research into multirotor configurations. It is clear from this review that little research has be conducted into multirotor vehicles with collective and cyclic pitch controls, especially in terms of airframe vibration and the ability for the vehicle to autorotate. A potential benefit of a collective cyclic-controlled multirotor vehicle is the ability for the aircraft to autorotate in the case of powerplant power loss. While claims have been made, in patents and research alike, as to the ability of a variable pitch multirotor and a collective-cyclic control multirotor to have the ability to autorotate, little research or experimentation has been conducted in this area. This gap in research in the field needs to be filled to provide researchers and designers the necessary information to develop state of the art multirotor vehicles. Below are areas of research that remain insufficiently answered.

- Characterization of stability & control for a multirotor aircraft with cyclic-collective pitch control
- Aeroelastic analysis of a cyclic-collective pitch control quadrotor
- The effect of cyclic pitch control on controllability and performance of a quadrotor in autorotation

The following is a summary of the mutlirotor configurations, listing potential advantages and disadvantages of each.

1.8.1 Chapter 2

Chapter 2 explores the design of the flight test vehicle and the subsystems. The first section of the chapter discusses flight testing of a conventional multirotor vehicle and the work to

Table 1.1: Multirotor Control Scheme Summary

Control Type	**Advantage**	**Disadvantage**
Fixed-Pitch Rotors	-Mechanically simple -Simple controllers and algorithms -Well understood -Scalable	-Poor system robustness -Reduced adaptability -Cannot autorotate
Variable-Pitch Rotors	-Can adjust blade pitch for more optimum operating conditions -More robust -Potential autorotation capabilities	-Added mechanical complexity -High Vibrations -Yaw control from rotor torque may limit autorotation control
Non-Planar Rotor Configurations	-Excellent maneuverability -Novel configuration layouts for unique requirements -Mechanically simple	-Reduced performance -Not robust -Cannot autorotate
Over-Actuated Vehicles	-Increased maneuverability -Increased robustness	-More mechanically complexity -Reduced performance -Cannot autorotate
Control System Adaptability	-Very robust -Mechanically simple -Scalable	-Loss of performance -Potential payload damage
Collective-Cyclic Control Rotors	-Can adjust blade pitch optimum operation -Increased robustness -Increased maneuverability -Can autorotate	-Very mechanically complex -High vibrations -Increased weight and structure -Unproven

understand and maximize the endurance of a multirotor, which was the precursor for this project. The flight controller firmware was modified for the control allocation of this vehicle. The current vehicle only used collective and cyclic pitch for control, however, a variety of control allocation arrangements are available due to the over-actuated nature of the vehicle. Structural members of the airframe were tested to calculate the structural properties necessary for vibration analysis. A finite element analysis was used for tuning and validation

of the physics model. Difficulties incorporating aerodynamics damping into the finite element modal analysis prompted development of a low-order physics model to determine the vibration characteristics of the airframe with aerodynamic damping considered.

1.8.2 Chapter 3

Chapter 3 discusses flight testing of the vehicle. After construction and testing of vehicle subsystems, initial test flights were performed to tune the flight controller gains and determine the handling qualities of the vehicle. While the vehicle had many successful test flights, there were also significant challenges with vehicle vibration. The first instance of damage due to vibrations occurred when one of the strut braces de-bonded from the frame. After a minor repair, the vehicle had many successful flights with incident, however, a crash led to a chain of events that uncovered severe underlying vibration issues. After major damage was sustained, a vehicle redesign led to another instance of major damage. While further redesign eliminated some of these issues, significant vibrations still exist that degrade the flight performance.

1.8.3 Chapter 4

In order to gain insight into the vehicle vibration characteristics and propose solutions to mitigate some of the impacts of vibration, Chapter 4 first examines the impact of incorporating aerodynamic damping into the modal analysis of the airframe. A helicopter has naturally occurring aerodynamic damping from the rotor and airframe. This aerodynamic damping has an influence on the vibration characteristic of the vehicle. A code was developed to calculate these stability and control derivatives that are then used in the physics model. The validity of the code is compared against published data for a variety of rotorcraft. The physics model transforms the effective spring constants of the structural members and

the aerodynamic damping matrix into a mass-spring-damper model to predict the natural frequency and vibration transmissibility of the airframe. The results are then compared against the flight test data. The formulation of the system into the mass-spring-damper model allows the analysis of both passive and active vibration mitigation methods. Because the vehicle is over-actuated, a feedback control system may be implemented to modify the vibration characteristics of the frame through rotor inputs.

1.8.4 Chapter 5

Chapter 5 explores the stability & control of the entire vehicle. The stability & control derivatives, presented in Chapter 4 are extended to the complete vehicle configuration and an assessment of the vehicle hovering characteristics discusses. Chapter 5 goes on to explore the control allocation for the vehicle. Because of the over-actuated configuration, there are several methods to control the forces and moments on each axis, i.e. cyclic pitch, collective pitch, and RPM control. By analyzing the reachable sets of the vehicle, for each configuration, the various control schemes can be compared with one another to determine which have the potential to maximize the reachable set, which can provide insight into the maneuverability and control power required for the vehicle.

1.8.5 Chapter 6

Chapter 5 provides conclusions and recommendations for further work on the vehicle. Flight testing will be critical to validating stability & control derivative estimates and developing control allocation arrangements. Many of the vibration characteristics can be modified and tuned by reexamining the vehicle frame and rotorhead design. To be able to implement vibration attenuation methods and expand the vehicle flight envelop, the flight control system needs to be modified and expanded, coupled with a suite of sensors. The end goal of

the project is to explore alternative configurations for multirotor vehicles and enhance the understanding of well-established configuration.

Chapter 2

Vehicle Design & Construction

2.1 Flight Performance

A premier requirement of unmanned aerial vehicles (UAVs) is endurance and is often a limiting factor in the utility of small UAVs, especially for eVTOL aircraft. The energy density of current lithium polymer batteries is significantly lower than liquid fuels. While the energy density of the current state-of-the-art batteries continues to increase, aircraft designs need to address vehicle power consumption. Changes to the airframe configuration may lead to reduction in power required and increase flight endurance. Gatti, Giulietti, & Turci[36] addressed the maximum endurance of a multirotor vehicle with fixed-pitch rotors. In their analysis they assess the impacts on performance from adding addition battery capacity to an existing airframe. They show that there are diminishing returns from simply adding more battery weight to increase endurance and that careful analysis or the requirements, early in the design, is critical to maximizing endurance.

My experience has shown that, when not taken into consideration in the design, the frame configuration can significantly reduce flight time and, if severe, may render the vehicle un-

flyable. The area of the frame in the rotor wake and the shape of the appendages create a download on the frame during hover. In flight, these features increase the parasitic drag of the vehicle. Assuming the hover flight condition to start, the power required to hover is as follows:

$$P = \kappa T \sqrt{\frac{T}{2\rho A}} + \rho A (\Omega R)^3 (\sigma c_{d_0}/8) \tag{2.1}$$

This can be broken up into the induced power and the profile power:

$$P_{induced} = \kappa T \sqrt{\frac{T}{2\rho A}} \tag{2.2}$$

$$P_{profile} = \rho A \left(\Omega R\right)^3 \left(\frac{\sigma c_{d0}}{8}\right) \tag{2.3}$$

According to Johnson, "...the figure of merit compares the actual rotor performance with the performance of an ideal rotor, which has only the inescapable induced power loss." [37].

$$M = \frac{T\sqrt{\frac{T}{2\rho A}}}{P} \tag{2.4}$$

For hover $T \approx W$, the figure of merit may have a value around 70%. This suggests that the induced power is the significant contribution to the total hover power. The induced power is sensitive to the thrust required and the disk loading T/A. Additionally, the downwash velocity in the near wake of the rotor is proportional to the disk loading:

$$v_h = \sqrt{T/2\rho A} \tag{2.5}$$

To build a metric that can apply in the design phase and to analyze different vehicles, it is useful to look at the power loading of the vehicle. Fixing, for a moment, the figure of merit, the power loading will be:

$$\frac{P}{T} = \frac{1}{M}\sqrt{T/2\rho A} \tag{2.6}$$

This can be rewritten as:

$$\frac{P}{T} = C\sqrt{T/2\rho A} \tag{2.7}$$

where C an empirical value we can find through testing. This will include information about the rotor geometry, and non-ideal losses. Assuming a disk loading of: $T/A = 1\left[\frac{lb}{sq.\ ft}\right]$ the value for C can be found for the base line case. The vehicle used in this experiment has a disk loading of one pound per square foot and required $\approx 53\ watts$ per pound to hover.

$$\frac{P}{T} \cong \left(\frac{P}{T}\right)_0 \sqrt{\frac{cT/A}{(T/A)_0}} \tag{2.8}$$

$\left(\frac{P}{T}\right)_0 \cong 53\frac{watts}{lbf.}$ at a disk loading, $(T/A)_0 = 1\frac{lbf}{sq.\ ft}$ This makes it easy to extend to new vehicles of similar frame and rotor configurations through the relation:

$$\frac{P}{T} \cong \left(\frac{P}{T}\right)_0 \sqrt{T/A} \tag{2.9}$$

To conduct the experiment, the aircraft was first flown without the blockage additions. The blockage is cataloged as a percentage of the disk area that the rotor overlaps with the feature. For the baseline frame, the blockage is estimated to be approximately 1%. To predict the new power loading as a function of the downstream blockage, the features below the rotor are assumed to produce a vertical drag, and at this time, it will be assumed that the features

will not affect the inflow to the rotor. Johnson provides some guidance for this method.

$$D = C_D S \frac{1}{2} \rho V^2 \tag{2.10}$$

In the far wake of the rotor, the downwash velocity is:

$$w_h \approx 2v_h = 2\sqrt{T/2\rho A} \tag{2.11}$$

Substituting eq. 2.10 into eq.2.11:

$$D \approx C_D S \frac{T}{A} \tag{2.12}$$

The C_D used can be found for many common shapes or can be found experimentally. The C_D used in this analysis was assumed to be $C_D \approx 1.4$ corresponding to the shape of the boom and plates beneath the rotors. To find the new power loading, a new parameter, which will be referred to as the apparent disk loading, is introduced:

$$\left(\frac{T}{A}\right)_{apparent} \tag{2.13}$$

This parameter is found by finding an apparent disk area:

$$A_{apparent} = A\left[1 - BC_D\right] \tag{2.14}$$

The apparent disk area is found by subtracting the blockage ratio, B, multiplied by the drag coefficient of the features in the wake, C_D, from the true disk area, A. This shows that any blockage will effectively reduce the disk area, increasing the disk loading. The new power loading can be found from the procedure shown previously.

Table 2.1: Power Loading vs. Rotor Wake Blockage

$Blockage, B$ [% Disk Area]	$\left(\frac{P}{T}\right)_{Theoretical}$ $\left[\frac{watts}{lb.}\right]$	$\left(\frac{P}{T}\right)_{Measured}$ $\left[\frac{watts}{lb.}\right]$
1	53	52
20	63	64
40	80	88
60	134	144

The results of the tests are shown in Table 2.1, Fig. 2.1, Table 2.2, and Fig. 2.2. The deviations at high blockages are likely due to non-linearities with the rotor in-flow and voltage sag in the propulsion battery.

Table 2.2: Power Loading vs. Apparent Disk Loading

$\left(\frac{T}{A}\right)_{Apparent}$ $\left[\frac{lb.}{sq.ft}\right]$	$\left(\frac{P}{T}\right)_{Theoretical}$ $\left[\frac{watts}{lb.}\right]$	$\left(\frac{P}{T}\right)_{Measured}$ $\left[\frac{watts}{lb.}\right]$
1.06	53	52
1.48	63	64
2.44	80	88
6.76	134	144

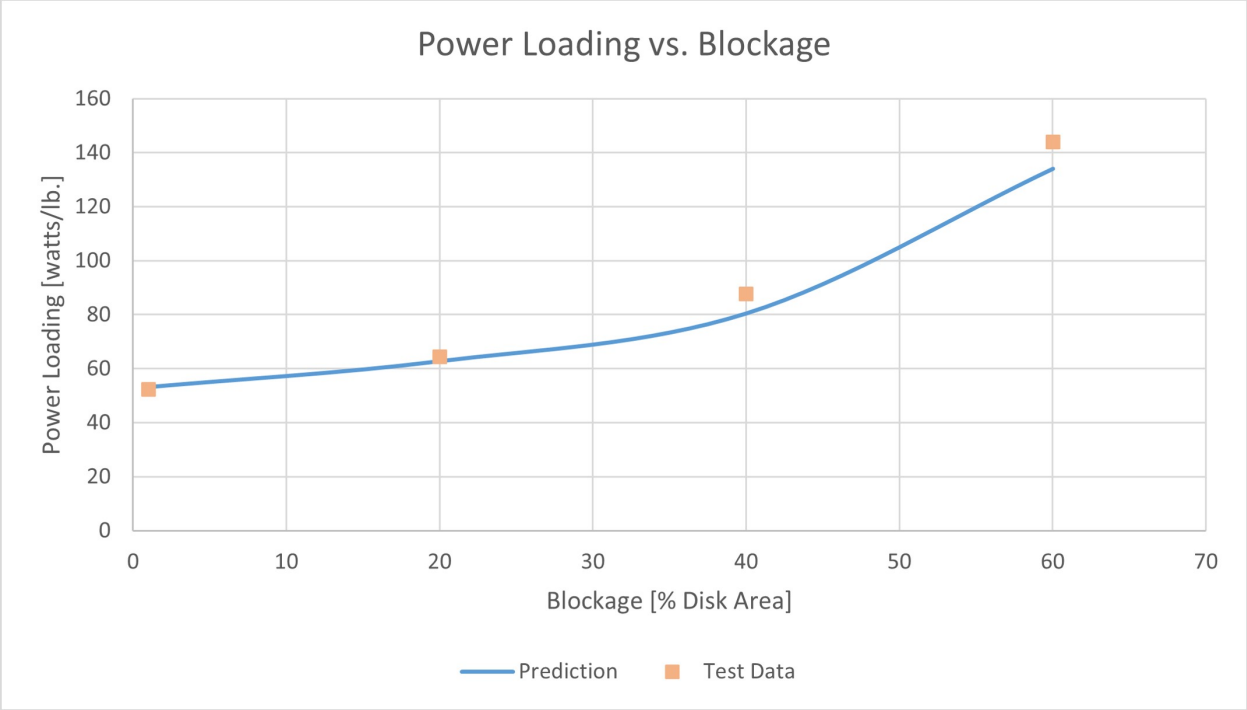

Figure 2.1: Power Loading vs. Rotor Wake Blockage (Theoretical & Experimental)

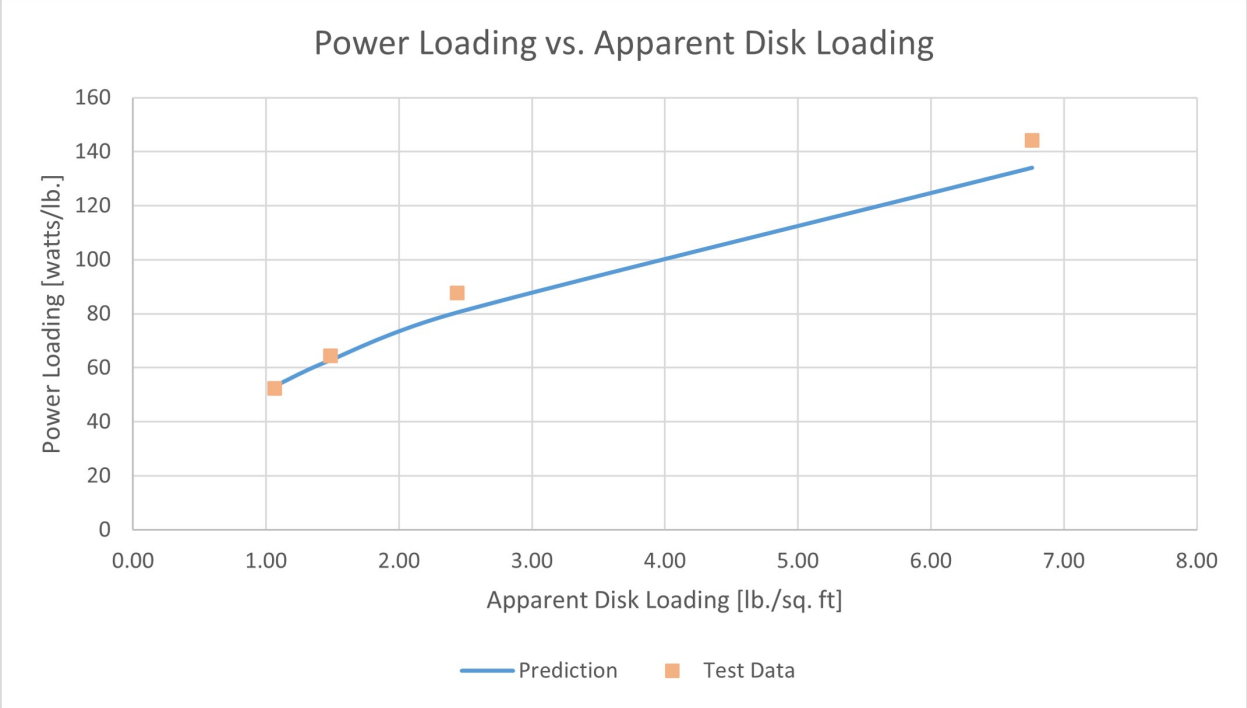

Figure 2.2: Power Loading vs. Apparent Disk Loading (Theoretical & Experimental)

2.2 Flight Vehicle Design

The initial conceptual design of the quadrotor vehicle had 54-inch diameter rotors, but cost constraints and space constraints prohibited this size of vehicle. The vehicle design was constrained to use as many commercially available parts as possible with the least number of modifications necessary. This significantly limited the available helicopters used for the main rotors. Additionally, three-bladed rotors were chosen to reduce vibrations, as a larger number of blades generally reduces vibrations [38]. Lower frequency structural harmonics are also less likely to be excited as a dominant source of vibrational energy occurs at $N \cdot RPM$, where N is the number of blades.

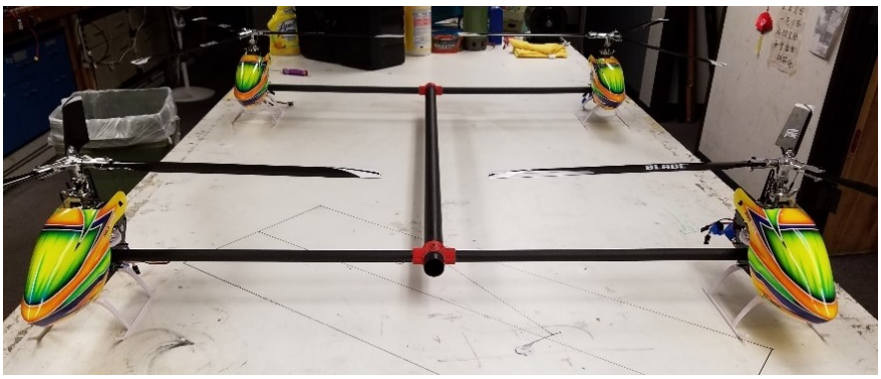

Figure 2.3: Initial Frame concept (without strut-braces)

The H-frame configuration was chosen to use existing features on the helicopter frame for secure, structural mounting and to keep the swashplate in the natural flight position to simplify the control scheme in the flight controller. The main fuselage tube and frame arm tube diameters were chosen based on size, stiffness, and cost, but a detailed analysis was not performed a priori. The initial frame design, shown in Fig. 2.3, was a simple 'H-shape' with cantilever arms and no arm strut-braces. With the rotor mechanics and brushless motors installed on the frame, it was immediately apparent that the frame was too flexible, and the low-frequency vibrational modes of the frame may be excited in flight. Supporting the frame in the middle of the main fuselage tube and providing an impulse to the arm to excite the fundamental mode, the arms appeared to vibrate in the horizontal plane at an estimated

5-10 hertz. The frame was modified before initial testing by adding strut-braces from the main tube and connected to the frame arm approximately half of the arm span, as seen in Fig. 2.4. With these additions, the fundamental frequency was clearly much higher, but no further consideration or detailed analysis was performed as this stage.

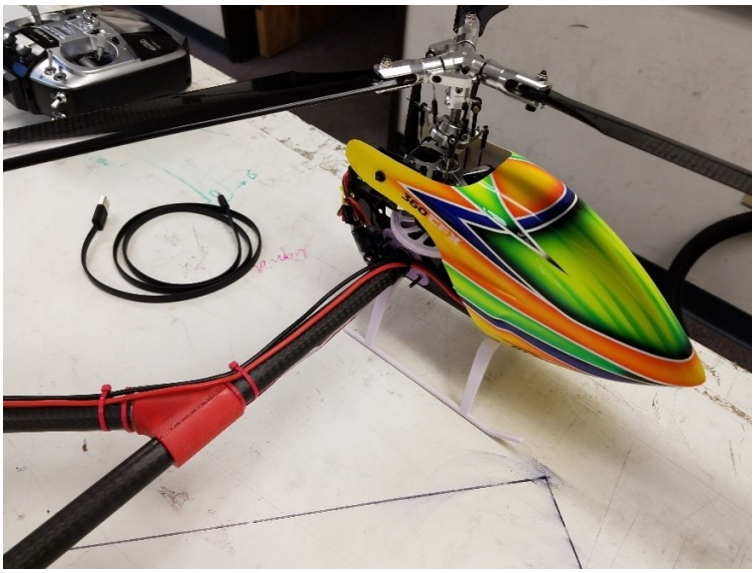

Figure 2.4: Strut-Brace Structure & Rotor Integration

The flight controller is the Pixhawk 2.1 with modified firmware. For a new aircraft control scheme, the user must modify the aircraft model files and reinstall the firmware. The control scheme was developed based on Table 2.3. Initially, only cyclic-pitch control was used for vehicle pitch, roll, and yaw control. Collective-pitch control was use for altitude control, while the RPM was held constant. The RPM can be mixed with collective-pitch control in designated flight modes as determined by the pilot, otherwise, the RPM is held at a constant value. This is accomplished by setting the throttle value as percentage of full throttle from the pilot's transmitter or setting the value in the motor controller and using the embedded governor function to maintain RPM, adding power as necessary in response to rotor torque demand. Table 2.3 is similar to the control table in patent (US3656723) [1]. The rotors are effectively hingeless rotor heads with bearings for blade feathering. A stiff rubber insert allows some compliance of the feathering axis to flap and lead/lag as well as the blade retaining bolt in the blade grips allows lead/lag of the blades. The hingeless rotor systems allow for control moments to not only be generated by tip path plane tilt, but also allows moments to be directly applied to the mast through blade flapping. Initial testing showed adequate control of the vehicle.

Table 2.3: Vehicle Control Allocation

	Rotor 1	**Rotor 1**	**Rotor 1**	**Rotor 1**
Pitch Control	Fore/Aft Cyclic	Fore/Aft Cyclic	Fore/Aft Cyclic	Fore/Aft Cyclic
Roll Control	Left/Right Cyclic	Left/Right Cyclic	Left/Right Cyclic	Left/Right Cyclic
Yaw Control	Diff. Cyclic	Diff. Cyclic	Diff. Cyclic	Diff. Cyclic
Altitude Control	Collective	Collective	Collective	Collective

Initial control gains were based on values for conventional fixed-pitch multirotor vehicles. With initial hover tests, the gains can be increased (or decreased) based on a procedure of applying control step inputs on each axis and watching how the vehicle follows the commanded input. If oscillations develop to step inputs, the gain should be reduced. If structural coupling exists, the structure should be stiffened before attempting to correct the gain. Interestingly, the pitch and roll gains for a conventional multirotor required only minor adjustments while the yaw gain needed significant changes. This may be attributed to a poor 'default' gain recommendation from the flight controller, due to the different mechanism for yaw control, or significant changes in the z-axis moment of inertia. A more accurate procedure of system identification and gain tuning should be implemented, especially due to the differences in control latency of changing motor RPM versus changing the blade angle and rotor flapping.

The flight control system is shown in Fig. 2.5. The Pixhawk 2.1 has 14 available output channels but at least one port was used for actuator input power. The design needs a minimum of 4 output channels per rotor, a total of 16 for this vehicle. This requirement was relaxed by controlling the throttle signal directly through the receiver as opposed to an output signal from the flight controller. It is desirable to have an output channel for

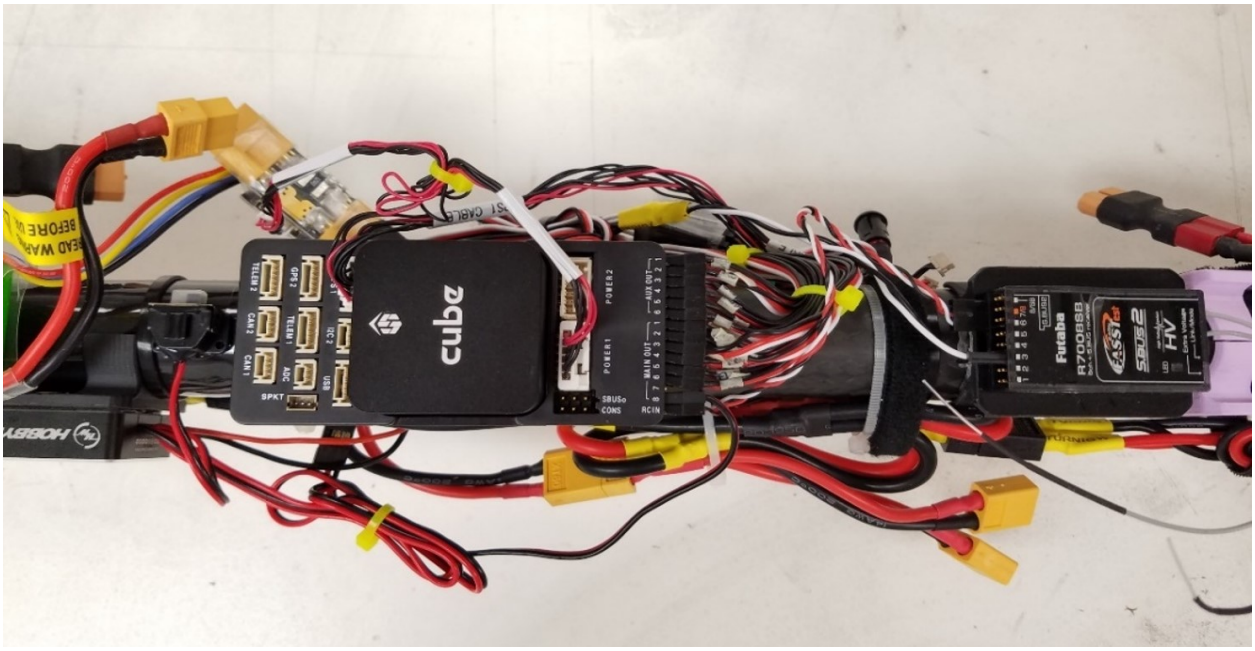

Figure 2.5: Initial Frame concept (without strut-braces)

each motor on the flight controller to allow an additional actuation method. An external tachometer was not installed on the vehicle which would be desirable for normal flight modes and would be necessary for autorotation flight. The flight controller, telemetry, receiver, and actuators are powered separately from the main propulsion batteries. This provides an added layer of safety to ensure control even if the propulsion batteries were to have a fault. This, however, adds a possible failure mode.

For the initial design, each rotor would have its own battery for simplicity of wiring. Concerns of RPM control and the failure of a single battery pack necessitated all of the batteries to be tied together so that the voltage of the system would be approximately equal, and the batteries would deplete uniformly. From a structural standpoint, adding the battery mass underneath the rotors would provide inertial relief for the frame structure, however, from a vibration standpoint, adding mass underneath the rotors, at the end of the arms, would lower the natural frequencies. Because this was a concern, the four small battery packs were replaced by two larger battery packs mounted on the main fuselage tube. For the first flights of the vehicle, the two front rotors were powered by one battery, while the two aft rotors

were powered by another battery. The batteries, however, were not tied together on a main bus line. Low voltage alarms were installed to alert the pilot when a critical voltage was reached in either pack so the vehicle could be safely landed. During one test, the vehicle began to show reduced control on the pitch axis. The pilot commanded nose-down pitch but the aircraft continued to drift backward. As more nose-down pitch was commanded, the aircraft suddenly pitched aggressively nose down and crashed. While the cause of the crash was not fully discovered, one possible cause was low voltage for the aft rotors, resulting in lower RPM, and a nose-up pitch attitude. After the incident, the fore and aft rotors were tied together with a wiring harness to ensure that voltage is approximately equal for all rotors.

Figure 2.6: Vehicle Electronics & Propulsion Batteries

Setup of the rotors was difficult due to flight controller not having an easy method to adjust servo travel and servo zero position. The lengths of the threaded mechanical linkages with ball-ends need to be changed individually. Careful measurements of swashplate position, blade angle, and swashplate angles are necessary to set each rotor to an initial starting value so the vehicle would trim properly. A significant number of short duration hover tests and linkage adjustments were necessary to trim the vehicle. Additionally, each rotor disk can assume a different angle and different collective pitch positions while the vehicle still trims. This is not desirable and was mitigated by more careful linkage adjustments. Blade tracking is also a critical to mitigate vibrations. This is done by hovering

the vehicle and viewing each rotor disk to see if there are two distinct rotor planes. The high-flying blade link must be shortened to reduce the pitch angle. This task is made more difficult when the rotor systems have more than two blades.

2.3 Structural Properties

The structural of properties of the carbon-composite tube use for the fuselage were not given by the manufacture. The tubes are referred to as 'Pullbraided', company specific process that involves creating a pultruded tube with a braided sleeve at $+/-45°$ as part of the layup. The complete layup schedule includes fibers at $0°$, $90°$, and $+/-45°$ Even though composites are non-isotropic, this layup schedule should have more consistent properties in all directions when compared to a carbon-composite tube with fibers at $0°$ or at $0°$ & $90°$ only. These tubes were chosen based on their 'high performance' from previous experience. The $+/-45°$ layers also enhance the torsional properties of the tube, which is important for the long, thin-walled tubes. On the manufacture's website [8], a value of 13 *msi* to 17 *msi* for the 'Tensile Modulus (stiffness)" is reported for several diameters offered. While this was assumed for elastic (Young's) modulus in the initial assessment of the vehicle, it was important to perform a structural bending test to confirm or adjust the values given. Additionally, without a stated Poisson's ratio, the shear modulus would need to be found experimentally for the torsional motion of the fuselage components.

Using the solution to the elastica, for a cantilever beam with a load at the end, from Hibbeler [39], the solution for a the maximum displacement due to a bending load is given in eq. 2.15 while the solution for maximum angle displacement due to a torsional load is given in eq. 2.16.

$$\nu_{max} = -PL^3/3EI \tag{2.15}$$

$$\theta_{max} = TL/GJ \tag{2.16}$$

(a) Structural Member Bending Test (Test Frame)

(b) Structural Member Bending Test (Loading Hook and Measuring Device)

Figure 2.7: Structural Bending Test

The experiment set up for the bending test is shown in fig 2.7. A tube of known length was placed into the test stand and clamped into place. At the end of the tube, a hook structure was bonded to the tube and a measuring 'needle' bonded to the end. A combination square with $1/16 inch$ graduations was mounted to base of the test structure. The opposite end of the tube was restrained to the base by steel cable and turnbuckle to resist torsional motion of the stand during the bending test. The most likely source of error of the test is the compliance in the test stand. A fishing scale was attached to the hook and ten data points were taken, incrementally increasing the force for each data point.

Figure 2.8 show the experimental setup for the torsional test. A similar hook structure used for the bending test was used for the torsion test, located at the end of a small moment arm. A vertical support and bearing, shown in fig. 2.8 were added to eliminate bend from the torsional test. A digital angle gauge with $+/-0.1^{\circ}$ accuracy was used to record angular

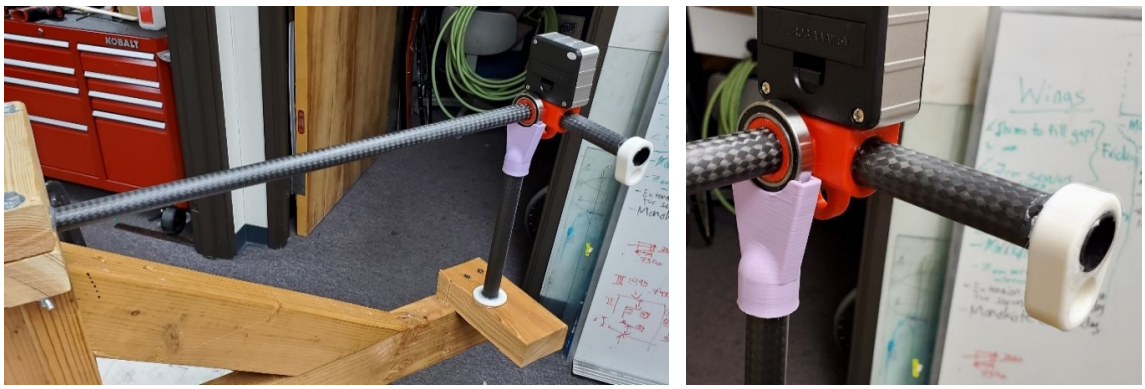

(a) Structural Member Torsion Test (Test Frame)

(b) Structural Member Torsion Test (Support, Moment Arm, & Angle Gauge)

Figure 2.8: Structural Torsion Test

deflection. Additionally, adhesive was added between the tube and the clamp to reduce the risk of the tube moving in the mount. Each test was performed two times and the load

Table 2.4: Elastic & Shear Modulus Structural Test Data

	Test 1	***Test 2***
Elastic Modulus, $E_{avg}[psi]$	8.635e6	8.518e6
Shear Modulus, $G_{avg}[psi]$	2.391e6	2.280e6

was released between each data point. The bending test displacement versus load data is shown in fig. 2.7. The torsional angular displacement versus moment load data is shown in fig. 2.10. For both test, the data is relatively linear which indicates that there was not structural damage to the tube or test equipment during the data collection. Additionally, the linearity from low load to high load would suggest that there was not major compliance in the test structure itself, however some compliance likely exists. Rearranging eqs. 2.15 & 2.16 to obtain eqs. 2.17 & 2.18 show the expressions to calculate elastic modulus and shear modulus, respectively.

$$E = \frac{PL^3}{3\nu_{max}I} \tag{2.17}$$

$$G = \frac{TL}{\theta_{max} J} \tag{2.18}$$

The resulting elastic and shear modulus data is shown in figs.2.11 & 2.12. Table 2.4 shows the compilation of the structural test data with the average value of the elastic and shear modulus for each complete test. The values obtained in the test was substantially lower

Table 2.5: Structural Test vs. Manufacturer's Data [8, 9, 10]

	Experimental	***Manufacturer Data***
Elastic Modulus, $E_{avg}[psi]$	$8.635e6$	$14.55e6$
Shear Modulus, $G_{avg}[psi]$	$2.391e6$	$4.5e6*$

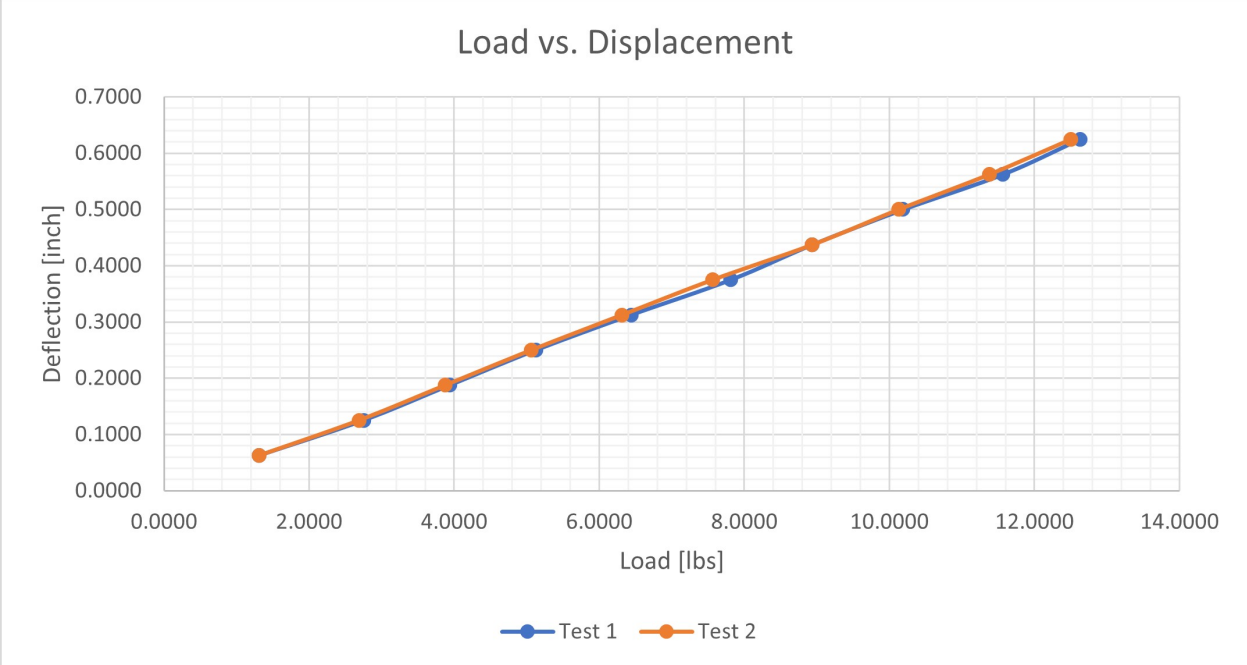

Figure 2.9: Bending Test Load vs. Displacement

than the reported values from the manufacturer. Possible sources of error for the test include compliance in the test stand, compliance in the hook and moment arm structure, and inaccu-

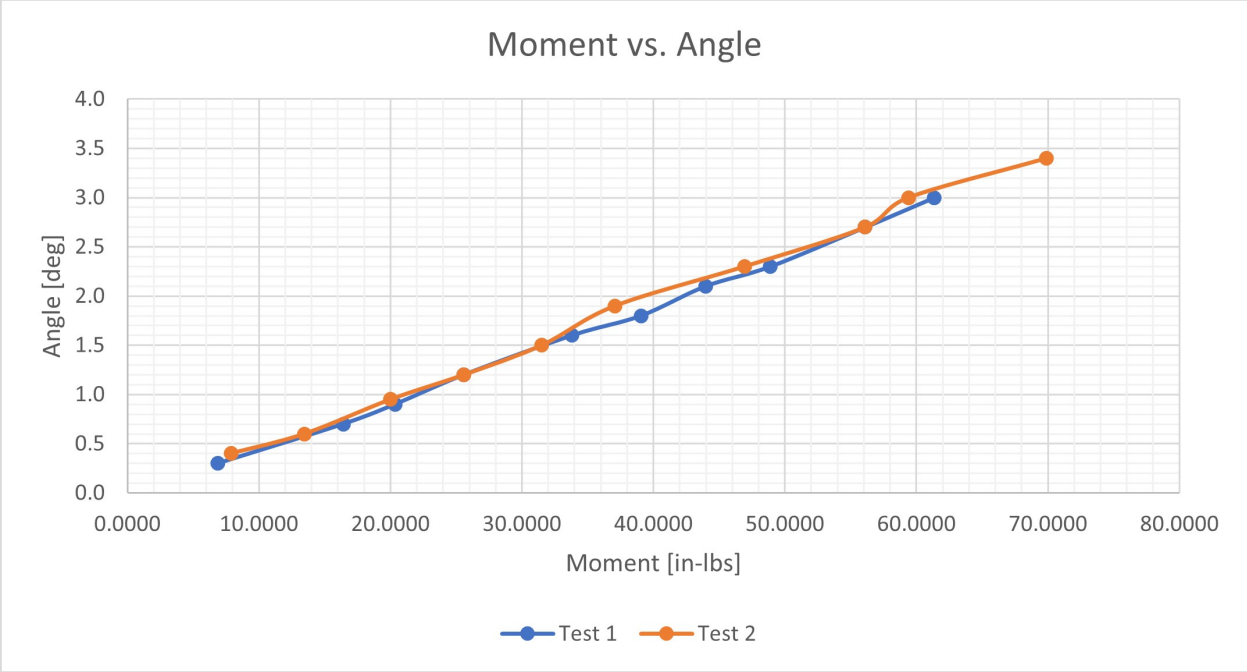

Figure 2.10: Torsion Test Moment vs. Angular Displacement

racies in load and displacement measuring devices. The values obtained from this test were compared with the values obtained from manufacturer's data, shown in table 2.5. For the simplified model, the manufacturer's data matched the FEA model and the flight test data better than the experimental structural test data, however, the manufacturer's data resulted in predicted frequencies that were consistently higher than the flight test data. This is likely due to flexibility in the joints and structural arrangement that was not accounted for in the simplified model. Taking this into account, either a different value for the moduli could be used or slight changes to the length of the structural members to modify the response. Changes to the length of the structural members was the method used for the analysis.

**Data for shear modulus was not provided by the manufacturer. The data was obtained from Clearwater Composites [9] for unidirectional carbon tube and compared to datata from Performance Composites Ltd. [10]. The Rockwest Pullbraided tubes should perform as well or better, under a torsional load, than a unidirectional tube due to the fibers oriented at* $+/-45°$.

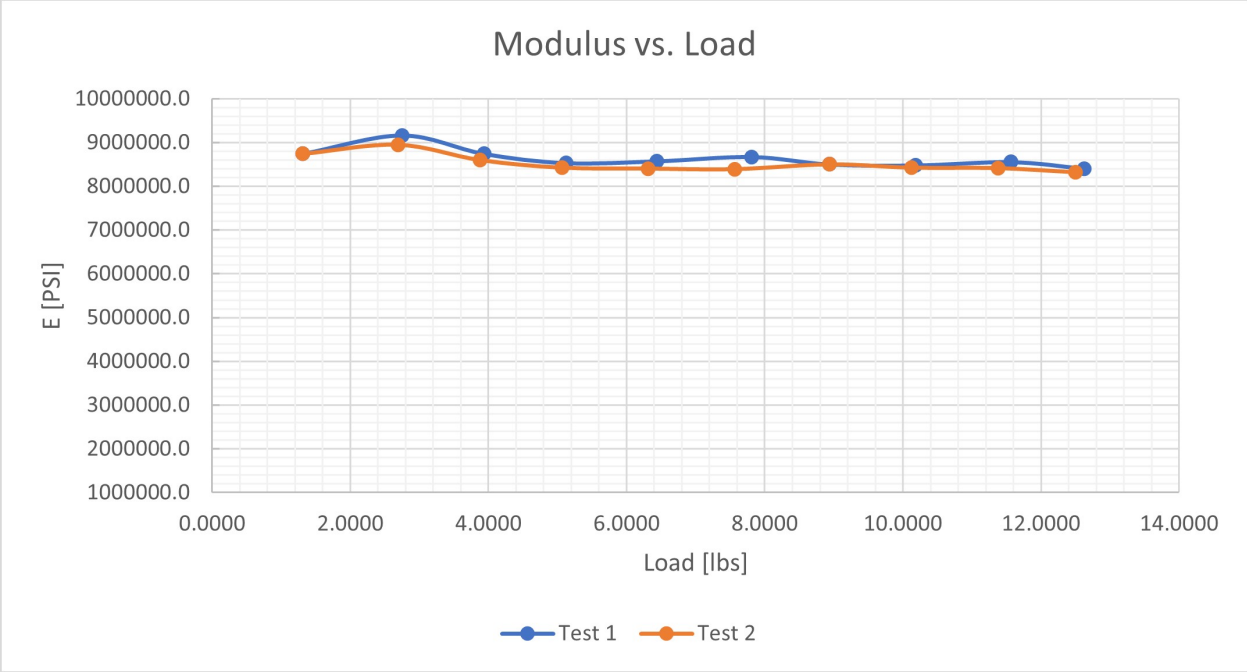

Figure 2.11: Bending Test Elastic Modulus vs. Load

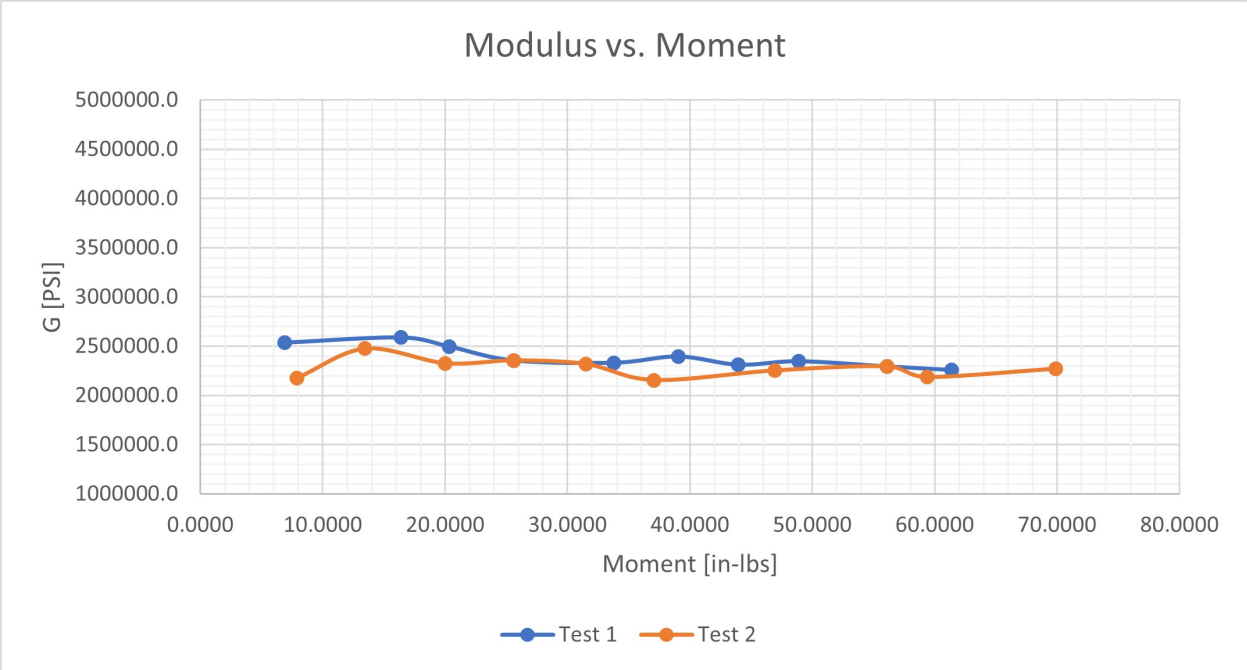

Figure 2.12: Torsion Test Shear Modulus vs. Moment

2.4 Finite Element Analysis

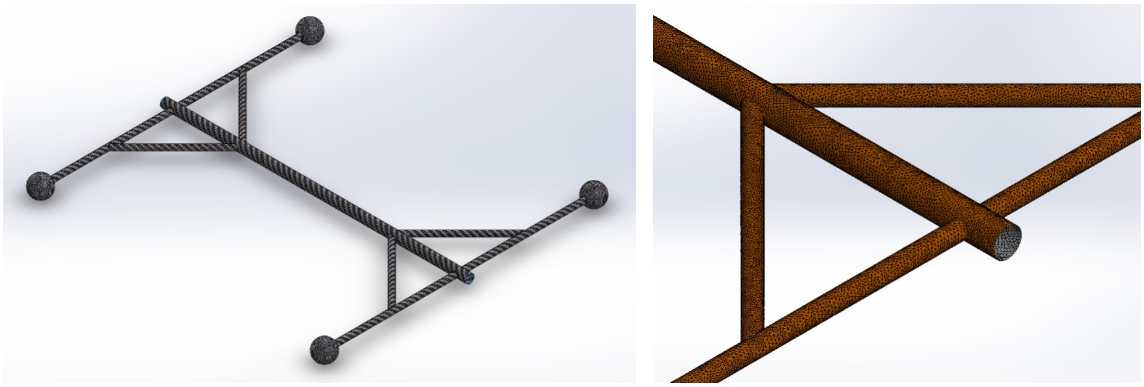

(a) Example Finite Element Analysis Model

(b) Typical Finite Element Analysis Mesh

Figure 2.13: Structural Torsion Test

The finite element analysis (FEA) was performed using primarily SolidWorks Simulation. The model was derived from the original CAD model used to manufacture many of the airframe components, but was simplified for meshing and simulation convergence. Components and features such as the tube couplers, rotor mechanics, electronics, and accessories have been omitted. The tubes are modelled as surfaces to utilize 2D surface elements. Intersections of the tubes were carefully modelled to facilitate meshing at the joints. The rotor mechanics and batteries were represented with simple masses in the appropriate locations.

The modal analysis performed in FEA environment does not account for any structural damping or aerodynamic damping. The modal analyses performed are compared to the undamped simplified physics model and results from flight testing to assess the accuracy of the physics model and provide a check of the FEA model. Table 2.7 shows the simulation setup. The model was unconstrained, and no external loads were added. The material used is representative of the Rockwest Pullbraided carbon-composite tubes using the manufacturer's material data for the FEA model and physics model. As described previously, the lengths of the structure members were 'tuned' to account for flexibility of the joints in the simplified

Table 2.6: Composite Tube Manufacturer's Data [8, 9, 10]

Rockwest Pullbraided Carbon Fiber Tube	
Material Property	***Value***
Elastic Modulus (from [8]) $[psi]$	$14.55e6$
Shear Modulus (estimated based on [9, 10]) $[psi]$	$4.5e6$
Poisson's Ratio (estimated from [10])	0.10
Tensile Strength $[ksi]$	355
Compressive Strength $[ksi]$	230
Density $[lbm./ft^3]$	0.058

Table 2.7: Finite Element Analysis Model Setup

Material	***Restraint***	***Load***	***#Frequencies***	***Surface thickness***
Rockwest Pullbraided	Free-Free (Unrestrained)	No External Load	12	0.04 $inch$

model, however this was only performed on the simplified model while the model used for the FEA analysis is true to size.

Table 2.8: Finite Element Analysis Predicted Resonant Frequencies

Mode	***Predicted Frequency Frame Design 1***	***Predicted Frequency Frame Design 2***	***Predicted Frequency Frame Design 3***
First	$10.4Hz$	$10.7Hz$	$15.4Hz$
Second	$16.4Hz$	$18.5Hz$	$46.5Hz$
Third	$36.3Hz$	$45.9Hz$	$66.7Hz$
Fourth	$38.7Hz$	$62.6Hz$	$76.4Hz$
Fifth	$42.1Hz$	$62.8Hz$	$104.5Hz$
Sixth	$55.1Hz$	$140.4Hz$	$118.4Hz$

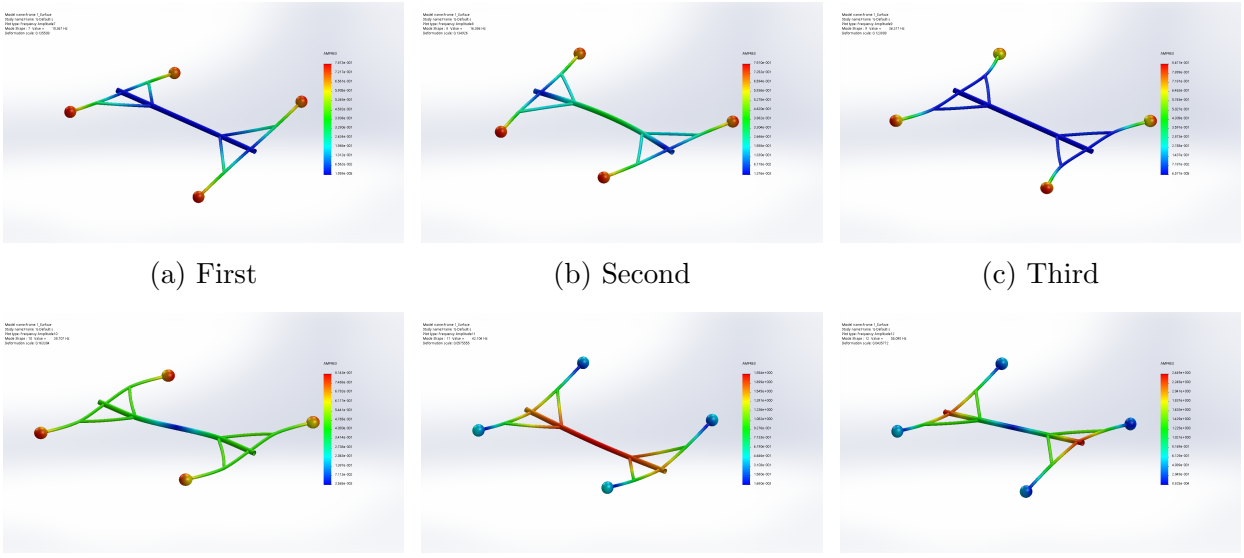

(a) First (b) Second (c) Third

(d) Fourth (e) Fifth (f) Sixth

Figure 2.14: First six mode shapes for frame design one without fuselage masses (from the top left to right)

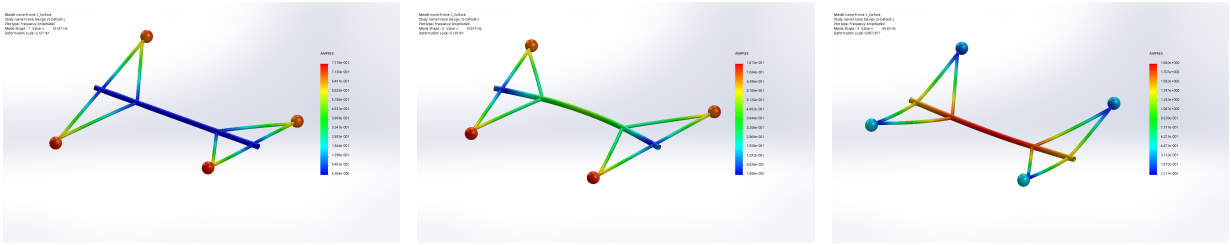

(a) First (b) Second (c) Third

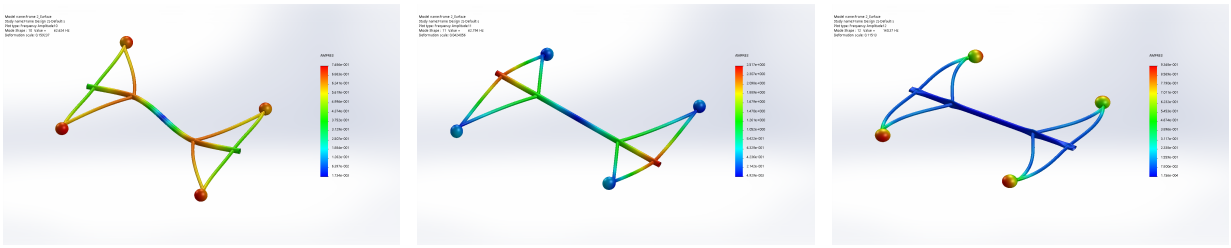

(d) Fourth (e) Fifth (f) Sixth

Figure 2.15: First six mode shapes for frame design two without fuselage masses (from the top left to right)

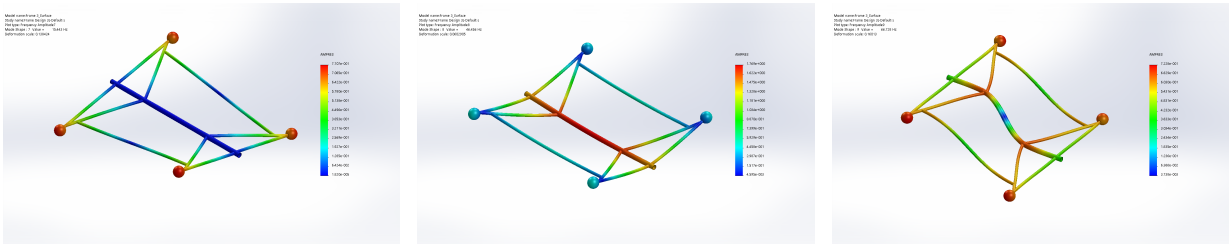

(a) First (b) Second (c) Third

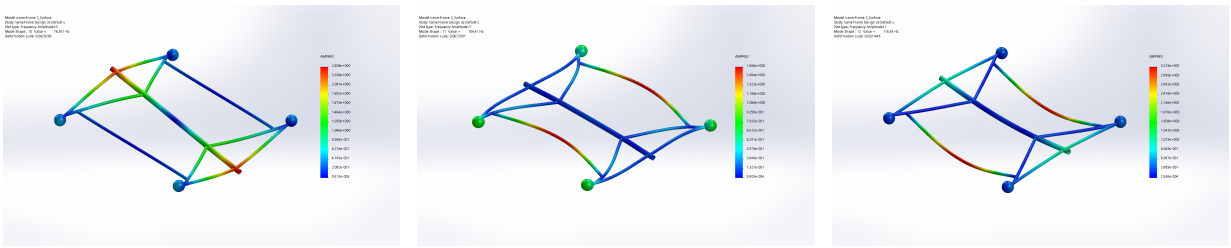

(d) Fourth (e) Fifth (f) Sixth

Figure 2.16: First six mode shapes for frame design three without fuselage masses (from the top left to right)

The FEA model setup and boundary conditions are cataloged in table 2.7. The model was instructed to compute 12 resonant frequencies and the resulting mode shapes. Due to the free-free boundary condition (unrestrained), the first six resonant frequencies represent six rigid-body mode; 3 displacement modes and 3 torsional modes. This leaves six flexible body modes. These six resonant frequencies are sufficient to characterize the dynamic response of the airframe structure as the highest predicted resonant frequencies were well above the rotor RPM and frequencies of energy from other sources. The resonant frequencies and mode shapes for each frame iteration is discussed in more detail in chapter 3, section 3.3, 3.4, & 3.5.

Table 2.9: Finite Element Analysis Resonant Frequencies With & Without Fuselage Masses (Frame Design One)

Mode	***Predicted Frequency (without fuselage masses), Fig. 13***	***Predicted Frequency (with fuselage masses), Fig. 14***
First	$10.4Hz$	$11.7Hz$
Second	$16.4Hz$	$18.2Hz$
Third	$36.3Hz$	$22.2Hz$
Fourth	$38.7Hz$	$29.0Hz$
Fifth	$42.1Hz$	$38.9Hz$
Sixth	$55.1Hz$	$40.7Hz$

The initial FEA models were simplified to only include the weights of the rotors at the end of the arm appendages. This would likely represent the arm models well but may degrade the predictions for the fuselage specific models because of changes in mass and inertia. Remote/virtual masses created challenges with computation time and convergence so component weights were represented as dense spheres with the material properties of aluminum alloy 6061, and the spherical volume set to match the weight of the represented components. Only major components were considered such as the flight batteries, the rotors, and groupings of electronics. The total weight was matched to the flight test vehicle weight.

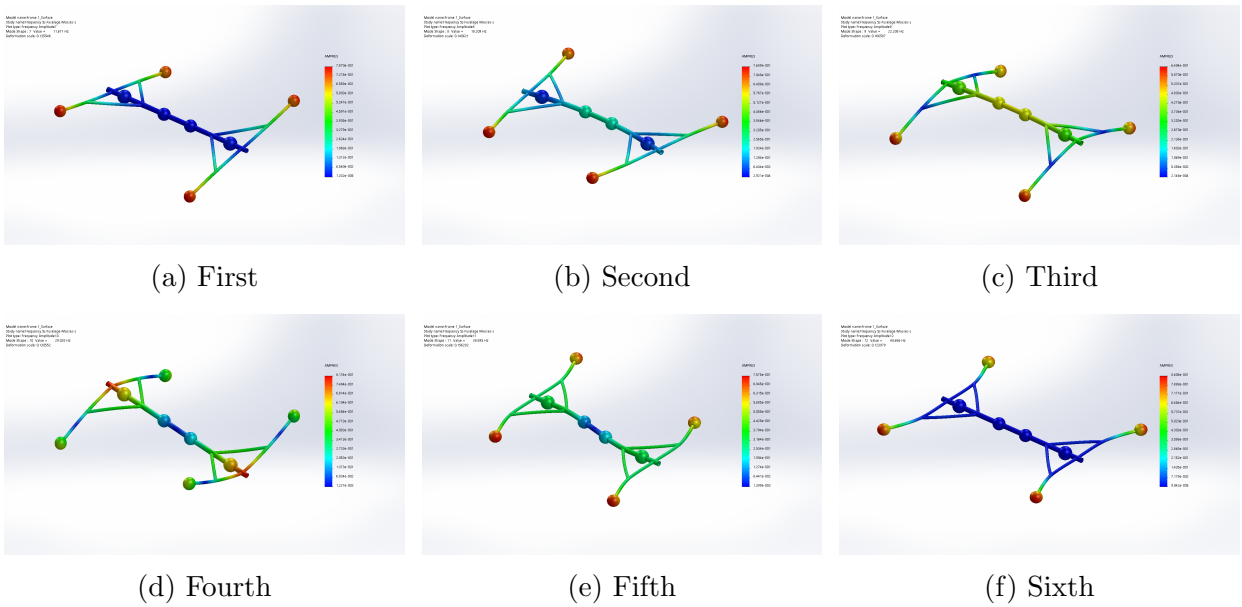

(a) First (b) Second (c) Third

(d) Fourth (e) Fifth (f) Sixth

Figure 2.17: First six mode shapes for frame design one with fuselage masses (from the top left to right)

This simplification does not match the inertia of the represented components. This would have the biggest impact on torsional modes. Addition of these spherical masses changes the stiffness of the model, especially in locations where the model bends. The computation time also increased with more bodies and computation challenges can occur if there is a poor-quality interface between the solid and surface bodies. A comparative test was performed to determine the effects on the resulting resonant frequencies and mode shapes with the inclusion of the fuselage masses. Table 2.9 shows the first six flexible body resonant frequencies of the same frame iteration with and without the fuselage masses. Figures 2.14 & 2.17 show the mode shapes of the first six flexible body modes with and without the fuselage weights. Interestingly, there is a slight increase in the first two modes which represent the fuselage torsional mode and the fuselage in-plane bending mode. It would be expected that an increase in mass and inertia would lower the resulting resonant frequencies of these modes. It is possible that the inboard fuselage masses increased the stiffness of the tube member, increasing the resonant frequencies. There was also a small increase in the arm in-plane bending mode, but the four arm in-plane bending modes (1 symmetric, 1 anti-

symmetric for each configuration) have similar predicted frequencies. The most pronounced change is the mode that represents the arm bending out of the plane. Without the fuselage masses, the predicted resonant frequency is approximately two time higher than when the fuselage masses are included. This is because without the fuselage masses, the low mass of the fuselage frame when compared with the large masses of the rotors causes the fuselage to vibrate vertically while the outboard rotor masses remain mostly stationary. When the fuselage masses are included, the outboard masses have more vertical motion combined with the fuselage motion. This is mode shape is a better representation of this specific flexible mode. The physics model treats the arms as cantilever beams fixed and the root with the rotor mass outboard. There is good correlation between the physics model result for arm out-of-plane bending and the FEA predicted resonant frequency when the fuselage masses are included in the FEA model. For the other modes of interest, the simplified model omitting the fuselage masses appears acceptable.

Figure 2.18 shows another specific scenario where the inclusion of fuselage masses is necessary. The physics model includes a prediction for an out-of-plane fuselage bending mode. For the fuselage bending modes, the physics model treats the fuselage structural member as a cantilever beam fixed at the center of the tube with a weight representing the two rotors and one battery on each half of the frame. Because the tube has an axisymmetric cross-section and the weight is the same, the predicted natural frequency for the fuselage bending in plane and out of plane is the same. In reality, this is unlikely. As seen in fig. 2.18, when the fuselage bends out of plane, the arm displace as well. This coupling of the arms and the fuselage bending is significantly different from the assumptions made it he physics model. The FEA model results show that the difference in predicted resonant frequencies is off by a factor of 2 when the fuselage weights are included. This is another situation where it would be necessary to incorporate the appropriate masses for an accurate prediction. As discussed more in Chapter 4, a lumped-mass model should be integrated into the physics model for more accurate predictions of structural natural frequencies.

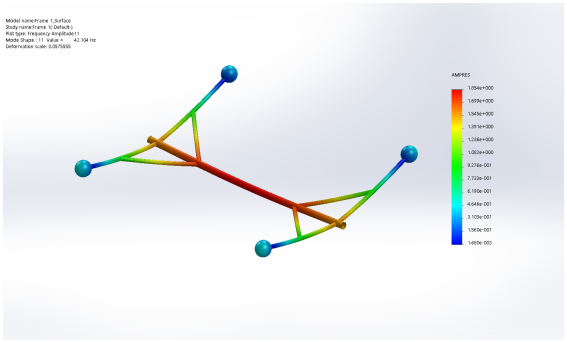

(a) Fifth (without weights)

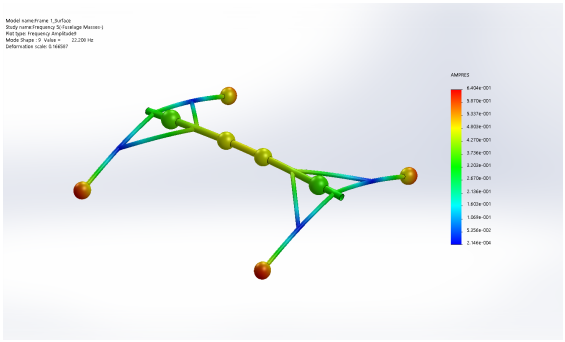

(b) Third (with weights)

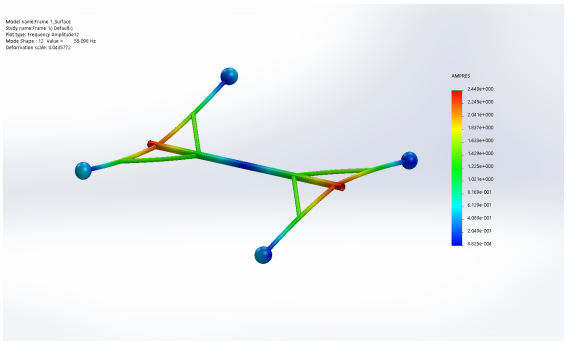

(c) Sixth (without weights)

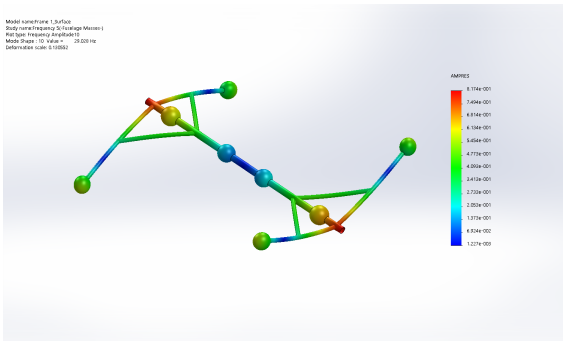

(d) Fourth (with weights)

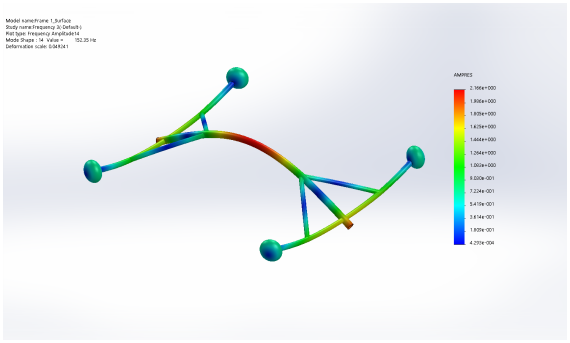

(e) Eighth (without weights)

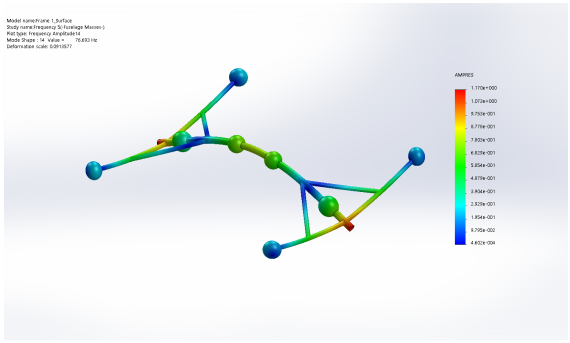

(f) Eighth (with weights)

Figure 2.18: Arm and Fuselage out-of-plane bending mode comparison with & without fuselage weights

Chapter 3

Flight Testing

3.1 Initial Strut Brace Failure

Initial hovering test flights were performed to tune the gains, assess flight performance, flight controls, structural vibrations, and RPM operational limits. It was discovered early that there was a narrow band of useable RPM. RPMs below this band and above this band resulted in significant frame vibrations. For the upper band, there appeared to be another useable region, but this RPM was rarely used. Table 3.1 describes the throttle percentage, predicted RPM, and observed vibration metric. Additionally, changes in RPM had significant

Table 3.1: RPM, Throttle %, & Vibration Characteristics

Throttle % (estimated)	$< 45\%$	45%–60%	60%–75%	$> 75\%$
RPM	< 1575	$1575 - 2100$	$2275 - 2675$	> 2675
ω ***Hz***	< 26	$26 - 35$	35–45	> 45
Observed Vibrations	High	Acceptable	High	Not tested

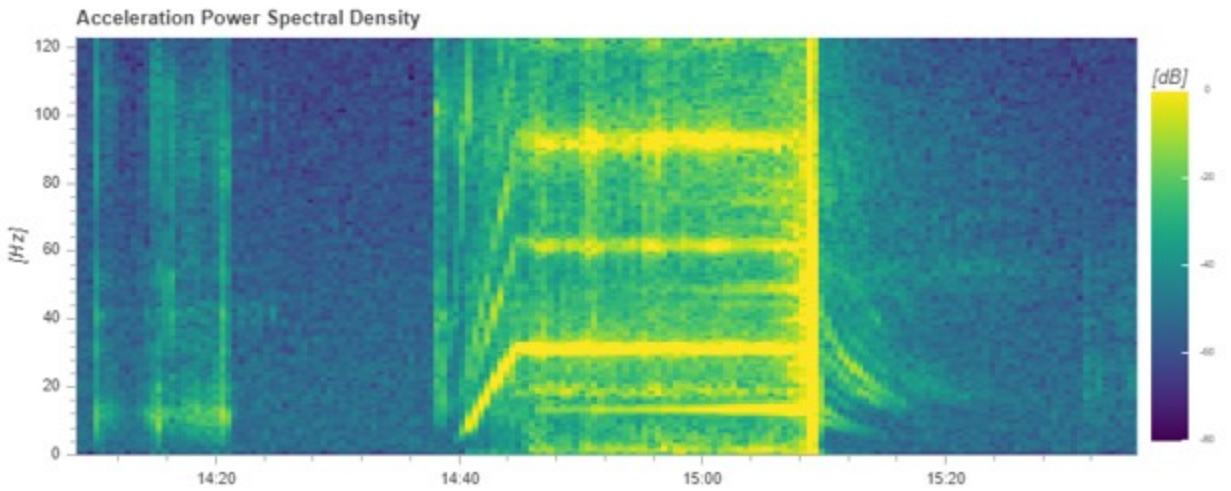

Figure 3.1: Acceleration Power Spectral Density Plot for Strut Brace Failure

impact on the stability and control from the pilot's perspective. When the RPM changed, the gains needed to be revised for acceptable flight characteristics. To operate at a variety of RPMs, a gain schedule would be necessary. After several hover tests the vehicle was tuned sufficiently and a forward flight was performed. Under manual control, the vehicle took off and was flown in a figure-8 pattern. Approximately 30 seconds into the flight, large amplitude vibrations were noticed in the aft, right arm. The throttle was cut, and the vehicle was safely landed in a controlled, autorotation decent. Once the aircraft touched down, however, the bond between the aft-right arm and the strut-brace failed. A portion of the structural coupler was also damaged. Figure 3.1 shows the acceleration power spectral density plot of the flight. The clearly defined bands at approximately 30 hertz shows the 1 rev (RPM) while the band at approximately 90 hertz shows the N rev frequency of the blades. The time at which the arm fails is clearly seen as the bright vertical band showing content at all frequencies. Interestingly, it appears as if some component began vibrating early in the flight at a frequency of approximately 10-15 hertz. The strut-brace may have failed earlier in the flight, but this is not clear. Figure 3.2 shows the raw accelerations from the flight and it shows that vibrations were building for nearly the entire flight but were only

visible to the pilot and observer after the amplitude of the vibrations was large enough to be seen in flight.

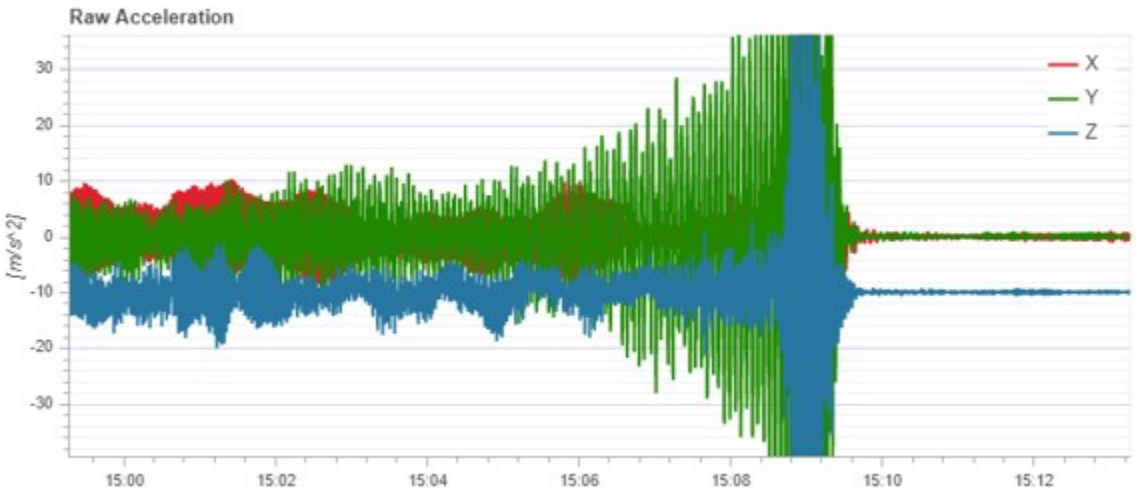

Figure 3.2: Acceleration Plot during Strut Brace Failure

After the strut-brace was repaired, pins were added through the tubes and coupler-joints to provide a more secure attachment of the struts. Test flights resumed and the flight controller gains were adjusted. With the enhancements made to the structure, the operational envelope was expanded to explore the RPM limits and revise the gains accordingly. Several successful test flights were performed exploring the vehicle performance and control during forward flight maneuvers. From an anecdotal pilot perspective, the vehicle did not handle significantly different from a conventional multirotor with fixed-pitch rotors and variable RPM. As discussed previously, for this vehicle, the RPM is held at a constant value while the blade angles are varied for control. The fact that this configuration had similar handling characteristics when compared to a convention multirotor is encouraging for development and use of the vehicle. Additional flight test will be necessary to determine if there are flight regimes where the vehicle handling significantly deviates and to discover any unusual handling characteristics. Figure 3.3 shows still images from one the video of the vehicle in forward flight.

Figure 3.3: Vehicle Shown in Various Stages of Forward Flight

3.2 Vehicle Crash

During another forward flight test, the aircraft was flying for approximately one minute when the pitch control began to degrade. The aircraft was slowly drifting backwards and did not respond to the commanded forward pitch attitude. As the aircraft continued to drift backwards and more nose-down pitch was commanded, suddenly the aircraft responded to the nose-down pitch commanded and struck the ground in a near vertical attitude. The source of this error was not clear. Possible causes include low voltage on the aft rotor battery, which was not tied with the forward rotor battery, radio interference, excessive vibration in the flight controller, and the use of a new flight mode that switched from commanding angles to commanding rates once a threshold on the pilot's controls was exceeded. Fig. 3.4 shows the acceleration power spectral density of the flight where the crash took place. There does not appear to be abnormal vibration frequencies or excessive energy when compared to other flights. This would rule out excessive flight controller vibration. Using a modern Futaba 2.4 GHz radio

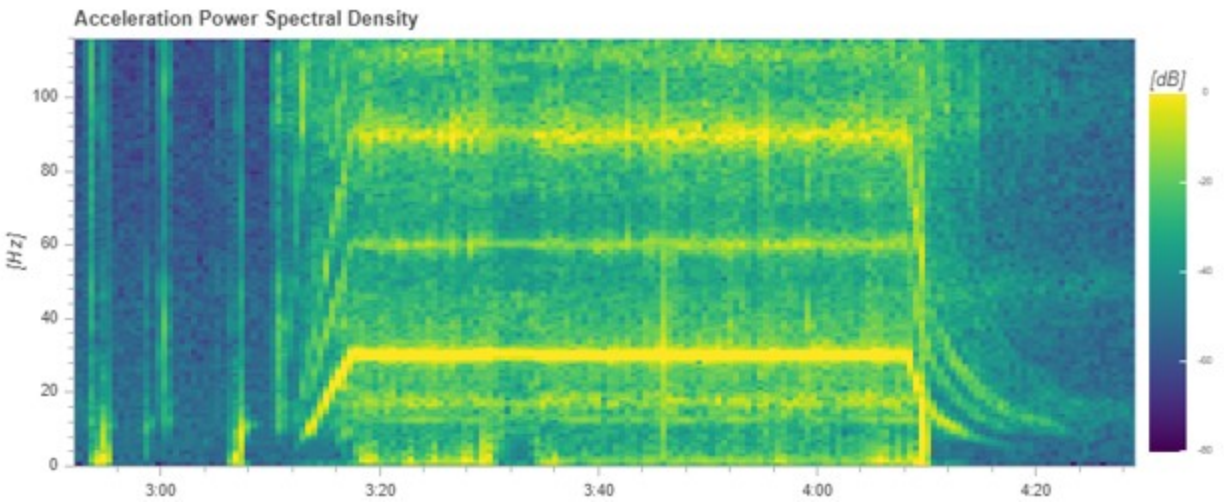

Figure 3.4: Acceleration Power Spectral Density Plot during Crash Flight

transmitter would make radio interference possible, but unlikely so this was ruled out. While the batteries for the aft rotors were not tied to the front rotors, it is possible that the RPMs were mismatched, causing an aft pitching moment, this would have shown up on Fig. 3.4 as a widened RPM band near 30 hertz or a second RPM band just below this 30 hertz band. An example of this is shown in Fig. 3.5, which was obtained from a different, successful flight where the vehicle was flown to the limit where the front rotors and aft rotors had mismatched RPM due to low voltage. The most likely cause of the crash was pilot error.

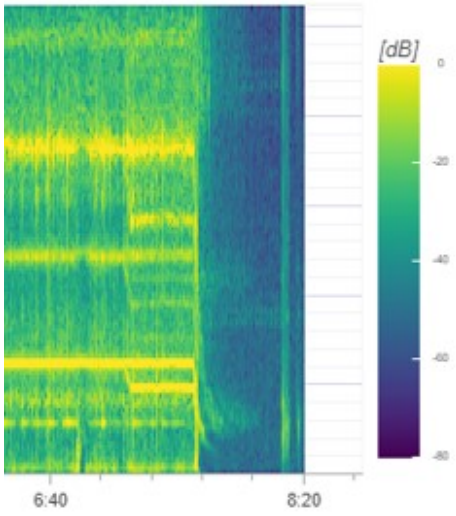

Figure 3.5: Acceleration Power Spectral Density Plot during RPM Mismatch

Initial inspection did not discover frame damage, however, damage to the rotor drive gears, rotor blades, main rotor shafts, and servo actuators occurred. The vehicle was repaired using OEM parts, except for the main rotor blades. Due to the cost of the main rotor blades, a decision was made to use rotor blades that have the same planform design and airfoil section, but with differences in weight and appar-

ent stiffness. The apparent stiffness was discovered later, after vibration damage occurred. The new blades were heavier than the OEM blades, which was a desirable trait, given that the higher blade inertia produces desirable autorotation characteristics, and increase necessary reaction time, for pilots to initiate an autorotation after an engine failure, as describe by Prouty [40] and Johnson [37]. The following section will discuss, in more detail, about the impacts of decision to use different blades.

3.3 Frame Arm Failure

After repairing the aircraft, hovering flight tests were performed to assess system function, trim the aircraft, and track the blades. One immediate result of the change of blade type was that the control gains need revision. This is likely due to the lower Lock number $\gamma = \rho a R^4 / I_B$ [37] of the new blades. Frame vibrations appeared more substantial to the pilot and observer, but this could also be attributed to poor tracking of the blades in at least one of the rotors.

Figure 3.6: Frame Arm Appendage Structural Failure

During one hover test, the vehicle RPM was increased to 75% throttle. As shown in Table 3.1, this RPM is on the boundary of dangerous vibrations. Large amplitude vibrations were observed by the pilot and observer. The aircraft motors were shut down and an autorotation decent initiated. Once the aircraft touched down and the RPM decayed into a range of high

vibrations, resulting in failure of the front right and back left frame arms, which subsequently separated from the vehicle. Several rotor blades were damaged as well as several actuators. The damage is shown in Fig. 3.6. It should be noted that the arm separated from the vehicle at the location where the structural-coupler pins were drilled into the arms. It is possible that damage to the inner tube layers during construction promoted the failure at this location, although a later failure would suggest the tube may have failed regardless of this addition. It was clear from this event that it would be critical to develop a deeper understanding of the frame harmonics and vibration sources. A model of the frame was developed for finite element analysis (FEA) simulations. The simulation showed surprising results.

Table 3.2: First Three Resonant Freq. for Frame Design One

Mode	***FEA Predicted Frequency***
First	10.4 Hz
Second	16.4 Hz
Third	36.3 Hz

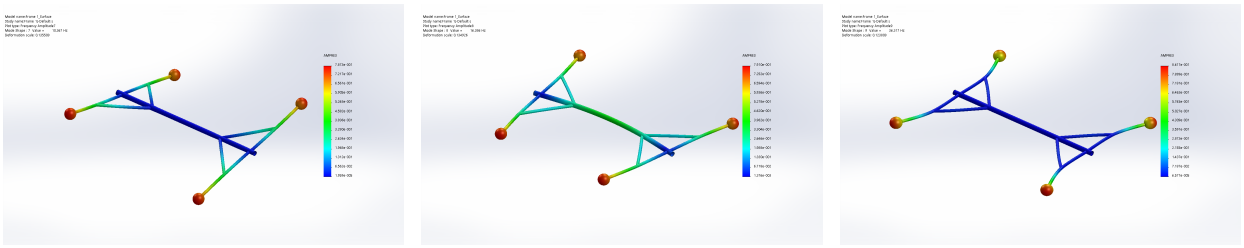

(a) First (b) Second (c) Third

Figure 3.7: First Three Mode Shapes for Frame Design One

Figure 3.7 shows the results from the FEA simulation for the first three mode shapes and predicted frequencies for the initial flight frame configuration that failed. Table 3.2 shows the predicted frequencies and, when compared with Table 3.1, the third harmonic mode frequency, predicted by the simulation, is close to the RPM the vehicle was operating at when it failed. Figure 3.8 and Fig. 3.9 show the acceleration power spectral density and the

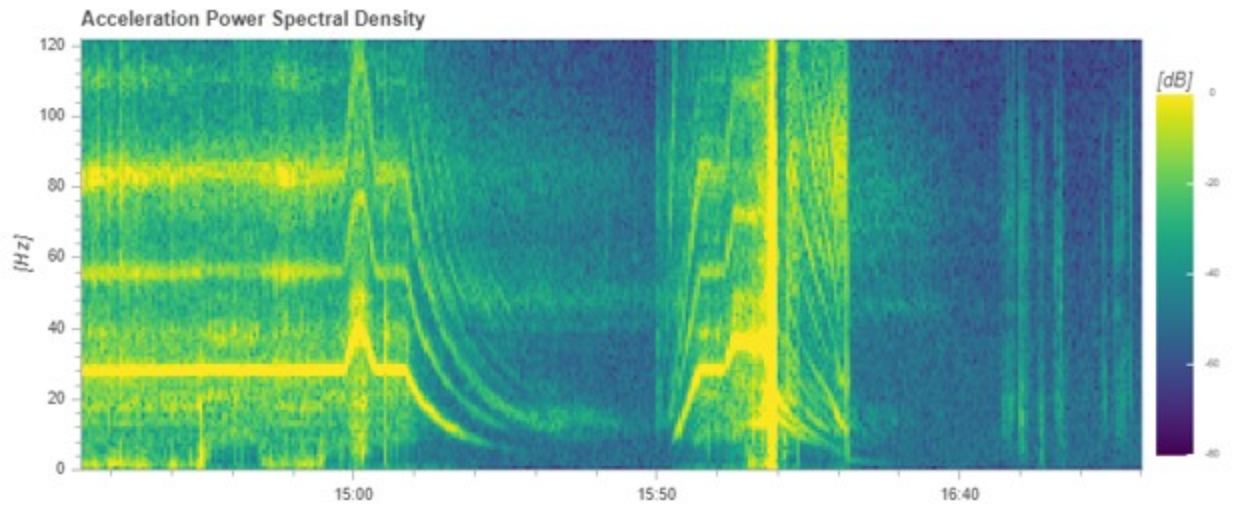

Figure 3.8: Acceleration Power Spectral Density Plot during Arm Failure

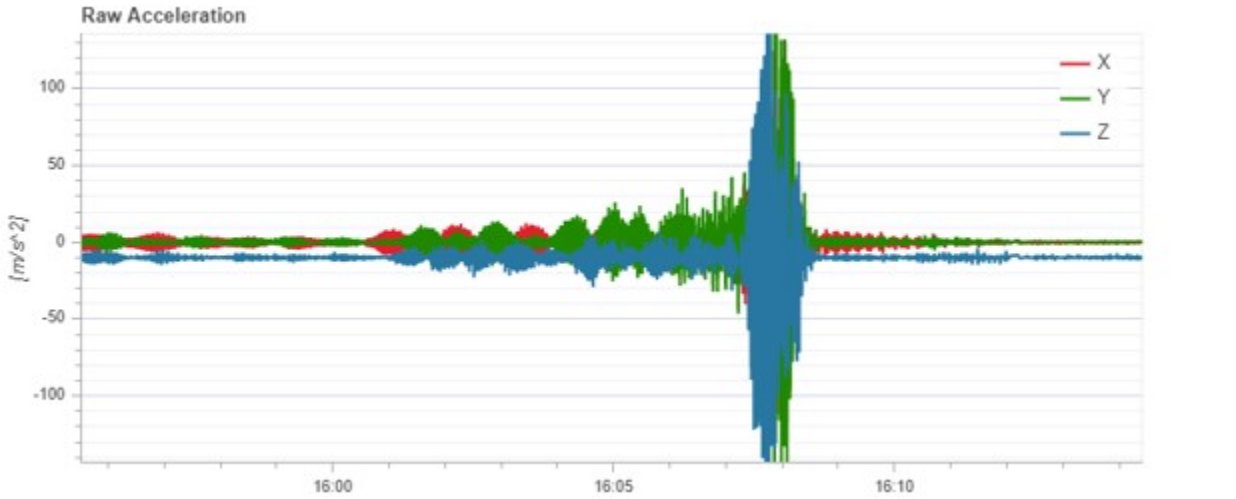

Figure 3.9: Acceleration Plot during Arm Failure

raw acceleration plots, respectively. This confirms that the operating RPM, at failure, was just below 40 Hertz.

Looking closer at this mode shape, seen in Fig. 3.10, the frame motion was similar to what was observed by the pilot and spotter just prior to failure. For the simulation model, the rotors and rotor mechanics were approximated as equivalent weights at the end of the arms and the plastic coupler joints were omitted from the simulation. Even with this lower fidelity model, the results were surprising. Starting with a simple mass-spring model, and obtaining

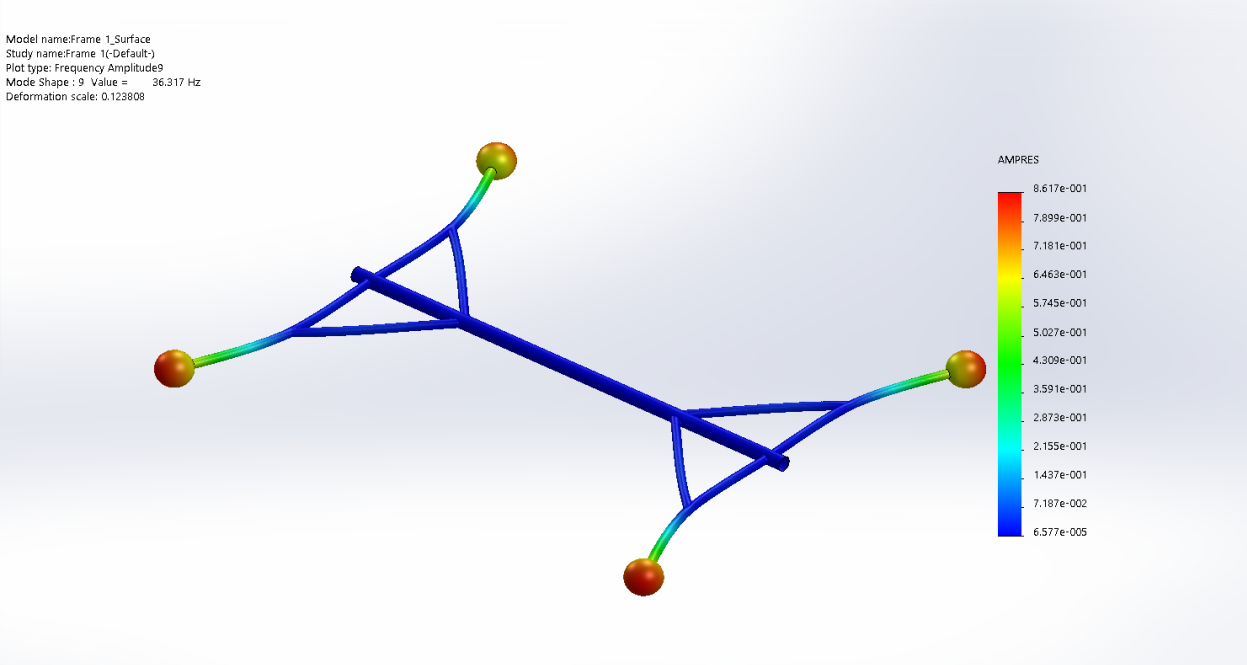

Figure 3.10: Finite Element Predicted Mode Shape Resembling Arm Failure

the equivalent spring constant and mass:

$$\omega_n = \sqrt{k/m} \tag{3.1}$$

some intuition could be developed for the proposed structural modifications. Using Palm [41], for a cantilever beam with a mass at the end, the equivalent lumped mass, m_e, is given by:

$$m_e = m_c + 0.23 m_d \tag{3.2}$$

where m_c is the mass at the end of the beam and m_d is the distributed mass of the beam. Additionally, using the solution to the elastica, for a cantilever beam with a load at the end $\nu_{max} = -PL^3/3EI$ from Hibbeler [39], and based on the method using $k = F/x$ from Palm

[41], the equivalent spring constant for the tube in bending can be found:

$$k = \frac{P}{\nu_{max}} = \frac{3EI}{L^3} \tag{3.3}$$

Where the area moment of inertia for the fuselage structural tubes is given by:

$$I = \frac{1}{4}\pi \left(R_o^4 - R_i^4\right) \tag{3.4}$$

Equations (15-18) clearly show that the natural frequency is sensitive to the length of the beam and tube cross-sectional geometry. Additionally, the material choice and weight at the end of the beam must be considered. This validates the choice to move the batteries from underneath the rotors to the center of the frame. It will also guide the material selection. While there would be a benefit to choosing a material that would have a less abrupt failure, using an aluminum tube, for example, would certainly reduce the natural frequency. The main guidance from this analysis is to increase the length of the strut-brace such that the beam does not have long, unsupported sections that would decrease the equivalent spring constant. The proposed change increased the strut-brace to the end of the arm. This was supplemented by a larger, more substantial tube joiner. The second structural configuration is shown in Fig. 3.11a. Due to damage to the rotor blades, new blades were purchased, but as before, these were not the OEM blades. The OEM blades come in sets of three blades that are matched to each other for weight and balance. The blades purchased are for a 2-bladed rotor. They come in sets of two that are matched to each other. It became very difficult to match three blades together and many blades were purchased to find a set that were compatible with each other. The rotor blades are shown in Fig. 3.11b. Additionally, it was discovered that the blades appeared to have different inertia and fundamental frequency. This was not experimentally verified, however a simple test by fixing the blade at one end, striking the other end, and estimating the frequency indicated that the blades vibrate at different frequencies.

(a) Frame Design Two

(b) Rotor Blade Comparison, from Top to Bottom: OEM Blade, Align Blade (blue), Align Blade (black)

Figure 3.11: Frame Design Two Changes

3.4 Frame Fuselage Failure

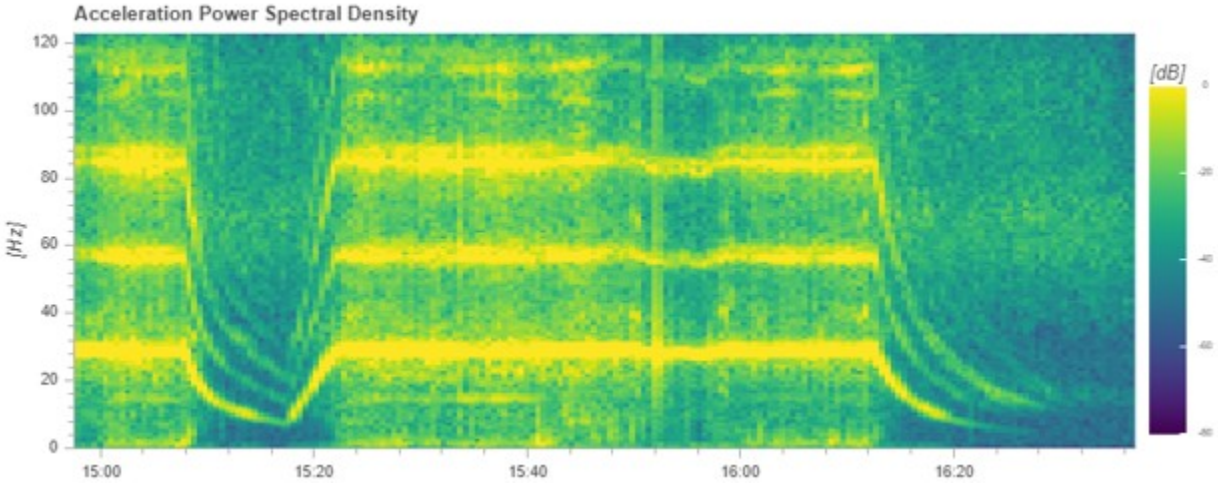

Figure 3.12: Acceleration Power Spectral Density Plot during Fuselage Failure

After the vehicle was repaired, the same procedure was used, as before, for the first flight after a repair. The vibrations in the frame were visually more significant than before and the vehicle was difficult to control and trim. While the low altitude, vertical autorotation performance was noticeably better with the new blades, the new blades seemed to increase frame vibrations.

Figure 3.13: Acceleration Plot during Fuselage Failure

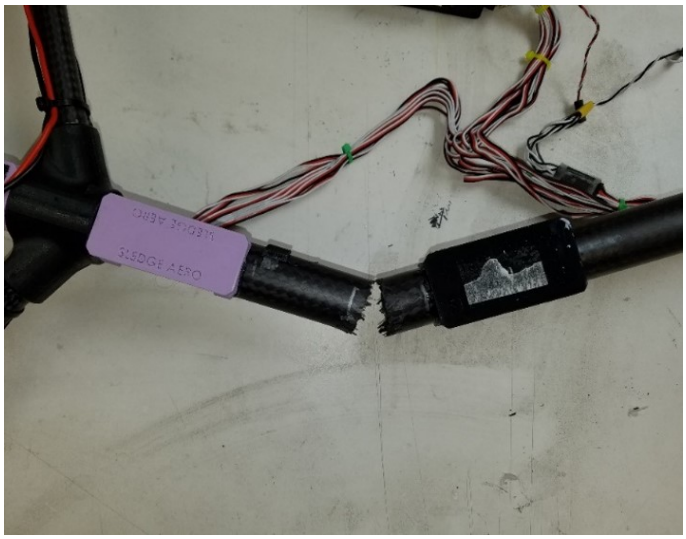

Figure 3.14: Fuselage Frame Structural Failure

The Pixhawk flight controller allows remote tuning of the gains from the pilot's transmitter. Small adjustments can be made in flight which facilitates the process. A hover test was being conducted to modify the pitch, roll, and yaw gains. The aircraft lifted off and while hovering, the pilot and spotter noticed significant vibrations that rapidly grew in amplitude. Similar to the previous failure, the kill switch was activated for the motors, but the reaction time was insufficient. The main fuselage tube failed in the middle and the forward portion of the vehicle separated from the aft portion. The main battery wires incidentally kept the two halves from completely separating and allowed a controlled landing. Fig. 3.14 shows the damage sustained during flight.

Once again, the acceleration power spectral density and raw acceleration plots were referenced in fig. 3.12 and fig. 3.13, respectively. Interestingly, the time at which the damage

occurred does not have a pronounced feature on either plot. There is a small possibility that the data was either lost or misinterpreted but is likely the time frame of the flight. As with the first structural failure, an FEA simulation was performed for the new configuration. The first three mode shapes and frequencies for this second configuration test are describe in Table 3.3 and Fig. 3.15.

Table 3.3: First Three Resonant Freq. for Frame Design Two

Mode	***FEA Predicted Frequency***
First	10.7 Hz
Second	18.5 Hz
Third	45.9 Hz

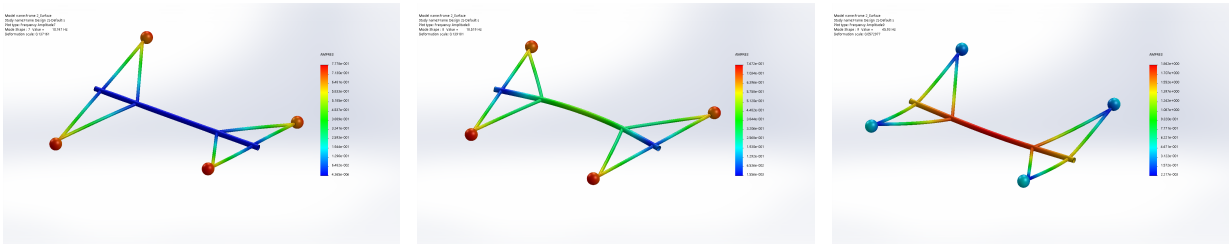

(a) First (b) Second (c) Third

Figure 3.15: First Three Mode Shapes for Frame Design Two

Even though the third mode shape is close to the 2/Rev frequency, the pilot's and observer's account of the event was most closely describe by mode shape two, see in fig. 3.16. While this is lower than the 1 rev frequency, it may be possible it was excited by this 1 rev energy. Additionally, the FEA simulation is currently a lower fidelity model and may not capture some of the physics, such as possible effects from aerodynamic-structural coupling.

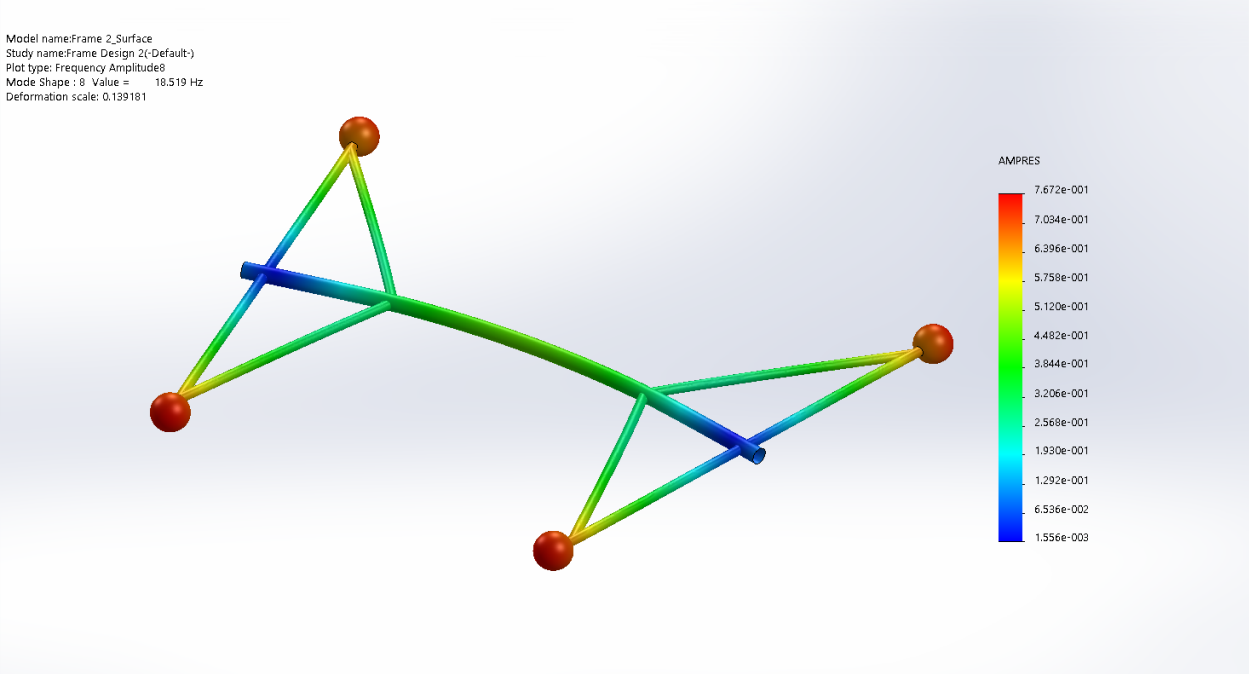

Figure 3.16: Finite Element Predicted Mode Shape Resembling Fuselage Failure

3.5 Current Frame Design

After the second failure, a custom tube joiner (ferrule) was used to reassemble the fore and aft sections, shown in fig. 3.17a. The ferrule was bonded to the inner tube and two ply of carbon fiber ($+/-45°$) was applied to the outer portion of the repair, shown in fig. 3.17b. Due to budget and time constraints, it was not feasible to change the main fuselage tube. There was concern that another material choice may improve the fatigue life, damage tolerance, and failure behavior. The concern with a material, such as aluminum, is that the elastic modulus would reduce the natural frequencies, which may increase the likelihood of exciting the frame harmonics during flight. This idea was dismissed at the time but should be revisited with changes to the frame geometry.

The geometry for the third frame iteration incorporated two struts connecting the front arm to the rear arm, just inside of the rotor mechanics. This modification can be seen in fig. 3.18. The addition of the lateral strut braces reduces the ability for the frame to bend in-

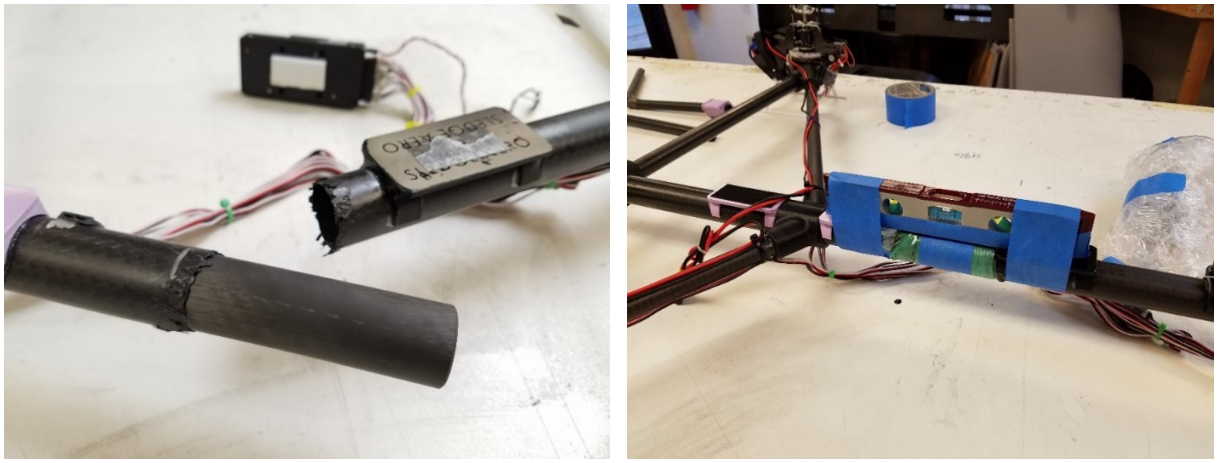

(a) Fuselage Structural Repair (Tube Ferrule) (b) Fuselage Structural Repair (Wet Layup)

Figure 3.17: Frame Design Two Changes

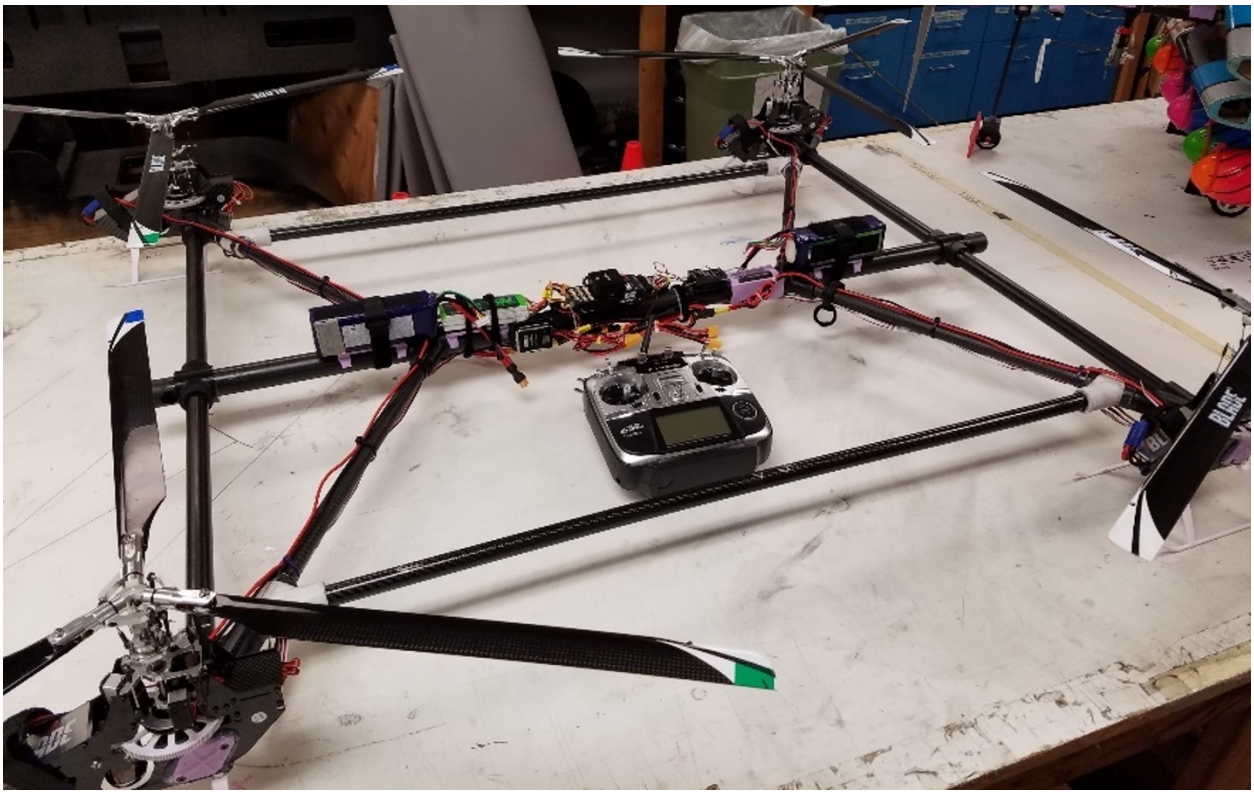

Figure 3.18: Frame Design Three

plane. An FEA simulation was performed to predict the new mode shapes and frequencies. The first three mode shapes and frequencies are shown in table 3.4 and seen in fig. 3.19. This analysis showed that with the changes to the geometry the fuselage torsional natural frequency increased as well as the out-of-plane bending mode. Only one mode remains below

the rotor RPM, at 15 Hertz predicted. This torsional mode, shown in fig. 3.20, would require significant changes to the frame design, such as a 3D truss frame, to increase the natural frequency. This was not a feasible option at this stage; however, the 3D truss frame would be an important modification to consider.

Additionally, the method of mounting the rotor mechanics to the frame will impact how vibrations are transferred to the frame. After the first crash, the rotor frame attachments to the main frame arms were revised to allow a layer of hot melt adhesive in between the mount and the rotor frame for vibration damping. A result of this change was a more secure connection and may have impacted the energy transfer from the rotors to the frame.

Table 3.4: First Three Resonant Freq. for Frame Design Three

Mode	***FEA Predicted Frequency***
First	15.4 Hz
Second	46.5 Hz
Third	66.7 Hz

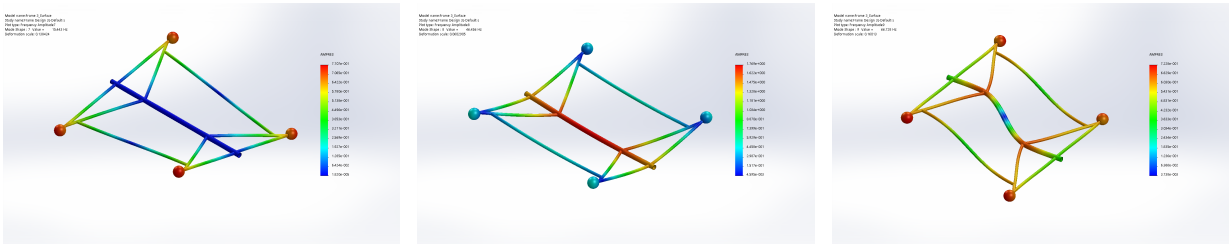

(a) First (b) Second (c) Third

Figure 3.19: First Three Mode Shapes for Frame Design Two

Figure 3.21 and Fig. 3.22 show the power spectral density chart from frame design one and frame design three, respectively. For frame design one, the bands of energy at the dominant frequencies are qualitatively narrow and there is low energy content between each band. The bands themselves have lower noise when compared with subsequent frame designs, especially frame design three. It is especially distinctive that the band of energy at 1 rev is

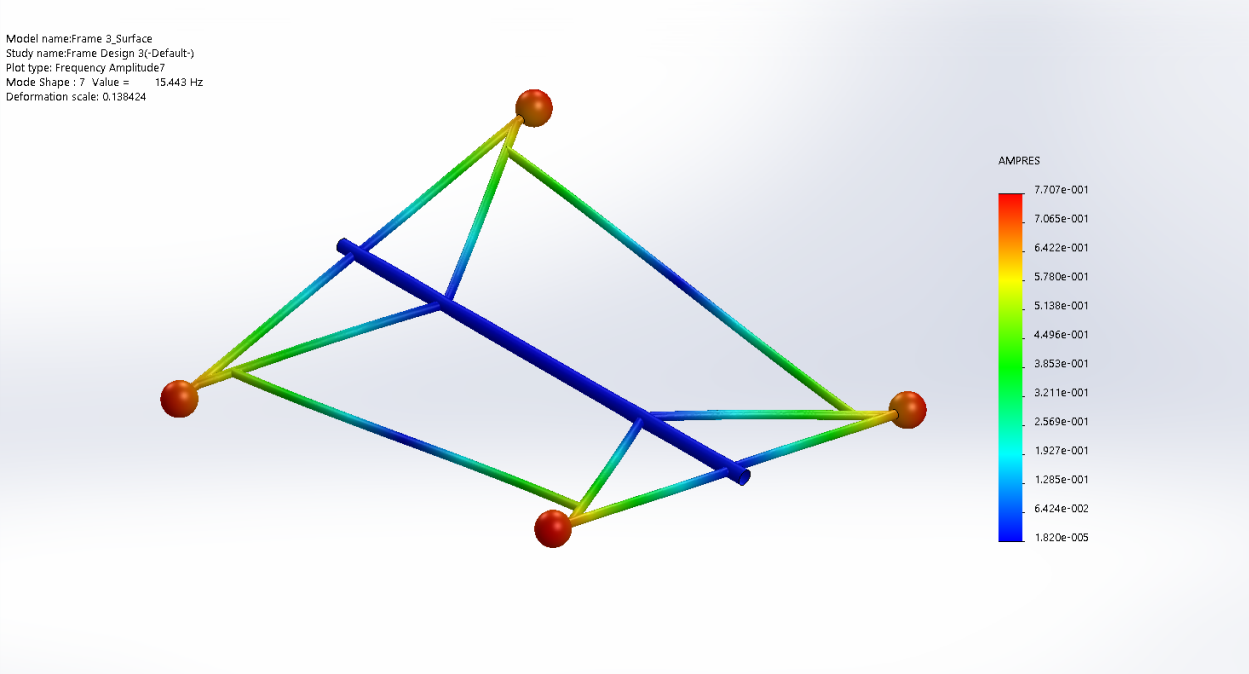

Figure 3.20: Finite Element Predicted Mode Shape for Frame Design Three Low-Freq. Mode

very narrow with low noise. The band at 2 rev is also very weak when compared to frame design three. While the band of energy at 3 rev is noisier when compared to the other bands, when compared with the 3 rev band from frame design three, it is clear the energy content is much less. Characteristically, the power spectral density chart from frame design three shows much higher vibrations and energy content. Another distinction is that the P.S.D. chart from frame design one shows a long, continuous flight. It last until the battery for one set of rotors depleted enough that the RPM for one set of rotors split and maintained a lower RPM until the vehicle was landed, which can be seen around 7:30 on the chart time history. This is significant because it shows that the vehicle was easy to control, and the vibrations were low and unobtrusive to the stability of vehicle and structural integrity. Even when the RPMs split, this was not obtrusive to the pilot. Comparing this with frame design three, the vibrations were significant enough that the vehicle could only be flown for short increments. At this point, the vibrations were degrading the control & stability of the vehicle, as well as providing visual cues that the vehicle structure may be in 'danger'. This is interesting because the changes from frame design one to frame design three were intended to make

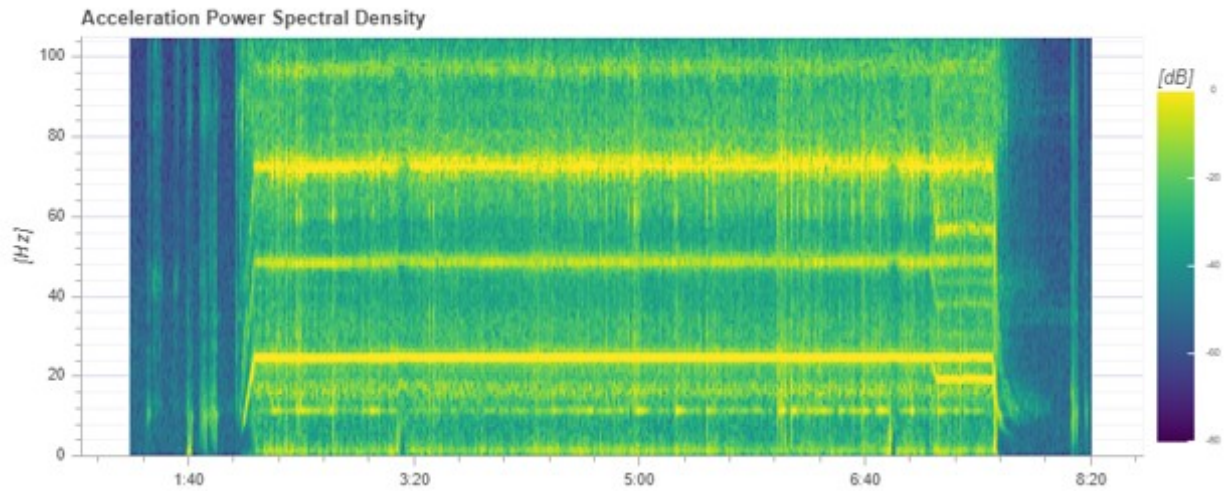

Figure 3.21: Acceleration Power Spectral Density Plot for Frame Design One (Successful Flight)

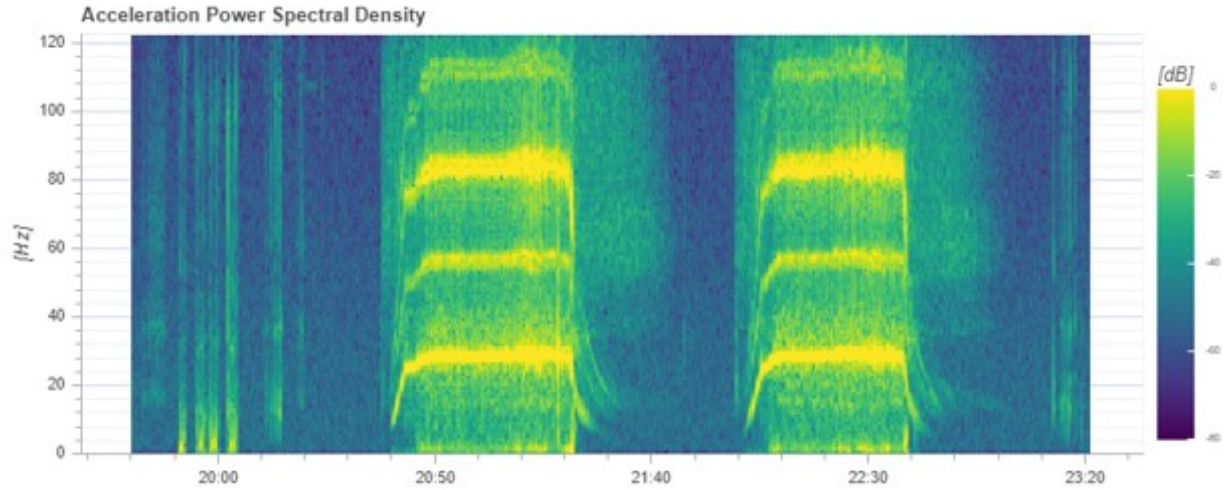

Figure 3.22: Acceleration Power Spectral Density Plot for Frame Design Three (Successful Flight)

the vehicle more robust and less susceptible to vibrations. While some of these changes eliminated flexible modes of the vehicle, it appears that the increased stiffness has increased the vibration in the vehicle and specifically the vibrations the reach the flight controller. There are a couple possible contributions to this degradation. For frame design one, the rotor-fuselage attachment point, shown in fig. 3.23a was sized so that the joint between the rotor frame and the attachment was tight, with minimal gaps. The end cap is screwed into place, clamping the frame to the attachment interface. After the initial vibration damage to

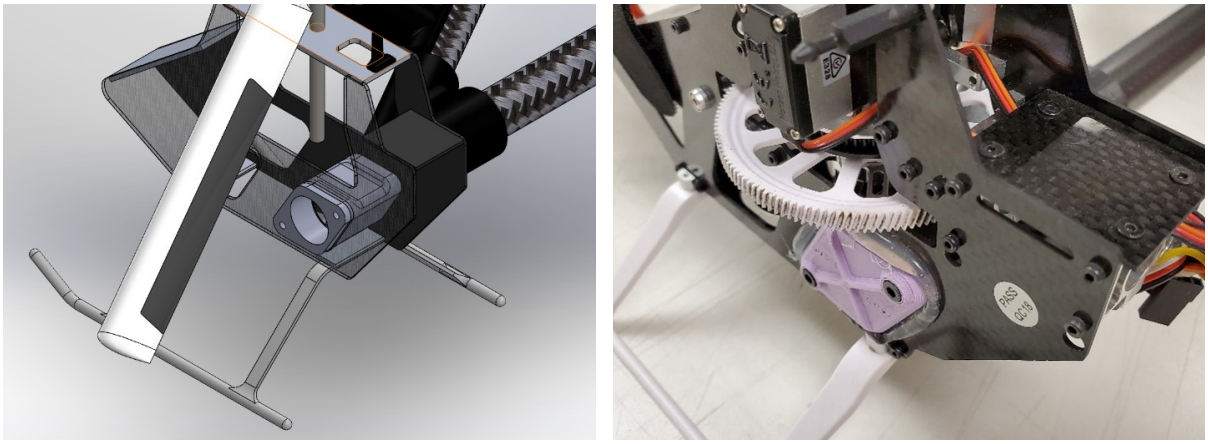

(a) Rotor-Fuselage Attachment (b) Rotor-Fuselage Attachment Bond

Figure 3.23: Frame Design Two Changes

frame design one, interface joint was modified so that there was a small bond line of hot-melt glue. The points of contact between the rotor frame and the interface joint were padded with hot-melt glue during installation. Hot-melt glue was then added to the end cap before it was screwed into place, shown in fig 3.23b. The idea was to provide a small amount of vibration damping between the rotor frame and the interface. The hot-melt glue is slightly flexible but still rigid so moments could be effectively transferred to the frame. It is possible that this new joint design is more rigid than the previous design. Characteristically, the connection 'feels' more solid than the previous design. In the previous design, if the rotor frame was able to move, slightly, on the interface joint, this would have some ability to dissipate some energy. With this joint more rigid, the transfer of energy from the rotor through the frame may be more effective. Additionally, after the initial damage to frame design one, the structural joints for frame design two and frame design three became more substantial. The thickness and size of each joint was increased. This would have likely increased the stiffness of the frame and may have changed and/or reduced any structural damping when compared with joints that had more compliance. Another source of vibration noise may be found in the rotor mechanics. As components in the rotor have worn, the connections are not as tight and maybe be contributing to noise shown in the power spectral density chart. The ball joints on the pushrods from the frame to the swashplate and the swashplate to the blade

grips do wear and become more loose over time. Noticeable compliance is also found in the blade grip connections to the rotor head. Most model helicopters are two-bladed systems. In the typical design, a solid feathering shaft passes through the rotor head and the blade grip are connect to the feathering shaft through radial bearings, and a thrust bearing and bolt that hold the blade grip on to the feather shaft. The feathering shaft is supported in the rotor head with a semi-rigid piece of elastomer or hard plastic. The rotor system is not like a teetering rotor, but more closely related to a hingeless rotor. For this current design, the three-bladed rotor system was chosen attempting to reduce vibrations. Since dominant vibration from the rotor are general at 1 rev and N rev where N is the number of blades, a two-bladed rotor system will have dominant vibrations as 1 and 2 rev These low-frequency, high-amplitude vibrations can be more challenging to design to. For model helicopters, it is possible to find rotor heads with more blades with three being the most common alternative. Unfortunately, the design for the three-bladed rotor head used has some deficiencies. It is not possible to have a solid feathering shaft for more than two blades, so each blade grip is connected to a single feathering shaft that has a cantilever connection in the rotor head. Small elastomer dampers support the feathering shafts in the rotor head. Over time, the connections between the feathering shafts to the rotor head and feathering shafts to the blade grips have worn significantly and there is a lot of compliance in the flap direction of each blade. The wear is also inconsistent from blade to blade. It is not clear what the impact is, however, this would likely be noticed at the N rev. frequency because the N rev frequency comes from each blade changing angle and flapping once per cycle. As time has progressed, the N rev. frequency has more noise and energy content when compared to early flights of the vehicle, as seen in fig. 3.21 and fig. 3.22. It is also possible that stiffening the structure has reduced the aerodynamic damping from the rotors. A rotor with six-degrees of freedom has aerodynamic damping as the rotor moves in space. Without this motion, the motion of the rotor at the end of the vibrating appendage may have a reduced aerodynamic damping. While the additional members added to the frame reduced or eliminated modes of

vibration in the frame, these changes also reduced motion of the rotors, possibly reducing the aerodynamic damping realized in the frame. This may have created a more efficient transfer of vibration energy from the rotor to other parts of the frame, including the flight controller. The following chapter analyzes the coupling of the frame vibration, motion of the rotors, and the aerodynamic damping. This analysis develops understanding of the frame susceptibility to vibration damage, which vibration modes are at risk, and proposed solutions to reduced potential damage in the frame.

Chapter 4

Coupled Aeroelasticity Flight Dynamics Analysis

4.1 Rotor Stability & Control Derivatives

The stability and control derivatives are calculated from methods described by Johnson [37] and Padfield [42]. A code was written to calculate the values of the derivatives and test data from Heffley et. al [7], Franklin [43], Hilbert [44], and Padfield [42] was used to compare and validate the code. For more information regarding the terms and derivations of the stability & control derivatives, readers are referred to the text by Johnson [37].

For an articulated single main rotor, the force is generated due to blade flapping. The tilt of the lift vector, due to blade flapping, at a height, h, above the CG, creates the moments on the vehicle. For a hingeless rotor, moments are also developed due to the root moment of the blades flapping transferred to the hub through the root connection. A hingeless configuration can generate significantly higher moments and an articulated rotor with hinge springs or pitch-flap coupling can generate higher moments than a purely articulated rotor

system. A tandem rotor configuration generates in-plane and out-of-plane forces like a single main rotor configuration; however, the longitudinal moments are dominated by differential thrust. Longitudinal moment due to pitch rate is governed primarily by differential thrust due to pitch rate and is realized by the heave derivative and the rotor spacing.

4.1.1 Single Main Rotor Stability Derivatives

$$X_u = -\frac{\gamma}{M^*\left(1+N_*^2\right)}\left[\frac{2C_T}{\sigma a} - \frac{\nu^2-1}{\gamma/8}\left(R_\theta - H_\theta N_*\right)\right]8M_\mu + \frac{\gamma}{M^*}\left[H_\theta 8M_\mu - \left(H_\mu + R_\mu\right)\right] \tag{4.1}$$

$$X_q = \frac{\gamma}{M^*\left(1+N_*^2\right)}\left[\left(\frac{2C_T}{\sigma a} + H_{\dot\beta}^* - \frac{\nu^2-1}{\gamma/8}R_\theta\right)\left(\frac{16}{\gamma}+N_*\right) - H_\theta K_P\left(\frac{16}{\gamma}N_* - 1\right)\right] - hX_u \tag{4.2}$$

$$M_u = \frac{\left(\nu^2-1\right)8M_\mu}{k_y^2\ M^*\left(1+N_*^2\right)} - \frac{h}{k_y^2}X_u \tag{4.3}$$

$$M_q = -\frac{\left(\nu^2-1\right)\left(\frac{16}{\gamma}+N_*+h8M_\mu\right)}{k_y^2\ M^*\left(1+N_*^2\right)} - \frac{h}{k_y^2}X_q \tag{4.4}$$

$$Z_w = -\frac{\gamma C'/4}{M^*} \tag{4.5}$$

$$C' = \frac{1}{1 + \frac{\sigma a}{16\lambda_0}} \tag{4.6}$$

$$M^* = \frac{1}{g}\gamma \left(\frac{2C_T}{\sigma a}\right)_{trim} \tag{4.7}$$

$$\nu^2 = 1 + \frac{3}{2}\frac{e}{e-1} + \frac{K_\beta}{I_b \Omega^2 (e-1)} \tag{4.8}$$

$$N_* = \frac{\nu^2 - 1}{\gamma/8} + K_P \tag{4.9}$$

$$K_P = \tan \delta_3 \tag{4.10}$$

$$H_{\dot{\beta}} = \frac{C_T}{\sigma a} + H^*_{\dot{\beta}} = \frac{C_T}{\sigma a} - \frac{\lambda_{HP}}{4} \tag{4.11}$$

$$M_\mu = \frac{2C_T}{\sigma a} + \frac{\lambda_{HP}}{4} \tag{4.12}$$

$$\lambda_{HP} = (C_T/2)^{1/2} \tag{4.13}$$

$$H^*_{\dot{\beta}} = -\frac{\lambda_{HP}}{4} \tag{4.14}$$

$$\frac{M_{\nu>1}}{M_{\nu=1}} \cong 1 + \frac{\nu^2 - 1}{h\gamma 2C_T/\sigma a} \tag{4.15}$$

4.1.2 Tandem Main Rotor Stability Derivatives

$$M_q = -\frac{\gamma l^2 C'/16}{k_y^2\ M^*} - \frac{h}{k_y^2} X_q = -\frac{g l^2 C'}{16 k_y^2\ (2C_T/\sigma a)} - \frac{h}{k_y^2} X_q \tag{4.16}$$

$$M_{\Delta w} = \frac{\gamma l^2 C'/16}{k_y^2\ M^*} = \frac{g l^2 C'}{16 k_y^2\ (2C_T/\sigma a)} \tag{4.17}$$

4.1.3 Control Derivatives Single Rotor

$$X_\theta = -\frac{\gamma}{M^*\left(1 + N_*^2\right)} \left[\frac{2C_T}{\sigma a} - \frac{\nu^2 - 1}{\gamma/8}\left(R_\theta - H_\theta N_*\right)\right] \tag{4.18}$$

$$M_\theta = \frac{(\nu^2 - 1)}{k_y^2\ M^*\left(1 + N_*^2\right)} - \frac{h}{k_y^2} X_\theta \tag{4.19}$$

4.1.4 Control Derivatives Tandem Rotor

$$X_\theta = -\frac{\gamma}{M^*\left(1+N_*^2\right)}\left[\frac{2C_T}{\sigma a} - \frac{\nu^2-1}{\gamma/8}\left(R_\theta - H_\theta N_*\right)\right] \tag{4.20}$$

$$M_{\theta,\ tandem} = \frac{\gamma l C'/12}{k_y^2\ M^*} = \frac{glC'}{12k_y^2\ \left(2C_T/\sigma a\right)} \tag{4.21}$$

4.2 MATLAB Code & Validation

A code was written in MATLAB to calculate the stability and control derivatives from given helicopter data. The results were validated against NASA test data and data from Padfield. The NASA data had a sufficient amount of aircraft data to calculate the stability derivatives with the exception of the hinge spring constants (or equivalent hinge spring constants for hingeless rotor systems). Padfield included this geometric data. The aircraft specifications remained consistent between Padfield and the NASA test data, however, some of the stability derivative results, at hover, were not consistent between the sources. A variety of aircraft of different sizes and rotor types were chosen to validate the code. The BO-105C was considered the benchmark for a hingeless rotor system. The CH-53D and Puma SA330 are articulated rotor systems. Data for the CH-47B, from Franklin [43], was included to evaluate a tandem rotor configuration. Geometric data for the CH-47B was obtained from Ostroff, Downing, & Rood [45]. Missing geometric data for the Lynx ZD559 was estimated from [46]. The UH-60 helicopter data was obtained from [44]. Although the data is not presented below, other aircraft were included in the validation. A variety of aircraft of different sizes and with different rotor head types were chosen to establish a range of acceptable output values and assess the sensitivity of the code to different input parameters.

There were significant challenges to evaluate the stability derivatives. Some of the difficulty was realized in collecting and evaluating the aircraft geometry and specifications. The stability derivatives are sensitive to parameters that were either incomplete or missing. Appropriate approximations were made based on 'tuning' the given parameters to match at least one of the critical stability derivatives. The realized value of the parameter was compared to other aircraft where the parameter was explicitly given to estimate if the value was reasonable and within bounds. The results show reasonable correlation between the test data and the MATLAB code. The derivatives all have the correct sign and many are around 10% or better correlation with the published data. This builds confidence for use of this code to generate the stability derivatives that will represent the aerodynamic damping in the structural vibration model and to evaluate the stability and control derivatives of new vehicle configurations for flight dynamics analysis.

Table 4.1: Damping Derivatives Comparison & Validation (Set 1)

Aircraft	***BO-105C***			***CH-53D***		
(Hover, at SL)	X_u [sec^{-1}]	Z_w [sec^{-1}]	M_q [sec^{-1}]	X_u [sec^{-1}]	Z_w [sec^{-1}]	M_q [sec^{-1}]
NASA	-0.0166	-0.3317	-3.3972	-0.0917*	-0.2980	-0.4990
Padfield	-0.0211	-0.3220	-3.7472	N/A	N/A	N/A
Franklin	-0.0170	-0.3300	-3.4000	N/A	N/A	N/A
MATLAB	-0.0166	-0.3324	-3.3832	-0.0186	-0.3066	-0.2690

Assumptions

The collection of sources was used to obtain the geometry and configuration data for the aircraft. The BO-105 helicopter was the most complete set of data because each source had data for the aircraft, so fewer assumptions were needed to complete the data set. This is the

*Data from source uncharacteristically high for X_u. Source [7] may have an error.

Table 4.2: Damping Derivatives Comparison & Validation (Set 2)

Aircraft	***Lynx ZD559***			***Puma SA330***		
(Hover, at SL)	X_u [sec^{-1}]	Z_w [sec^{-1}]	M_q [sec^{-1}]	X_u [sec^{-1}]	Z_w [sec^{-1}]	M_q [sec^{-1}]
NASA	N/A	N/A	N/A	N/A	N/A	N/A
Padfield	-0.0199	-0.3108	-1.8954	-0.0176	-0.3195	-0.4506
Franklin	N/A	N/A	N/A	N/A	N/A	N/A
MATLAB	-0.0171	-0.3087	-1.1660	-0.0116	-0.3141	-0.3810

Table 4.3: Damping Derivatives Comparison & Validation (Set 3)

Aircraft	***CH-47B***			***UH-60***		
(Hover, at SL)	X_u [sec^{-1}]	Z_w [sec^{-1}]	M_q [sec^{-1}]	X_u [sec^{-1}]	Z_w [sec^{-1}]	M_q [sec^{-1}]
NASA	N/A	N/A	N/A	N/A	N/A	N/A
Padfield	N/A	N/A	N/A	N/A	N/A	N/A
Franklin	-0.0210	-0.3000	-1.2300	-0.0240	-0.2900	-0.8200
MATLAB	-0.0171	-0.3043	-1.2691	-0.0200	-0.2909	-0.3995

reason this was the benchmark for validation of the code. For all aircraft, the coning angle was calculated based on eq. 4.22. The pre-cone angle was computed based on Johnson, by setting K_β to zero and then obtaining the value of the pre-cone angle, β_0. This was then input as the pre-cone angle for each aircraft, as this parameter was usually omitted from the aircraft data.

$$\beta_0 = \frac{1}{I_\beta^* \nu_{\beta_e}^2}\left[\gamma\left(\frac{3}{4}\frac{C_T}{\sigma a} + \frac{\lambda_{HP}}{48} + \frac{\theta_{tw}}{160}\right) + K_\beta \beta_p\right] \tag{4.22}$$

Additionally, the hinge offset and K_β (hinge spring) were only included for some of the aircraft. Because the stability derivatives for a helicopter are largely based on the flapping motion of the rotor blades, the derivatives are sensitive to coning angle, hinge offset, and K_β. When aircraft parameters were omitted, reasonable values were back calculated by

comparing the computed values to other known quantities, comparing computed values to other similar sized aircraft with known values, and adjusting the values to match at least one of the critical stability derivatives, such as M_q or X_u.

Parameter Estimates

The biggest discrepancy was noticed in the derivative data from Padfield, for both articulated and hingeless rotor systems. Padfield explains that the simulation model uses, a 'centre-spring equivalent rotor'. This model develops an equivalent spring at the hub that accounts for the flap-hinge spring, flap-hinge offset, and blade bending stiffness in the case of a hingeless rotor. The equation for ν^2, the natural frequency of the blade fundamental flap mode, differs slightly from Padfield's version, which may explain the discrepancy. This was made clearer when attempts were made to calculate the hinge offset, e, from Padfield's equation. This would yield zero each time, because Padfield sets the hinge offset to zero for the equivalent flap-hinge spring. For the MATLAB code using Johnson's equation for ν^2, the hinge spring, K_β, is not at the center of the hub, but is located at the flap-hinge. For this reason, the hinge offset had to be 'tuned' for the Padfield data to have reasonable agreement. For the aircraft data from Padfield, the hinge offset was 'tuned' to match M_q, within reasonable bounds, and cross-referenced with other data, such as measuring scaled helicopter schematics, when applicable. This same process was used when data for hinge offset or hinge spring stiffness was absent. The following tables show the stability derivatives for two helicopters where $N_* = 0$ and N_* is computed according to eq.4.9. This term, N_*, accounts for lateral-longitudinal coupling of the rotor as the hinge geometry changes either with a hinge spring or a hingeless rotor configuration, and with pitch-flap coupling. As Johnson describes, when $N_* \neq 0$, the flap response is reduced. The sign of N_* changes the phase lag of the response. Looking at the general equations of the stability derivatives, the term $(1 + N_*^2)$ shows up in the denominator of the in-plane and moment derivatives, however, it

does not show up in the heaving derivative, Z_w. With any pitch-flap coupling, hinge spring, or hingeless geometry, the value of $N_*^2 > 0$. This analysis showed that the derivatives match

Table 4.4: Effect of Lateral-Longitudinal Coupling on Derivatives (Set 1)

Aircraft	***BO-105C***			***CH-53D***		
(Hover, at SL)	X_u [sec^{-1}]	Z_w [sec^{-1}]	M_q [sec^{-1}]	X_u [sec^{-1}]	Z_w [sec^{-1}]	M_q [sec^{-1}]
NASA	-0.0166	-0.3317	-3.3972	-0.0917	-0.2980	-0.4990
Padfield	-0.0211	-0.3220	-3.7472	N/A	N/A	N/A
Franklin	-0.0170	-0.3300	-3.4000	N/A	N/A	N/A
MATLAB ($N_* = 0$)	-0.0175	-0.3324	-3.4593	-0.0186	-0.3066	-0.2556
MATLAB ($N_* \neq 0$)	-0.0166	-0.3324	-3.3832	-0.0186	-0.3066	-0.2690

Table 4.5: Effect of Lateral-Longitudinal Coupling on Derivatives (Set 2)

Aircraft	***Lynx ZD559***			***Puma SA330***		
(Hover, at SL)	X_u [sec^{-1}]	Z_w [sec^{-1}]	M_q [sec^{-1}]	X_u [sec^{-1}]	Z_w [sec^{-1}]	M_q [sec^{-1}]
NASA	N/A	N/A	N/A	N/A	N/A	N/A
Padfield	-0.0199	-0.3108	-1.8954	-0.0176	-0.3195	-0.4506
Franklin	N/A	N/A	N/A	N/A	N/A	N/A
MATLAB ($N_* = 0$)	-0.0245	-0.3087	-2.5505	-0.0196	-0.3141	-0.6465
MATLAB ($N_* \neq 0$)	-0.0171	-0.3087	-1.1660	-0.0116	-0.3141	-0.3810

with reasonable agreement retaining the term, N_*. The major discrepancies occurred with the Padfield data due to the slight difference in calculating an effective hinge spring and hinge offset. Tuning the hinge offset when the data was absent resulted in better agreement with the original equation.

Table 4.6: Effect of Lateral-Longitudinal Coupling on Derivatives (Set 3)

Aircraft	***CH-47B***			***UH-60***		
(Hover, at SL)	X_u [sec^{-1}]	Z_w [sec^{-1}]	M_q [sec^{-1}]	X_u [sec^{-1}]	Z_w [sec^{-1}]	M_q [sec^{-1}]
NASA	N/A	N/A	N/A	N/A	N/A	N/A
Padfield	N/A	N/A	N/A	N/A	N/A	N/A
Franklin	-0.0210	-0.3000	-1.2300	-0.0240	-0.2900	-0.8200
MATLAB ($N_* = 0$)	-0.0171	-0.3043	-1.2678	-0.0201	-0.2909	-0.3880
MATLAB ($N_* \neq 0$)	-0.0171	-0.3043	-1.2691	-0.0200	-0.2909	-0.3995

For the helicopter used in the flight vehicle tested, many of the physical parameters can be measured on the vehicle, however, several critical parameters had to be estimated similar to the processes described previously. A hinge offset was assumed to be at the end of the blade grip. This value is consistent with what Johnson considers common for hingeless rotor systems. For the hinge spring, a blade bending test was used to determine an approximate spring stiffness. For small deflections, the tip deflection was approximated as $\beta = \nu_{max}/R$, where ν_{max} is the maximum deflection at the tip. The bending test was performed similar to the structural test described in section 2.3. The hinge spring stiffness was determined using eq. 4.23. The resulting value for the blade fundamental frequency parameter was high, but still seems to be within an acceptable value.

$$K_\beta = \frac{PR^2}{\nu_{max}} = \frac{3EI}{R} \tag{4.23}$$

With respect to a single rotor, X_q and M_u are consider cross-coupling derivatives because they provide coupling between the vibrational models. These derivatives were compared versus published data. The impact of these derivatives on the vibration and damping of the vehicle is explored more in the following sections.

Cross-Coupling Derivatives

Table 4.7: Cross-Coupling Derivatives (Set 1)

Aircraft	***BO-105C***	
(Hover, at SL)	X_q $[ft/sec/rad]$	$M_u[rad/ft-s]$
NASA	1.5105	0.0202
Padfield	0.7086	0.1045
Franklin	1.6100	0.0200
MATLAB	1.3058	0.0184

Table 4.8: Cross-Coupling Derivatives (Set 2)

Aircraft	***CH-53D***	
(Hover, at SL)	X_q $[ft/sec/rad]$	$M_u[rad/ft-s]$
NASA	0.8700	0.0060
Padfield	N/A	N/A
Franklin	N/A	N/A
MATLAB	1.0524	0.0021

Table 4.9: Cross-Coupling Derivatives (Set 3)

Aircraft	***CH-47B***	
(Hover, at SL)	X_q $[ft/sec/rad]$	$M_u[rad/ft-s]$
NASA	N/A	N/A
Padfield	N/A	N/A
Franklin	2.5900	0.0093
MATLAB	1.5707	0.0054

These cross-coupling derivatives may have an effect on coupling the in-plane and torsion vibration modes to each other. X_q would provide in in-plane force in response to a pitch rate, which would be realized as a torsion vibration frequency. M_u would provide a torsional moment due to in-plane vibration motion. The cross-coupling will also affect the vehicle stability and flight dynamics. The out-of-plane coupling derivatives, M_w, Z_q, X_w, and Z_u were not presented in the tables, however, this full set of cross-coupling derivatives were included in the higher-fidelity stability model. Johnson provides an equation for M_w for a tandem rotor helicopter, which was modelled.

Control Derivatives

The control derivatives are compared in tables 4.10, 4.11, 4.12, & 4.13. These derivatives did not correlate as closely with the published data as did the stability derivatives. One source of error is the ratio of control input to output. For the rotorcraft presented in NASA [7], data was given for the amount of pilot collective and cyclic inceptor travel and the block diagram for linkage and servo travel as percentage of the inceptor travel. An example of the block diagram from NASA [7] is show in fig. 4.1. The data from [38] for the CH-47B

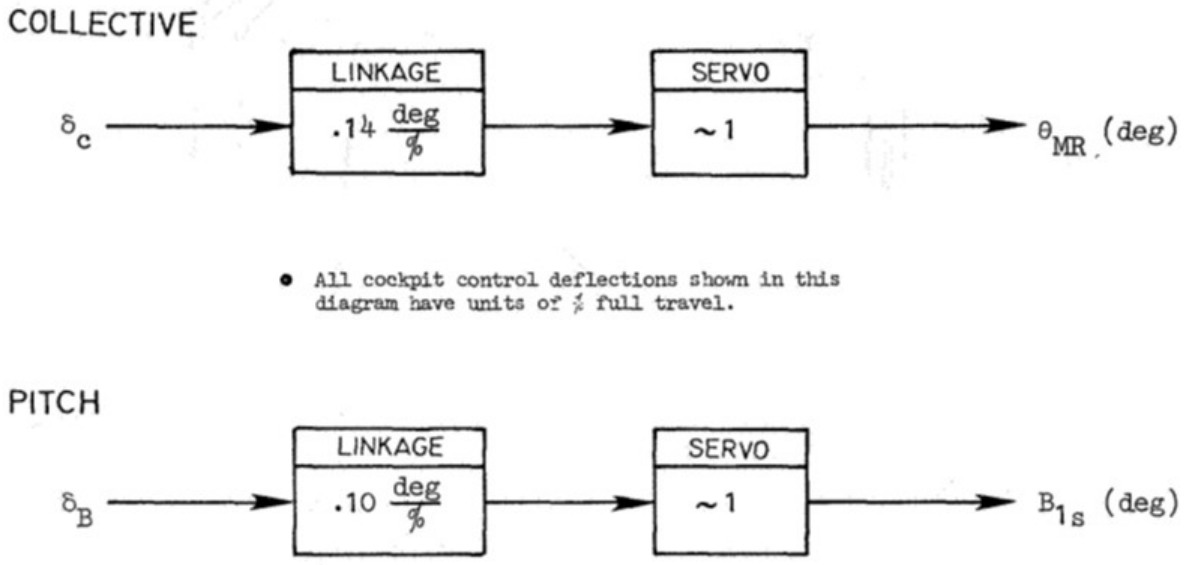

Figure 4.1: Example Control Block Diagram from NASA [7]. Shown: BO-105C Block Diagram

provided values for degrees per inch for collective and cyclic blade angle. Padfield did not provide this information. The values of the control derivatives for Padfield appear to have poor correlation with the other sources, however, this is simply a matter of providing the proper control input to blade angle output ratio. For the aircraft presented in Padfield, the ratio is set to 1 in the MATLAB code. This has reasonable correlation with Padfield's estimates. Another complication may be found in the swashplate geometry. For a swashplate

for the non-rotation frame inputs are arranged apart by 120°, a collective input requires all three actuators to move the same vertical distance, collectively. A 1 unit input vertical with move the swashplate up 1 unit which would, in turn, move the pitch links up by the same amount. If a longitudinal pitch input is commanded, the two actuators attached the points on the swashplate that are displaced laterally, from the centerline, move the same distance, vertically, while the actuator on the centerline, 120° from the others, will move vertically, in the opposite direction. Because the swashplate inputs are rotated 60° off the centerline, an input would yield a swashplate displacement proportional to $1/\cos 60°$, so a 1 unit input yields a 2 unit swashplate displacement. To maintain swashplate height on the mast, the actuator on the centerline has to move proportional to the swashplate. If the swashplate linkages, in the non-rotating frame, are at 90-degree angles, then a 1 unit input yields a 1 unit swashplate displacement. This seems to be accounted for in block diagram, however the block diagram shows the servo output ratio only. For the CH-47B, the tandem rotor arrangement also had the factor of 2 because for collective pitch, the rotors apply the same vertical collective input, but in opposite directions. This is illustrated in fig. 4.2 showing a collective and cyclic input that yields an output blade angle of 10° (for the cyclic input, the blade has been clocked into the position for maximum output). The level swashplate configuration is also shown. This swashplate as the non-rotating inputs spaced at 120° for a longitudinal cyclic command, the input on the centerline has to move twice the distance as the two input linkages that are displaced laterally from the centerline. For a collective input, all three linkages move the same distance. Care must be taken when developing the transfer function for the pilot controls to the actuator output. Different swashplate geometries will impact the transfer function for each individual actuator and could affect the necessary required bandwidth of the actuators for a particular swashplate motion.

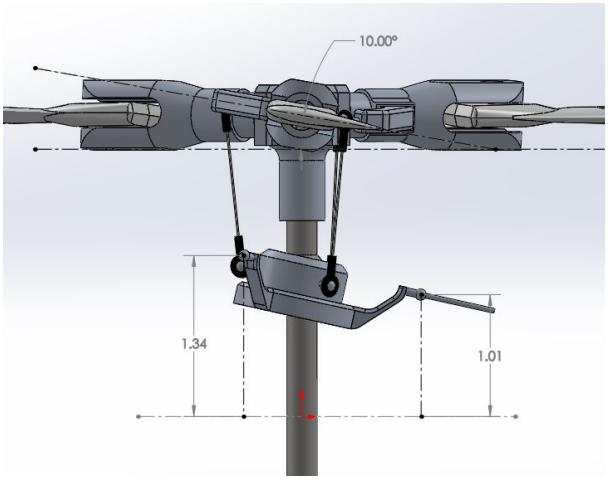

(a) Swashplate with Cyclic Input

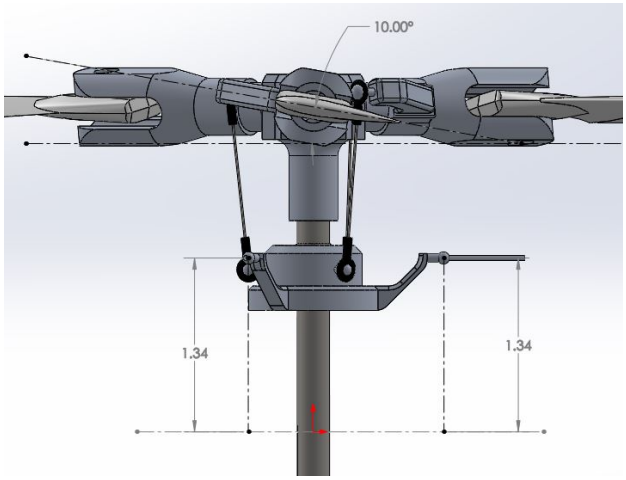

(b) Swashplate with Collective Input

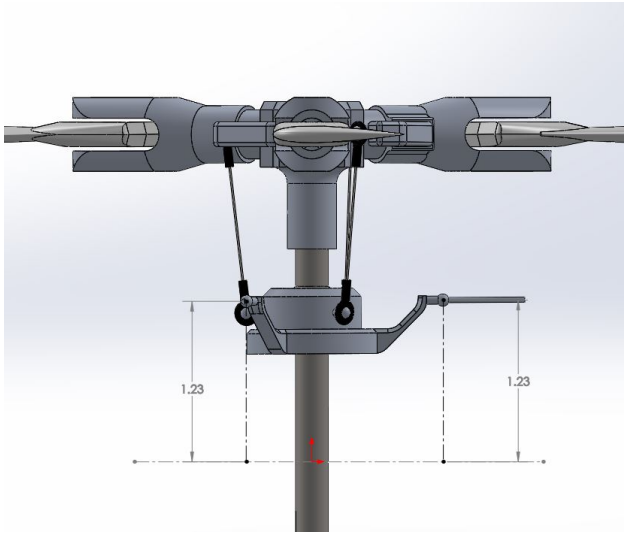

(c) Swashplate Level

Figure 4.2: Output Blade Angle and Linkage Displacement for Different Swashplate Inputs

Table 4.10: Rotor Control Derivatives Validation (Set 1)

Aircraft	***BO-105C***		
(Hover, at SL)	X_{θ_s} $[ft/s^2/in]$	$Z_{\theta_0}[ft/s^2/in]$	$M_{\theta_s}[rad/s^2/in]$
NASA	0.7894	-9.8810	-0.9727
Padfield†	-8.4769	-92.9573	44.9965
Franklin	0.7900	-9.8000	-0.9700
MATLAB	0.4888	-8.6071	-0.6733

Table 4.11: Rotor Control Derivatives Validation (Set 2)

Aircraft	***Lynx ZD559***		
(Hover, at SL)	X_{θ_s} $[m/s^2rad]$	$Z_{\theta_0}[m/s^2rad]$	$M_{\theta_s}[rad/s^2]$
NASA	N/A	N/A	N/A
Padfield†	-9.2860	-93.9179	26.4011
Franklin	N/A	N/A	N/A
MATLAB	-10.6113	-93.7883	28.8956

Table 4.12: Rotor Control Derivatives Validation (Set 3)

Aircraft	***CH-53D***		
(Hover, at SL)	X_{θ_s} $[ft/s^2/in]$	$Z_{\theta_0}[ft/s^2/in]$	$M_{\theta_s}[rad/s^2/in]$
NASA	1.5194	-6.3839	-0.1791
Padfield	N/A	N/A	N/A
Franklin	N/A	N/A	N/A
MATLAB	1.3448	-6.4406	-0.1763

Table 4.13: Rotor Control Derivatives vs. RPM (Set 4)

Aircraft	***CH-47B***		
(Hover, at SL)	X_{θ_s} $[ft/s^2/in]$	$Z_{\theta_0}[ft/s^2/in]$	$M_{\theta_s}[rad/s^2/in]$
NASA	N/A	N/A	N/A
Padfield	N/A	N/A	N/A
Franklin	0.1140	-8.0600	0.3300
MATLAB	-0.7024‡	-9.5369	0.3120

†Padfield [42] does not provide linkage data for control input/output ratio. Ratio is set to 1:1 for the analysis. Additionally, the Padfield control derivatives do not have units per inch.

‡The major discrepancy is likely because longitudinal control for a tandem rotor is by differential collective pitch. This control does not generate in-plane force, X_{θ_s}, unless there is tilt of the rotor masts.

Test Vehicle Rotors

After the code was validated, the stability and control derivatives for the rotors used on the test vehicle were calculated. The atmospheric conditions are taken at sea level standard day and the thrust is chosen to balance the complete vehicle in hover. Tables 4.15, 4.16, & 4.17 explore how the stability and control derivatives vary with changes in thrust and RPM. For subsequent calculations, the RPM is set to approximately 1680 RPM or 28 Hz, which was the baseline RPM during flight testing. Mass properties of the helicopters were determined by physical measurements and numerically from the CAD model. The CAD model was used specifically to obtain the moments of inertia for the single rotor units and the complete airframe. When necessary, such as with the fuselage in torsion, the mass properties of half of the vehicle can be measured. This is a unique advantage of the CAD model. Unfortunately, the mass properties can be significantly flawed when care is not taken. The initial CAD model of the blade provided an estimate of the flapping moment of inertia. This value was producing values for the rotor that appeared to be erroneous. Based on a technique presented by Prouty [47], the moment of inertia was experimentally calculated. This was performed by measuring the weight and center of mass of the blade, then treating the blade as a pendulum and measuring the period of oscillation. An average value was used to approximate the moment of inertia. When compared to the CAD model, this was significantly different. Measuring the moments of inertia for the complete vehicle is not as trivial and the CAD model is still used for estimations. When necessary, mass was added to the CAD model to match the weight of the components to better predict the mass properties. Because the CAD model does not account for all of the components, materials, and weight distributions, the moments of inertia are approximate. Due to the configuration, there was some difficulty determining what moment of inertia to use for the couple structural-aerodynamic model. The rotor unit does not contain the flight battery and the aft part of the fuselage and tail rotor have been eliminated. When comparing the non-dimensional radius of gyration, k_y,

Table 4.14: Comparison of Rotor Parameters

Rotor Parameter Comparison			
Aircraft	***BO-105***	***Lynx ZD559***	***Blade 360 CFX Trio***
k_y	0.3111	0.2805	0.2491
M^*	115.1079	130.2748	127.1653
${I_{yy}}^*$	11.1427	10.2519	7.888
C_T	0.0047	0.0052	0.0026
γ	5.3584	7.1099	6.5219
ν	1.1233	1.1359	1.0529
σ	0.0700	0.0778	0.0662

and the non-dimensional mass, M^*, were similar to values for other aircraft compared. In the equations for the stability and control derivatives, M^* and ${I_{yy}}^* = k_y^2 M^*$ are in the denominators for force and moment terms, respectively. Table 4.14 show the comparison of these values and other rotor parameters that govern the stability and control derivatives. Larger values of M^* and ${I_{yy}}^*$ will reduce the force and moment derivatives, affecting the correlation of the calculated values with the published data for other aircraft.

Additionally, the rotor is generating more lift than the weight of rotor unit because of the weight of the other components, such as the fuselage and electronics, that are not considered in the mass model for the aerodynamics. This affects the force derivatives, and it can be noticed that X_u and Z_w are also higher than what might be expected.

The hinge spring constant was calculated by treating the blade and blade grip as a cantilever beam in bending and measuring the deflection under a static load. The blade, by itself, in bending, has a value of approximately 18 $ft - lbs/rad$ while, the blade plus the blade grip attached to the rotor head has a value of approximately 3.5 $ft{-}lbs/rad$ for small deflection of blade flapping. A value of 3.5 $ft{-}lbs/rad$ provides good correlation with stability and control

derivative data of other aircraft. If the connection to the rotor head was stiffer, the bending would occur further outboard and the spring constant would be more representative of the value calculated for the blade, but due to the compliance in the connection of the feathering shaft to the rotor head and the rubber dampers, the blade system more likely flexes near this connection at the lower values calculated and used. This, however, should only be taken as an initial approximation.

Table 4.15: Rotor Stability Derivatives vs. RPM

Aircraft	***Blade 360 CFX Trio***		
(Hover, at SL) (Thrust = 3 lbs)	X_u [sec^{-1}]	Z_w [sec^{-1}]	M_q [sec^{-1}]
RPM = 1080	-0.0802	-1.0170	-10.6093
RPM = 1680	-0.0343	-1.3569	-6.5745
RPM = 2280	-0.0257	-1.6121	-4.6133

Table 4.16: Rotor Stability Derivatives vs. Thrust

Aircraft	***Blade 360 CFX Trio***		
(Hover, at SL) (RPM = 1680)	X_u [sec^{-1}]	Z_w [sec^{-1}]	M_q [sec^{-1}]
Thrust = 3 lbs	-0.0343	-1.3569	-6.5745
Thrust = 4 lbs	-0.0373	-1.0751	-5.1051
Thrust = 5 lbs	-0.0412	-0.8945	-4.2301

Table 4.17: Rotor Control Derivatives vs. RPM

Aircraft	***Blade 360 CFX Trio***		
(Hover, at SL) (Thrust = 3 lbs)	X_{θ_s} $[ft/s^2/in]$	$Z_{\theta_0}[ft/s^2/in]$	$M_{\theta_s}[rad/s^2/in]$
RPM = 1080	0.5890	-4.0148	-5.6855
RPM = 1680	0.5891	-8.3323	-6.2566
RPM = 2280	0.5798	-13.4349	-6.3645

Interestingly, when the RPM is increased, the damping derivatives X_u and M_q decrease while Z_w increases. During the test flight, when the RPM was increased just prior to failure, it appears that the in-plane damping decreased while the out-of-plane damping increased. The decrease in the in-plane damping would have increase the likelihood of damage.

4.3 Physics Model

A mathematical reduced-order model was developed to incorporate damping into the structural vibration model. The initial intent was to incorporate the damping derivatives into the finite element model. This proved to be difficult and extremely time consuming with no promising results. This prompted the development of the reduced-order model to capture the effects of aerodynamic damping in the structural vibrations. Additionally, an accurate and robust reduced-order model would be ideally incorporated in initial conceptual or preliminary design. The model is fast to modify and run to test responses to changes in parameters either individually or over a spectrum of values. Starting with a simple mass-spring-damper model, eq. 4.24, the spring constants come from the fuselage structure and the damping constants come from the aerodynamic stability derivatives from the previous section.

$$m\ddot{x} + c\dot{x} + kx = F(t) \tag{4.24}$$

The complete fuselage frame is shown in fig. 4.3. For the analysis, the complete frame is decoupled into two main sub blocks to represent the fuselage bending & torsional modes and the frame arm bending & torsional modes, shown in fig. 16. In the physics model, the rotor units, batteries, and electronics are replaced by equivalent masses. Additionally, the arm and fuselage geometry are numerically simplified. The arm structural members are assumed to be simple springs added together in series and parallel for out-of-plane bending. For in-plane bending of the arms, the strut brace is assumed to sufficiently stiffen the structure to

Figure 4.3: Complete Frame Configuration (Frame Design Three)

eliminate in-plane bending inside of the intersection. Only unsupported tubes outside of the joint are considered compliant. The frame tube couplers and their effects on the stiffness of the frame are not considered and the rotors are assumed to be rigidly connected at the ends of the arm.

4.3.1 Spring Constants

Starting with $\nu_{max} = -PL^3/3EI$ and $\theta_{max} = TL/GJ$, the maximum displacement for bending and torsion of a cantilever member presented in section 2.3, we rearrange the equations to get the effective spring constants due to the structure. This is analogous to $F/x = k_B$

(a) Arm Section (b) Fuselage Section

Figure 4.4: Frame Decoupling for Analysis

and $T/\theta = k_\tau$.

$$k_B = \frac{P}{\nu_{max}} = \frac{3EI}{L^3} \tag{4.25}$$

$$k_\tau = \frac{T}{\theta_{max}} = \frac{GJ}{L} \tag{4.26}$$

For structural configurations with more than one structural member, the structural elements are added in series or parallel accordingly. Using Palm [41], for a cantilever beam with a mass at the end, the equivalent lumped mass, m_e and lumped inertia, I_e is given by:

$$m_e = m_c + 0.23m_d \tag{4.27}$$

$$I_e = I_c + I_d/3 \tag{4.28}$$

where m_c and I_c are the mass at the end of the beam & the inertia of that mass, respectively and m_d and I_d are the distributed mass of the beam & distributed inertia of the beam,

respectively. The natural frequency of the bending and torsion modes are given by eqs. 4.29 & 4.30.

$$\omega_n = \sqrt{k_B/m_e} \tag{4.29}$$

$$\omega_\tau = \sqrt{k_\tau/I_e} \tag{4.30}$$

The cross-section of the structural members are circular tubes where the area moment of inertia for the cross-section is given by:

$$I = \frac{1}{4}\pi \left(R_o^4 - R_i^4\right) \tag{4.31}$$

4.3.2 Damping Constants

The aerodynamic damping constants for each vibrational mode were related the appropriate stability derivatives. X_u provides damping for in-plane motion, Z_w provides damping for out-of-plane motion, and M_q provides damping for torsional motion of the arm. For the special case of fuselage torsional motion, the pair of rotors behave like a tandem rotor configuration with a pitching motion, so the damping comes from the moment generated by the heaving motion of the rotor at a distance from the fuselage axis. The damping constant can be represented by $M_{q,\ tandem}$, eq. 4.16 with an appropriate estimated moment of inertia. To compute the relative damping ratios, the theoretical critical damping constant was found based on the natural frequency as calculated previously for each mode.

$$c_{crit} = 2\sqrt{k_B m_e} \tag{4.32}$$

$$c_{\tau\ crit} = 2\sqrt{k_\tau I_e} \tag{4.33}$$

4.3.3 Vibration Transmissibility

The equation for vibration displacement transmissibility from Palm [41], eq. 4.34, is used to assess the un-damped natural frequencies of each mode in addition to the effect of aerodynamic damping. The transmissibility equation is a ratio of the response of a plant to the input vibration. By providing a damping ratio and sweeping through a range of vibration frequencies, the response of the plant is easy to characterize. This was convenient to use in this context as the damping ratio could be easily calculated in the structural code module and the damping in a separate module. Additionally, by setting the damping ratio to zero, the un-damped response could easily be shown with the damped response. The vibration transmissibility equation provided a nice visualization for the effect of damping, showing the reduction in the peak amplitude of each mode. The results are calculated in decibels for convenience of scale.

$$\left|\frac{X(j\omega)}{Y(j\omega)}\right| = \frac{X}{Y} = \sqrt{\frac{4\zeta^2 r^2 + 1}{(1-r^2)^2 + 4\zeta^2 r^2}}\ , \quad r = \frac{\omega}{\omega_n} \tag{4.34}$$

4.4 Vibration Analysis Preliminary Results

The vibration analysis is broken up into the distinct decoupling of the model: the arm appendages bending in plane, out of plane, and the arm in torsion followed by the fuselage bending in plane, out of plane, and the fuselage in torsion. This current study does not address the coupling between the fuselage modes and the arm appendage modes. For each

harmonic, the case with no damping is overlayed on the output with damping and shown as a dashed line. Because the damping ratios are small, there is not an appreciable difference between the damped natural frequency and the un-damped natural frequency. The main distinction is the reduction in vibration transmissibility peak amplitude values.

Table 4.18: FEA Prediction vs. Reduced-Order Model Prediction for Principal Modes

Mode	***FEA Predicted Frequency***	***Reduced-Order Predicted Frequency***
Fuselage torsion	11 Hz	11.0 Hz
Fuselage in-plane bending	16 Hz	16.9 Hz
Arm in-plane bending	36 Hz	36.2 Hz

4.4.1 Arm Appendages

The structural configuration for the arm analysis is shown in fig. 4.5. The main arm structural member extends from the fuselage to the rotor unit. A strut brace extends from the fuselage and meets with the continuous arm structure at approximately half the length of the arm and at a 45 deg angle. The outboard section of the arm is unsupported. This structural arrangement is mathematically treated as a cantilever beam outboard of the strut brace for in-plane bending. For out-of-plane bending, the structural members are added together, as springs, in parallel and series to form an equivalent bending member.

Figure 4.5: Initial Frame concept (without strut-braces)

The geometric parameters, such as length and mass, are 'tuned' to account for the small compliance in the tube couplers and the strut brace. Modifications to the length of the member was chosen as the primary method to tune resulting natural frequency of the vibration mode. This is used in lieu of changing the material properties, cross-section geometry, or applying a multiplication constant. The values of the un-damped natural frequencies were compared to the FEA data and flight test data for validation. Table 3.2 shows the predicted frequencies of the first three vibration modes for frame design one. The first two modes are fuselage torsion and bending modes. The third mode shape is the arm appendages bending in plane. This is a symmetric bending mode and characteristically, the FEA model shows most of the bending compliance happens outboard of the strut brace. This validates the assumption for the reduced-order model to treat the frame as rigid inboard of the strut brace. As mentioned previously, the arm lengths are 'tuned' to account for the small amount of compliance of other structural members contributing to this bending mode. Comparing the values of un-damped natural frequency, we can see good agreement with the reduced-order model.

Figure 4.6: Frame Arm Appendage Structural Failure

Figure 4.6 shows one instance of damage sustained during hover. During this event, the arm appendages vibrated in plane and two of the appendages separate from the vehicle. The figure shows that the failure in the structural member occurred at the strut brace, which is consistent with the FEA predicted mode shape and the assumptions used in the reduced-order model.

Figure 4.7 shows the acceleration power spectral density plot from this event. The RPM was increased just prior to failure and the data shows a frequency of approximately 38 Hz at the time of the event. The predicted frequency from the FEA analysis and the reduced-order model are in good agreement with flight data. Additionally, the mode shape of the vibrations seen at the time of failure visually match the FEA prediction, further building confidence that this adequately represented the failure mode, and that the main rotor RPM excited this mode.

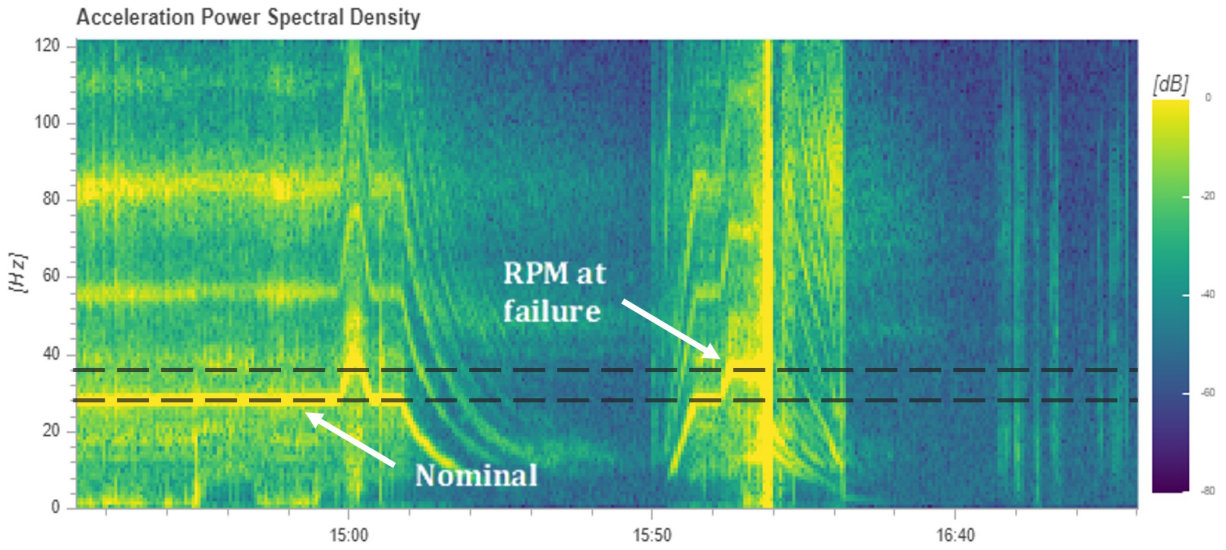

Figure 4.7: Acceleration Power Spectral Density Plot during Arm Failure

Figure 4.8 shows the vibration transmissibility for the in-plane, out-of-plane, and torsional arm bending modes. The un-damped response is overlayed on the damped response to show the effect of considering aerodynamic damping in the mass-spring-damper model and the relative magnitude of the two modes when compared with each other. The difference of the natural frequencies of the in-plane and out-of-plane bending modes is due to the difference in the frame geometry of the test vehicle. For a frame without a strut brace and that has a uniform cross-section, the in-plane and out-of-plane bending mode natural frequencies would be nearly identical and the damped response would be proportional to the ratio of the respective damping ratios. Comparing the damping derivatives X_u and Z_w for helicopter

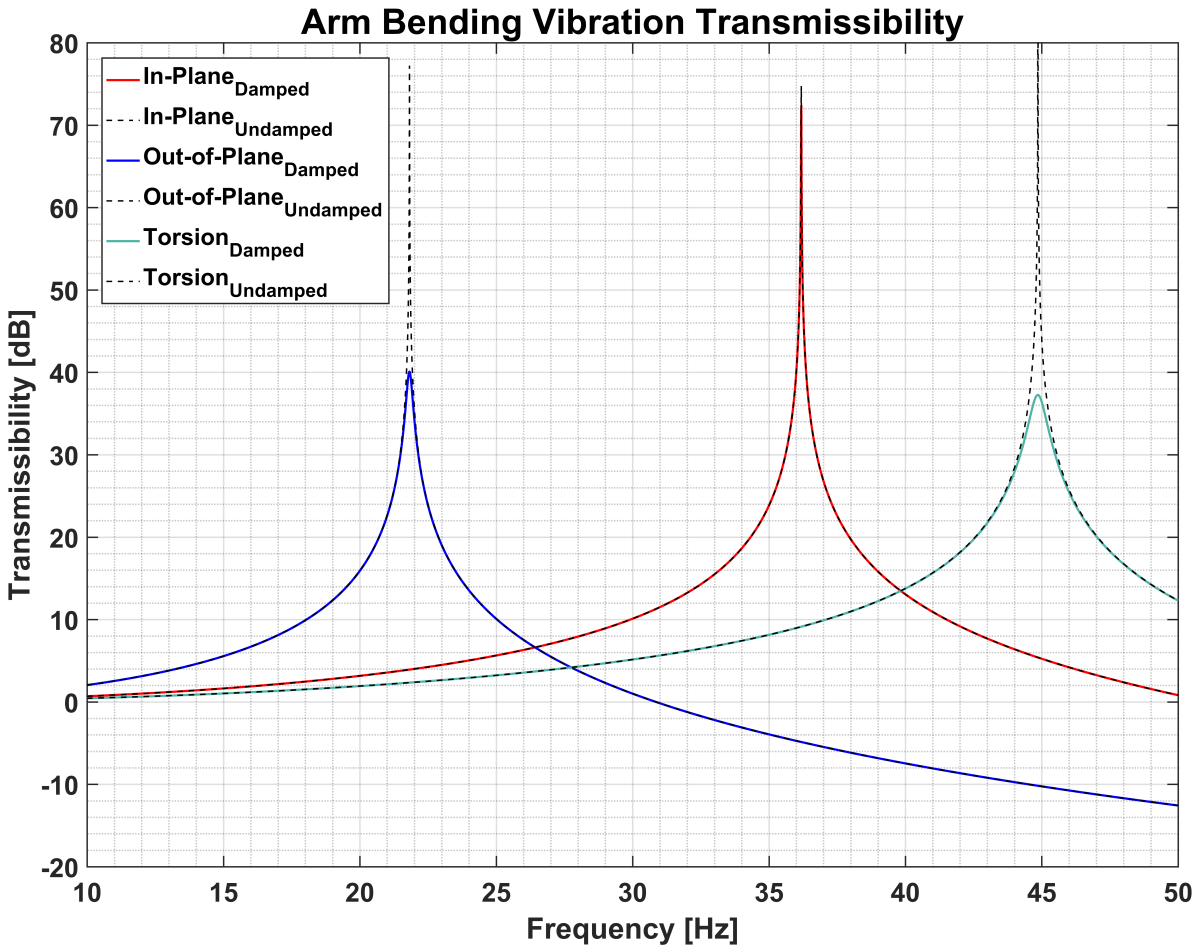

Figure 4.8: Arm Appendage Vibration Transmissibility

data presented, the magnitude of Z_w is typically on the order of ten times larger than X_u. For the rotor used with this airframe, the ratio of $Z_w/X_u \approx 39$. The large ratio is likely due, in part, to the fact that the rotors are producing more thrust than the weight of the rotor units. Because the fuselage frame and batteries make up a significant portion of the overall aircraft weight, the mass and inertia of the rotor units is significantly smaller than what would be typical of a conventional helicopter, for the same thrust. The vibration transmissibility analysis shows nearly a 40 dB reduction in transmissibility, for this frame configuration, when damping is considered. This large difference may have contributed to the initial in-plane arm bending failure. The natural frequencies of the in-plane and out-of-plane arm bending modes are both within the operating range of the rotor RPM. While

the vehicle RPM was near the in-plane bending natural frequency at failure, the vehicle RPM envelope was explored without failure until this higher RPM was reached. Table 3.1 describes that high vibrations were encountered below approximately 1500 RPM. This may explain some of those vibrations. While the arm out-of-plane bending mode is significantly more damped than the arm in-plane bending mode, the damping ratio is small, and the mode is still under-damped. At this lower RPM, there is less energy being delivered to the frame, from the rotors, so this may also contribute to some of the lower frequency modes being less susceptible to damage, especially if they are more damped than a neighboring mode.

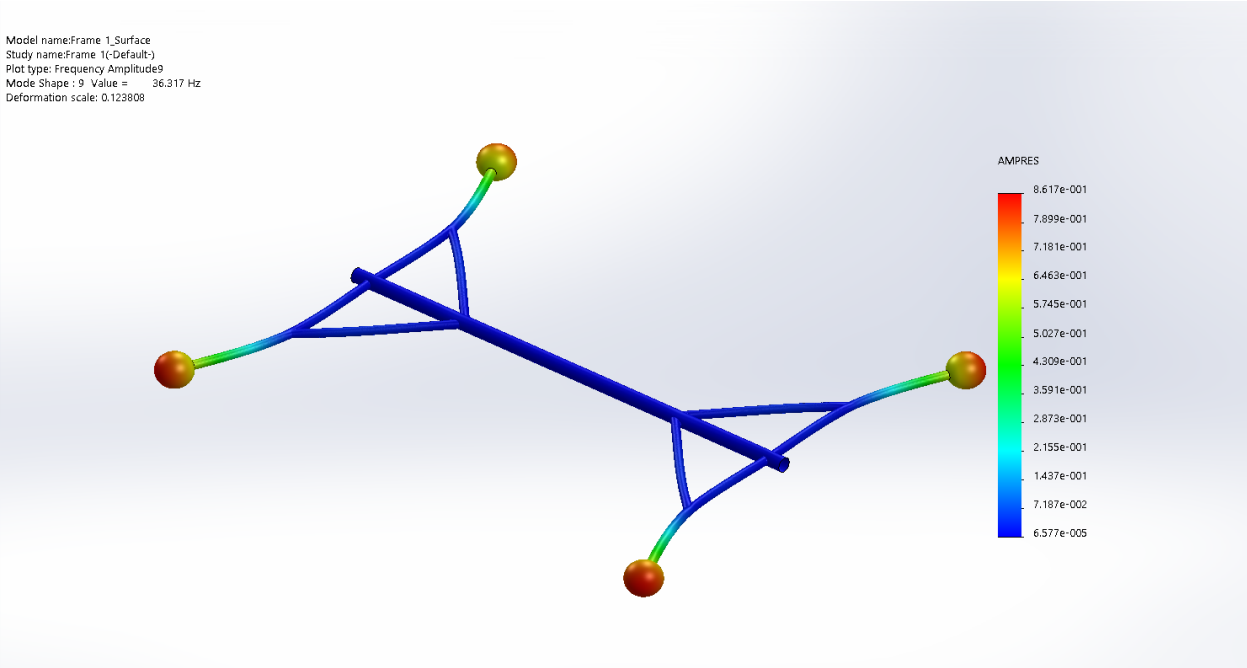

Figure 4.9: Finite Element Predicted Mode Shape Resembling Arm Failure

The torsional mode of the arms is important to consider due to control inputs to the vehicle. The current control scheme uses only cyclic pitch for pitch, roll, and yaw control of the complete vehicle. High frequency inputs may have the potential to excite the torsional mode of the arms. The damping for this mode is realized as the pitch damping derivative, M_q, of the rotor. $M_q/Z_w \approx 4.8$ for the rotors used on the vehicle and is significantly more damped

than the other arm modes. The damping ratio, however, remains well below being critically damped so this mode can be excited, in flight, through vehicle dynamics or control inputs. The analytical model shows that the natural frequency is near the upper limit of the rotor RPM, however a higher fidelity estimate of the moment of inertia of the rotor could show a decrease in the natural frequency.

4.4.2 Fuselage

Figure 4.10: Frame Design Two

The structural configuration for the fuselage analysis is shown in fig. 4.10. For the initial analysis, only half of the fuselage was considered, and the fuselage was treated as a cantilever beam fixed at the center of the frame at the vehicle C.G. The two rotor units, propulsion battery, and additional frame structure are treated as a single mass at the free end of the fuselage tube. The fuselage structural member is a tube that has the same cross-sectional properties for in-plane and out-of-plane bending, the so the predicted un-damped natural frequency should be the same for both. The material properties of the fuselage structural member are the same as the arm structural members.

Similar to the arm analysis, modifications to the length and of the fuselage structural member and the masses were used to tune resulting natural frequency of the vibration mode. The values of the un-damped natural frequencies were compared to the FEA data and flight

test data for validation. Table 3.3 shows the predicted frequencies of the first three vibration modes for frame design two. The first two modes are fuselage torsion and bending modes. The symmetry of the fuselage tube places the in-plane and out-of-plane bending natural frequencies at approximately the same value. Because of the symmetry of the vehicle, the first assumption treats the vehicle as a cantilever beam fix at the center of the tube, corresponding the vehicle CG. While the results of the model had good correlation to the FEA model, this may not be the most appropriate representation of the bending modes. The fuselage bending modes more closely represent an unconstrained tube in bending. The current frame has large, localized masses near what would be considered the free ends of the cantilever beams. As Venkatesan & Friedmann [16] describe in their analysis, it can be shown that if you have an unrestrained beam with concentrated masses, if the concentrated mass at the center of the beam is at least three times larger than the mass of the beam, the vibratory mode approaches that of a cantilever beam clamped at the center. The concentrated masses at the tips transform the system into one that is closely related to the that of a cantilever beam with a tip mass. Certain modes can be better approximated as a simple cantilever beam than others. The arms bending in plane and arms in torsion are approximated well as a cantilever beam with a tip mass. The arms bending out of plane and the fuselage bending in plane or out of plane will have more dependence on the mass distribution of the components. With more evenly distributed masses, the cantilever beam approximation may begin to breakdown. A more appropriate model would be the lumped-mass model. As

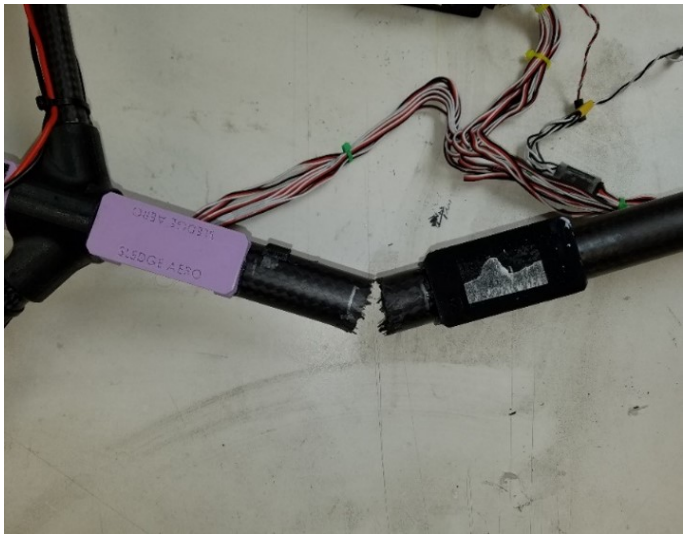

Figure 4.11: Fuselage Frame Structural Failure

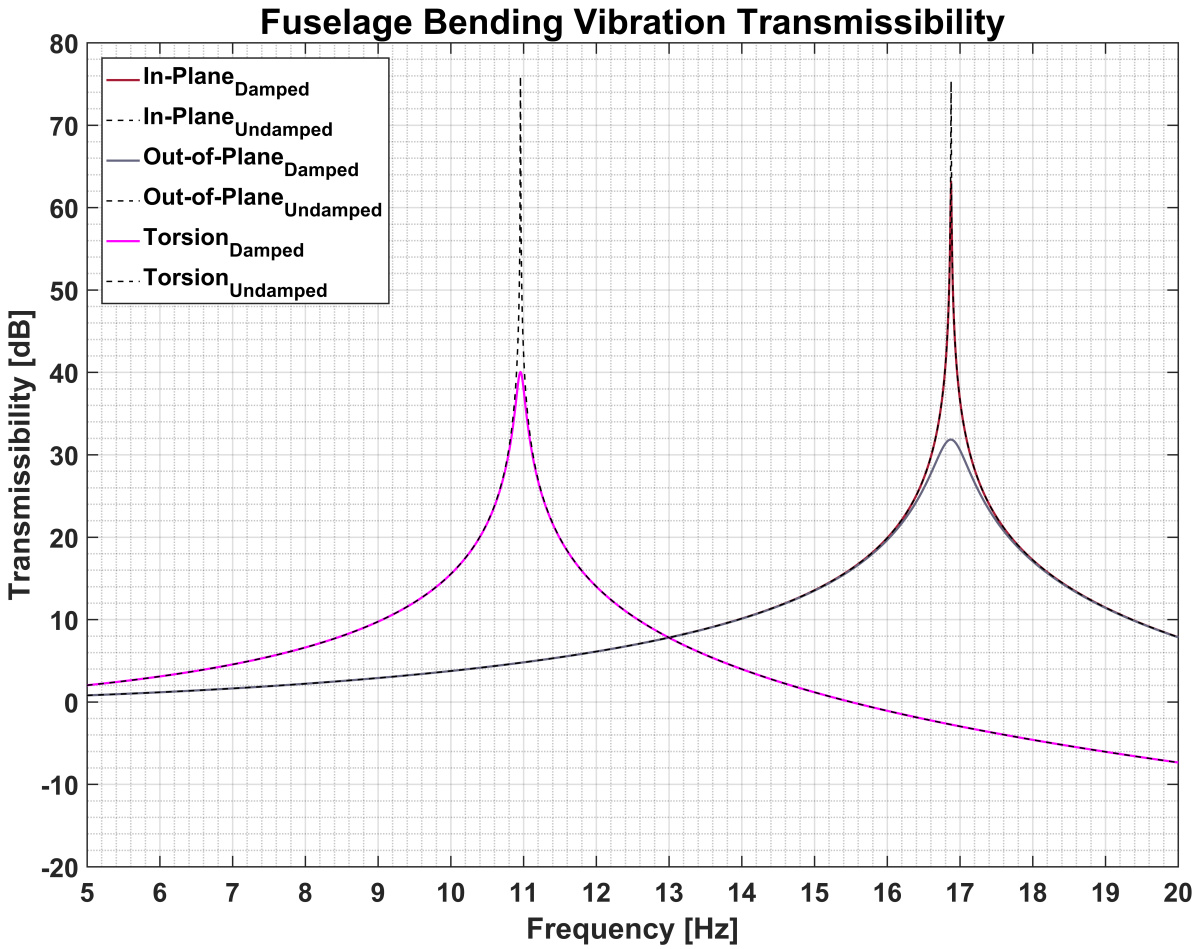

Figure 4.12: Fuselage Vibration Transmissibility

described in Aeroelasticity by Bisplinghoff, Ashley, & Halfman [48], the lumped-mass model approximates the system by breaking up the system into lumped masses and lumped inertias. A more accurate approximation of the natural frequency can be obtained for an arbitrary system. For the torsional mode, the first symmetric mode is a rigid-body mode, so the first vibratory mode is an antisymmetric mode, with the node at the center of the frame due to frame symmetry. The large battery mass, frame mass, and two rotor units concentrated at the free end allows the mode to be well represented as a cantilever beam in torsion where the center node of the frame is the fixed end. The analysis of the vibration transmissibility shows the two bending modes have a predicted natural frequency near 18 hertz while the torsion mode has a natural frequency near 11 hertz. The in-plane bending mode has the lowest

damping and the highest vibration transmissibility. The in-plane damping comes from X_u for the rotor pair. The highest damped mode is the out-of-plane bending mode of the fuselage. For the out-of-plane bending mode, the frame arms are assumed rigid, so the damping comes from the heaving motion of two rotors. The ratio of the damping derivatives for the fuselage in bending is $[2Z_w/2X_u]_{tandem} \approx 39$, which is the same as for the arms, however, the overall transmissibility of both bending modes and the out-of-plane bending mode has the lowest vibration transmissibility of the fuselage modes. The torsional mode has higher transmissibility than the out-of-plane bending mode, but significantly less transmissibility than the in-plane bending mode. The damping comes from the heaving motion of the pair of rotors in opposite directions at a distance, r, from the fuselage tube axis. If the rotor geometry can transfer moments to the hub, then this also contributes to the damping, $M_{q,tandem}$. While this damping mechanism can be significant, the large inertia of the two rotor systems plus the frame and batteries reduce the damping derivative. This explains why the single rotor in torsion has higher damping than the pair of rotors, because the inertia of a single rotor is considerably smaller. This is not typical as a tandem helicopter usually has higher pitch damping when compare to a single rotor helicopter. A change in mass distribution on the frame would change the spread in the vibration transmissibility.

Because the fuselage modes are not as close the rotor RPM as the arm bending modes, it was, at first, not clear what was exciting the mode. It is possible the other energy content at a frequency close the natural frequencies was responsible, but there may be another mechanism. The servo actuators have a max speed close the natural frequencies of the fuselage bending modes. This will be elaborated on in a following section and should certainly be considered during the frame design and control allocation.

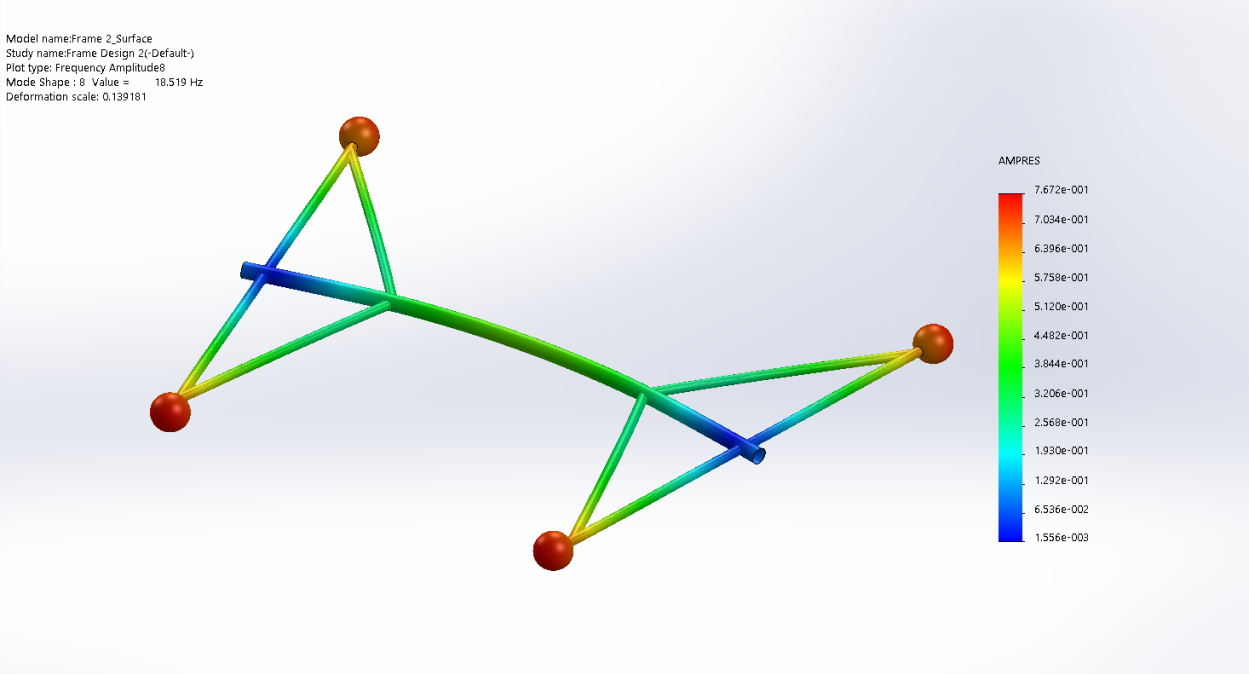

Figure 4.13: Finite Element Predicted Mode Shape Resembling Fuselage Failure

4.4.3 The Complete System

The compilation of the damped vibration transmissibility is shown in fig. 4.14. When aerodynamic damping from the rotors is considered, there is a hierarchy of transmissibility peak values. The arm in-plane bending mode has the highest peak value at approximately 72 dB. The fuselage in-plane bending mode is the second highest peak value at approximately 64 dB. The remaining modes are at least two decades lower in peak values. What is interesting is that the data resembles a 'timeline' of how the aircraft sustained damage during testing. The vibration transmissibility values should not be taken as absolute strength or amplitude but used as a gauge of dangerous arrangements of the vehicle structure, operational RPMs, and control system frequencies.

During testing, the first minor and major damage occurred in the arms vibrating in plane. Super imposed on the graph is the measured RPM from the acceleration power spectral density plot from the event. The damped natural frequency is near the RPM of the vehicle

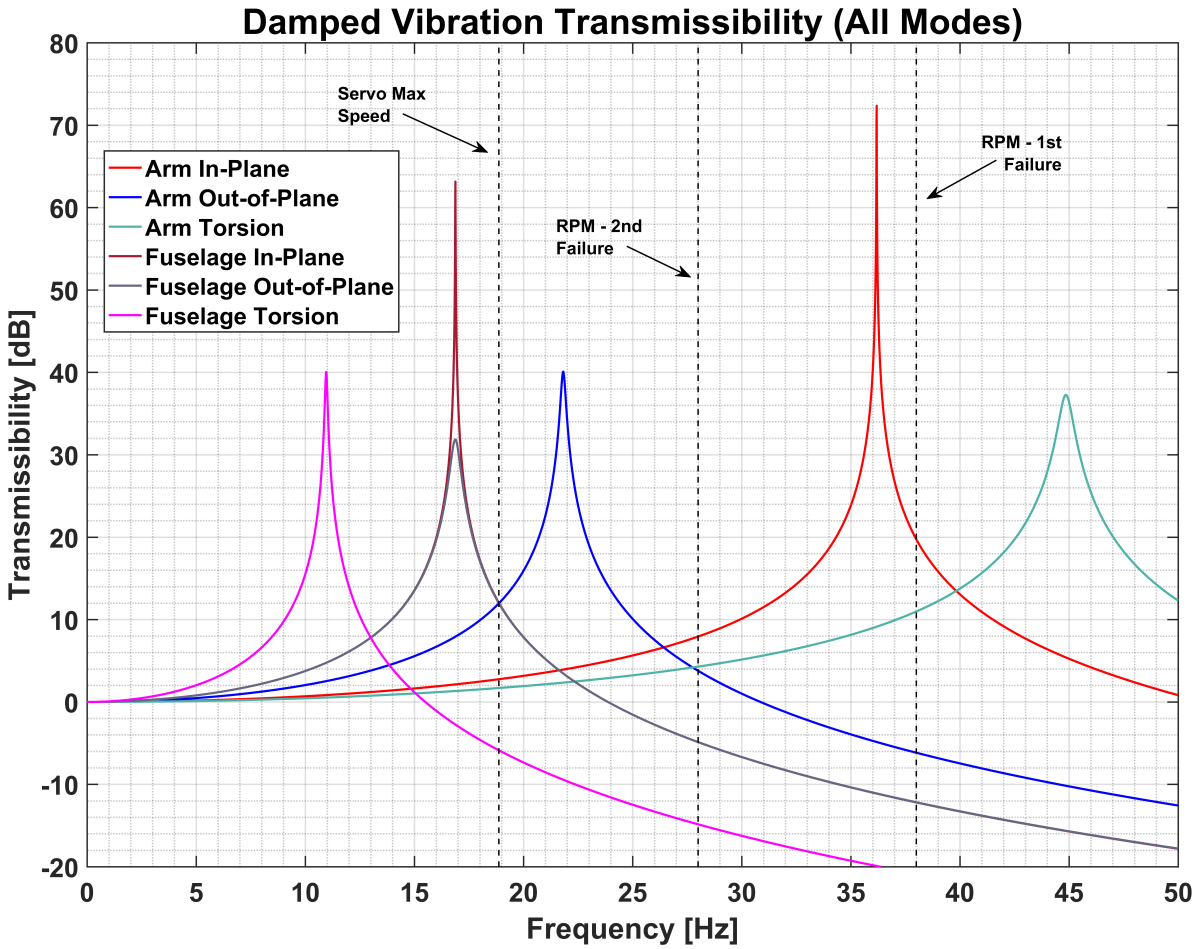

Figure 4.14: Airframe Vibration Transmissibility (Complete Picture)

at failure and this mode is the most susceptible to being excited by the rotor RPM (1P). The second major damage occurred with the fuselage vibrating in plane. While this is the second most susceptible mode to excitation, the RPM during this event was not close the predicted damped natural frequency, however, this mode is within the bandwidth of the servo actuators used for the cyclic and collective control. This is discussed more in the following section. While there are other modes near the maximum frequency of the servo actuators, the fuselage in-plane bending mode was significantly more susceptible to excitation and this was realized as airframe damage. The data seems to indicate that the fuselage torsional mode and the arms out-of-plane bending mode remain susceptible to excitation during operation

as they are within the actuator maximum speed and have relatively high transmissibility with respect to the remaining modes.

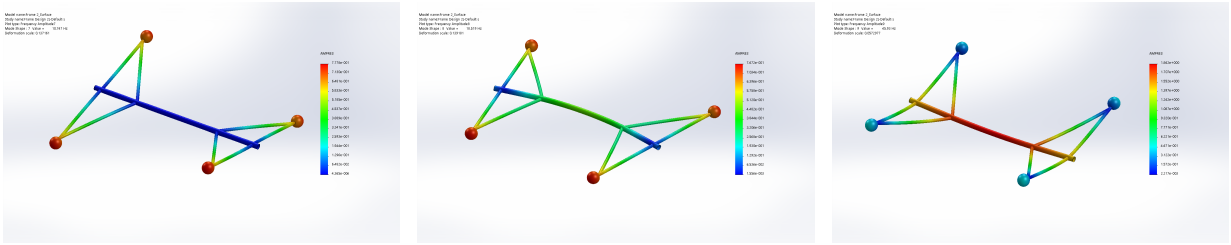

(a) First (b) Second (c) Third

Figure 4.15: First six mode shapes for frame design two without fuselage masses (from the top left to right)

The fuselage out-of-plane and arm out-of-plane modes shown are predicted from the reduced-order model but may not exist independently of one another. When the fuselage bends out of plane, the root of the arms would experience the same deflection as the end of the fuselage structure, however, the large masses at the ends of the arms would cause bending in the arms. The coupling of these modes and the close proximity of the damped natural frequencies may encourage these modes to become a coupled bending mode of the fuselage and arms. Figure 4.16 shows a similar mode, however, because the large battery mass, control system mass, wiring, and auxiliary components located on the fuselage are not included in this FEA model, this mode shape and predicted frequency are not correct. As discussed in section 4.4.2 regarding the fuselage analysis, the assumption of treating the decoupled model as groups of cantilever beams may neglect some of the structural dynamics of the vehicle. This is especially true

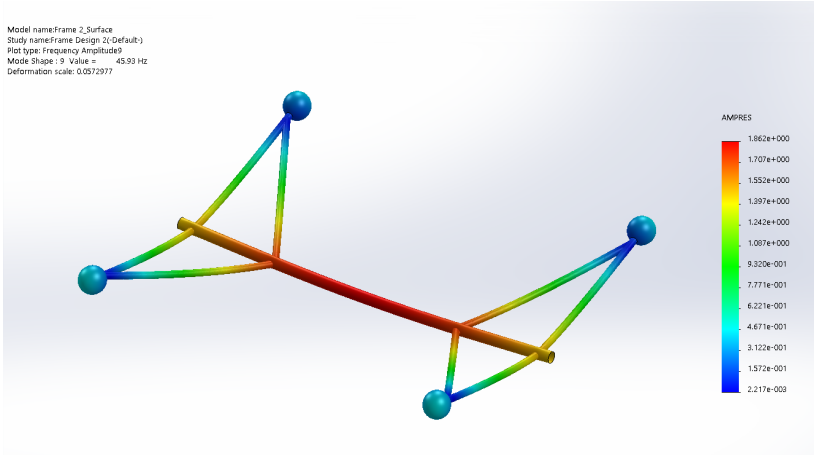

Figure 4.16: Arm Out-of-Plane Bending with Fuselage Motion

if the mass distribution changes. The current analysis does not use the lumped-mass model to calculate the natural frequencies of the system, however this should be implemented in future work. It would also reduce amount of 'tuning' and calibration the simple model will need to match the FEA model and the test data.

4.4.4 Mode excitation by actuator input

During testing, the second instance of major damage, shown in fig.4.11, due to structural vibration occurred as a fuselage in-plane bending mode showing fig.4.13. The predicted frequency for this mode is approximately 18 hertz, seen in table 3.3 and approximately 17 hertz as predicted by the the physics model, seen in fig.4.12. When this damaged occurred, the rotor RPM was approximately 1680 RPM (28 hertz). At the time, it was not clear what mechanism was adding energy to this flexible mode. Even though this mode has lower damping than other vibration modes, the predicted natural frequency was still far away from the rotor RPM, which seemed to be what instigated the first occurrence of major structural damage. The first occurrence of major structural damage occurred with the arms bending in plane and the fuselage bending in plane has a similar damping mechanism. While these are related, the connection was tenuous between the two modes regarding how the vibration was initiated. Additionally, there did not appear to be other elements on the airframe that were vibrating near this frequency, that could have possibly initiate the vibration mode.

Upon further analysis, it seems that resonance with the rotor actuators, specifically differential cyclic for yaw control, may have initiated the in-plane fuselage bending mode. Typical multirotor vehicles use varying RPM for yaw control. For a quadrotor, the RPM of the rotors across the diagonal changes while the RPM of the other pair of rotors changes by the same magnitude but in the opposite sense. This increase and decrease in thrust across the diagonal would be realized as a fuselage torsional bending mode. If a quadrotor vehicle were to control

with pure collective pitch, similar to changing RPM across the diagonal, the collective pitch is changed in the same sense. The result is a fuselage torsional bending, like using RPM for yaw control. For a vehicle that uses differential cyclic for yaw control, pairs of rotors on the same side of the vehicle apply cyclic control in one direction while the pair of rotors on the opposing side of the vehicle apply cyclic control in the opposite sense. Different from a conventional multirotor, application of yaw control creates in-plane bending of the fuselage.

The actuators used have a maximum speed of .067s/60 degrees, shown in table 4.19, from [49]. Model aircraft servo actuator specifications are generally given as a time to rotate through 60 degrees. Of course, when there is a load on the actuator, the speed will decrease. For cyclic control, the maximum deflection of the servo arm is approximately 30 degrees, so using the maximum speed is a reasonable upper boundary for cyclic control. Assuming small inputs, this maximum speed is approximately 15-18 hertz, depending on the voltage, which corresponds well with the predicted natural frequency of the fuselage in-plane bending mode. The flight controller output is adjustable from 50-200 hertz which would suggest that lag in the flight controller was not a factor.

Table 4.19: Servo Specifications

Model	***Speed***	***Torque***
Spektrum H3050	0.067 sec/60° at 4.8V	29 oz-in at 4.8V
	0.053 sec/60° at 6.0V	36 oz-in at 6.0V

Incidentally, during the flight test where this damage occurred, the vehicle control gains were being tuned, in flight, specifically the yaw gain. During most flight tests, the rotors could be seen oscillating slightly fore and aft. This would suggest that a poorly tuned yaw gain would initiate oscillations in the the rotors which would initiate fuselage in-plane bending. As the fuselage began bending, this could create a situation where the system vibrates near the natural frequency of this mode.

Mode excitation through actuator input has been observed in quadrotor vehicles with fixed-pitch rotors. A fixed-pitch rotor vehicle creates yaw moments through differential thrust by increasing the RPM in two of the rotors and decreasing RPM in the other pair. As mentioned previously, rotors located on the frame diagonal, with respect to the longitudinal axis, spin in the same direction, while rotors located on the opposite side of the frame, with respect to the frame longitudinal axis, spin in opposite directions. In general, the quadrotor vehicle would not be sensitive to the direction of rotation of a pair of rotors, however, if the frame is torsionally flexible, the chosen direction can increase the possibility for the torsional frame mode being excited by actuator inputs. Because pairs of rotors on the diagonal increase thrust with the other pair decrease thrust, this creates a torsional moment in the frame about the longitudinal axis. When the frame flexes, this will tilt the lift vector of the rotors and create a yawing moment. If this is counter to the desired yaw direction, the rotors will increase RPM further to compensate. Sharp yaw inputs can set up a situation where the frame torsionally flexes and resonates about the longitudinal axis, leading the loss of control. A quadrotor that used differential collective pitch for yaw control would potentially encounter a similar scenario if the torsional resonant frequency of the frame is within the actuator bandwidth.

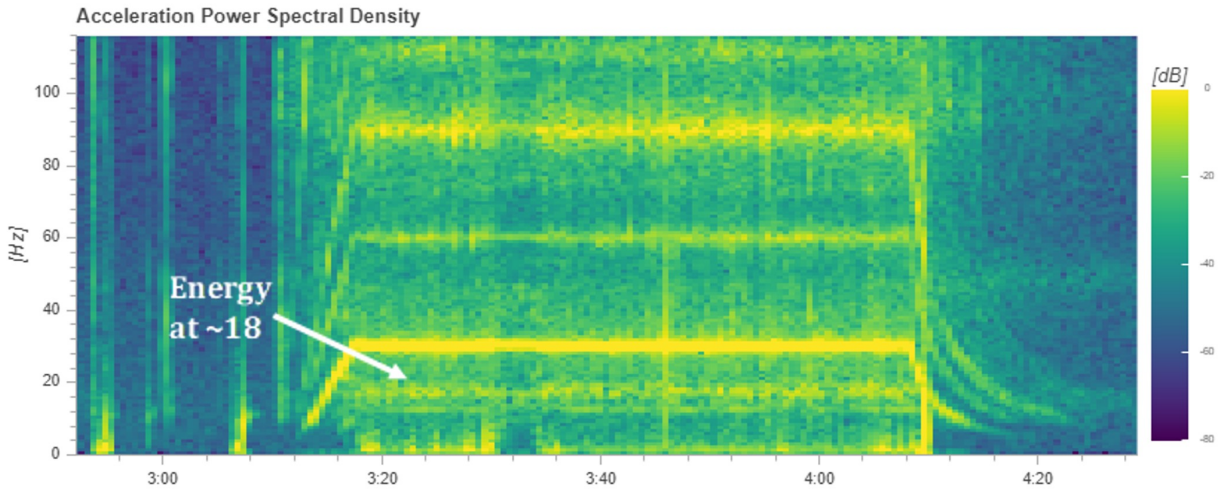

Figure 4.17: Acceleration Power Spectral Density Plot Showing Vibration Energy at Low Frequencies

Table 4.20: RPM, Throttle %, & Vibration Characteristics

Throttle % (Estimated)	$< 45\%$	45%–60%	60%–75%	$> 75\%$
RPM	< 1575	$1575 - 2100$	$2275 - 2675$	> 2675
ω ***Hz***	< 26	$26 - 35$	35–45	> 45
Observed Vibrations	High	Acceptable	High	Not tested

For the current frame configuration, the lowest airframe harmonic is the fuselage torsional mode at a predicted frequency at approximately 15 hertz from the FEA model, shown in figs. 3.20 & table 3.4 and approximately 11 hertz from the physics model, seen in 4.12. If the vehicle were to use differential collective pitch for yaw control or some combination of differential cyclic and collective control for yaw, a poorly tuned yaw gain could instigate the low frequency fuselage torsional mode. Initially this mode was thought to be well out of range of being excited by the main rotors, however, this mode appears to still be at risk, specifically if differential collective pitch is used for control. The direction of rotation of the rotors is also significant with this mode if differential collective pitch or varying RPM is used for control. The torsional moment created about the fuselage longitudinal axis depends on the direction of rotation of the rotors which affects the torsional bending of the fuselage and the structural stability. Due to the diagonal arrangement, the torsional moment about the fuselage longitudinal axis creates and angular displacement. If this displacement is in a direction that decreases the yaw moment, due to the tilting of the thrust vector, the flight controller will attempt to further increase collective pitch or RPM. The fuselage stiffness acts like a spring and can create a situation of structural instability in the airframe. A poor choice of flight controller gains for the yaw access can instigate fuselage vibrations. This should be carefully considered when developing control allocation arrangements.

4.4.5 State-space representation

For initial vibration analysis, the mass-spring-damper model was written out explicitly for each mode. This was important to develop the model however, this model lacks fidelity and versatility. The model is still decoupled into airframe arm and the fuselage bending and torsion modes. Paz & Leigh [50] provide guidance for developing a structural model in this form. This compact formulation of the structural model allows a natural integration of the aerodynamic stability derivatives for stiffness and damping. Additionally, this simplifies the consideration of derivatives that couple the vibration modes. The initial analysis only considered the fundamental damping derivatives for each mode such as the damping derivatives, X_u, Z_w, and M_q for in-plane, out-of-plane, and torsional vibrations, respectively. The state-space model was broken down into a structural spring matrix, a structural damping matrix, and the aerodynamic longitudinal flight dynamics stability matrix. The latter provides aerodynamic stiffness and damping contributions. For a given rotor, a separate analysis can provide the longitudinal flight dynamics matrix or this can be obtained from flight test data.

$$A_{aero} = \begin{bmatrix} 0 & 0 & 0 & 0 & 0 & 0 \\ 0 & 0 & 0 & 0 & 0 & 0 \\ 0 & 0 & X_u & X_w & X_q & X_\theta \\ 0 & 0 & Z_u & Z_w & Z_q & Z_\theta \\ 0 & 0 & M_u & M_w & M_q & M_\theta \\ 0 & 0 & 0 & 0 & 1 & 0 \end{bmatrix} \begin{bmatrix} \Delta x \\ \Delta z \\ \Delta u \\ \Delta w \\ \Delta q \\ \Delta \theta \end{bmatrix} \tag{4.35}$$

$$K_{structural} = \begin{bmatrix} 0 & 0 & 1 & 0 & 0 & 0 \\ 0 & 0 & 0 & 1 & 0 & 0 \\ \frac{3EI}{L_1^3} & 0 & 0 & 0 & 0 & 0 \\ 0 & \frac{3EI}{L_2^3} & 0 & 0 & 0 & 0 \\ 0 & 0 & 0 & 0 & 0 & \frac{GJ}{L_3} \\ 0 & 0 & 0 & 0 & 0 & 0 \end{bmatrix} \begin{bmatrix} \Delta x \\ \Delta z \\ \Delta u \\ \Delta w \\ \Delta q \\ \Delta \theta \end{bmatrix} \tag{4.36}$$

$$C_{structural} = \begin{bmatrix} 0 & 0 & 0 & 0 & 0 & 0 \\ 0 & 0 & 0 & 0 & 0 & 0 \\ 0 & 0 & c1 & 0 & 0 & 0 \\ 0 & 0 & 0 & c2 & 0 & 0 \\ 0 & 0 & 0 & 0 & c3 & 0 \\ 0 & 0 & 0 & 0 & 0 & 0 \end{bmatrix} \begin{bmatrix} \Delta x \\ \Delta z \\ \Delta u \\ \Delta w \\ \Delta q \\ \Delta \theta \end{bmatrix} \tag{4.37}$$

$$[M]\,\ddot{\mathbf{x}} + [C]\,\dot{\mathbf{x}} + [K]\,\mathbf{x} = f\,(t) \tag{4.38}$$

$$\ddot{\mathbf{x}} + \frac{[C]}{[M]}\dot{\mathbf{x}} + \frac{[K]}{[M]}\mathbf{x} = f\,(t) \tag{4.39}$$

$$\dot{\mathbf{x}} = [A_{aug}]\,\mathbf{x} + [B]\,\mathbf{u} \tag{4.40}$$

$$\mathbf{x} = \begin{bmatrix} \Delta x \\ \Delta z \\ \Delta u \\ \Delta w \\ \Delta q \\ \Delta \theta \end{bmatrix} \tag{4.41}$$

$$\begin{aligned} A_{aug} &= A_{aero} + K_{struct} + C_{struct} \\ &= \begin{bmatrix} 0 & 0 & 1 & 0 & 0 & 0 \\ 0 & 0 & 0 & 1 & 0 & 0 \\ \frac{3EI}{L_1^3} & 0 & X_u + c1 & X_w & X_q & X_\theta \\ 0 & \frac{3EI}{L_2^3} & Z_u & Z_w + c2 & Z_q & Z_\theta \\ 0 & 0 & M_u & M_w & M_q + c3 & M_\theta + \frac{GJ}{L_3} \\ 0 & 0 & 0 & 0 & 1 & 0 \end{bmatrix} \end{aligned} \tag{4.42}$$

$$B\mathbf{u} = \begin{bmatrix} 0 & 0 \\ 0 & 0 \\ X_{\theta_0} & X_{\theta_{1s}} \\ Z_{\theta_0} & Z_{\theta_{1s}} \\ M_{\theta_0} & M_{\theta_{1s}} \\ 0 & 0 \end{bmatrix} \begin{bmatrix} \theta_0 \\ \theta_{1s} \end{bmatrix} \tag{4.43}$$

An augmented matrix is created by summing the contributions from each of the matrices. This aero-structural augmented matrix, A_{aug}, represents the open-loop response of the sys-

tem. The effect of passive and active vibration attenuation will be explored in the next section.

4.4.6 Effect of Cross-Coupling Derivatives

For the vibrating airframe, the main aerodynamic contributions are the damping derivatives X_u, Z_w, and M_q. These damping derivatives act on the same axis as the motion of the rotor, i.e. in-plane force due to in-plane motion and torsional moment due to pitch rate about the axis of rotation. The cross-coupling derivatives M_u and X_q couple a motion in one direction with a force in another. For the initial analysis, the cross-coupling derivatives were not included. To determine the effect of this simplification, the frequency and damping of the modes are compared with and without the cross-coupling derivatives for the rotors on the vehicle. Table 4.21 shows the effect of the cross-coupling on the system. For the current

Table 4.21: Effect of Including Cross-Coupling Derivatives (Blade 360 CFX Trio)

Blade 360 CFX Trio	*Without M_u and X_q*		*Including M_u and X_q*	
Mode	***Frequency***	***Damping Ratio***	***Frequency***	***Damping Ratio***
Arm In-Plane	36.1 Hz	7.85e-5	36.1 Hz	7.99e-5
Arm Out-of-Plane	21.8 Hz	4.95e-3	21.8 Hz	4.95e-3
Arm Torsion	44.9 Hz	6.86e-3	44.9 Hz	6.86e-3

system, the effect of the cross-coupling derivatives is fairly muted. Upon further analysis, it was discovered that due to the structure of the matrices, only M_u affects the system; X_q does not provide an effect.To explore the effect of including the other cross-coupling derivatives in the system, the full longitudinal aerodynamic matrix for the BO-105C was used to explore the movement of the poles when the entire set of cross-coupling derivatives is included. For the BO-105 rotor, there was no pronounced effect by including the full set of derivatives

Table 4.22: Effect of Including Cross-Coupling Derivatives (BO-105C)

BO-105	*Without M_u and X_q*		*Including M_u and X_q*	
Mode	***Frequency***	***Damping Ratio***	***Frequency***	***Damping Ratio***
Arm In-Plane	36.1 Hz	3.65e-5	36.1 Hz	3.65e-5
Arm Out-of-Plane	21.8 Hz	1.21e-3	21.8 Hz	1.21e-3
Arm Torsion	44.9 Hz	6.03e-3	44.9 Hz	6.03e-3

including the cross-coupling derivatives. This suggests that simplifying the model with the main damping derivatives does not detrimentally degrade the model. It should be noted that this may not hold true for different combinations of derivatives and structural arrangements. It is recommended to include the full set of derivatives when convenient.

4.5 Vibration Attenuation

The natural frame response may require modifications to the natural frequencies if the natural frequencies were close to the operating frequencies of the vehicle. This would be especially true if the vehicle we to operate at multiple RPM for performance considerations. Adding more structural members or larger structural members to increase the natural frequencies can negatively impact performance of the vehicle and may, at times, amplify how vibrations are transmitted to the flight controller. Some vibrations may be attenuated by changing the mounting of the rotor units to the frame, however, large amplitude, low frequency vibrations, at frequencies near the natural frequencies of the frame can still set up a resonance situation. Starting with an existing frame, two feasible options to attenuate these vibrations or modify the frame response are through passive and active methods.

4.5.1 Passive Vibration Attenuation

A passive method of vibration attenuation may consist of some spring and damper element combination, in line with one or more of the frame structural members, to modify the natural response of the frame. These passive elements can be designed to change the response near known 'problem' frequencies. One major design consideration for this method is the weight of the installed elements. A passive spring-damper element can be significantly heavier than additional structural members. The spring-damper element would be placed in the position of an existing structural member and the existing structural member would need to be modified or eliminated to allow compliance in the structure to activate the elements. The choice of the structural member in which to integrate the spring-damper element should be an element that would develop, for example, tensile or compressive loads, in response to the dominant motion of the frame harmonic which is being designed to.

Section 4.4.3 presented two modes that were significantly underdamped, when compared with the other damped modes. These modes were responsible for the two instances of major structural damage to the frame. The in-plane bending of the arms lead to the first frame failure and the in-plane bending of the fuselage led to the second frame failure. The arm in-plane bending mode was eliminated by extending the strut brace, outboard, to the rotor mechanics. This eliminated the cantilevered outboard portion of the arm and effectively eliminated in-plane bending of the arm. The fuselage in-plane bending mode was eliminated by adding lateral struts between the arms. FEA analysis shows a possible anti-symmetric, in-plane bending mode of the fuselage with the lateral struts, however, this was outside of the operational range of the rotors and bandwidth of the servo actuators. Figure 4.18 shows a proposed location for a spring-damper element to modify the in-plane bending response of the fuselage. Adding the spring-damper element in place of or in line with the member will allow activation if the fuselage bends in plane. Additionally, this spring-damper element would modify the response of the arms bending in-plane for anti-symmetric modes; the arms

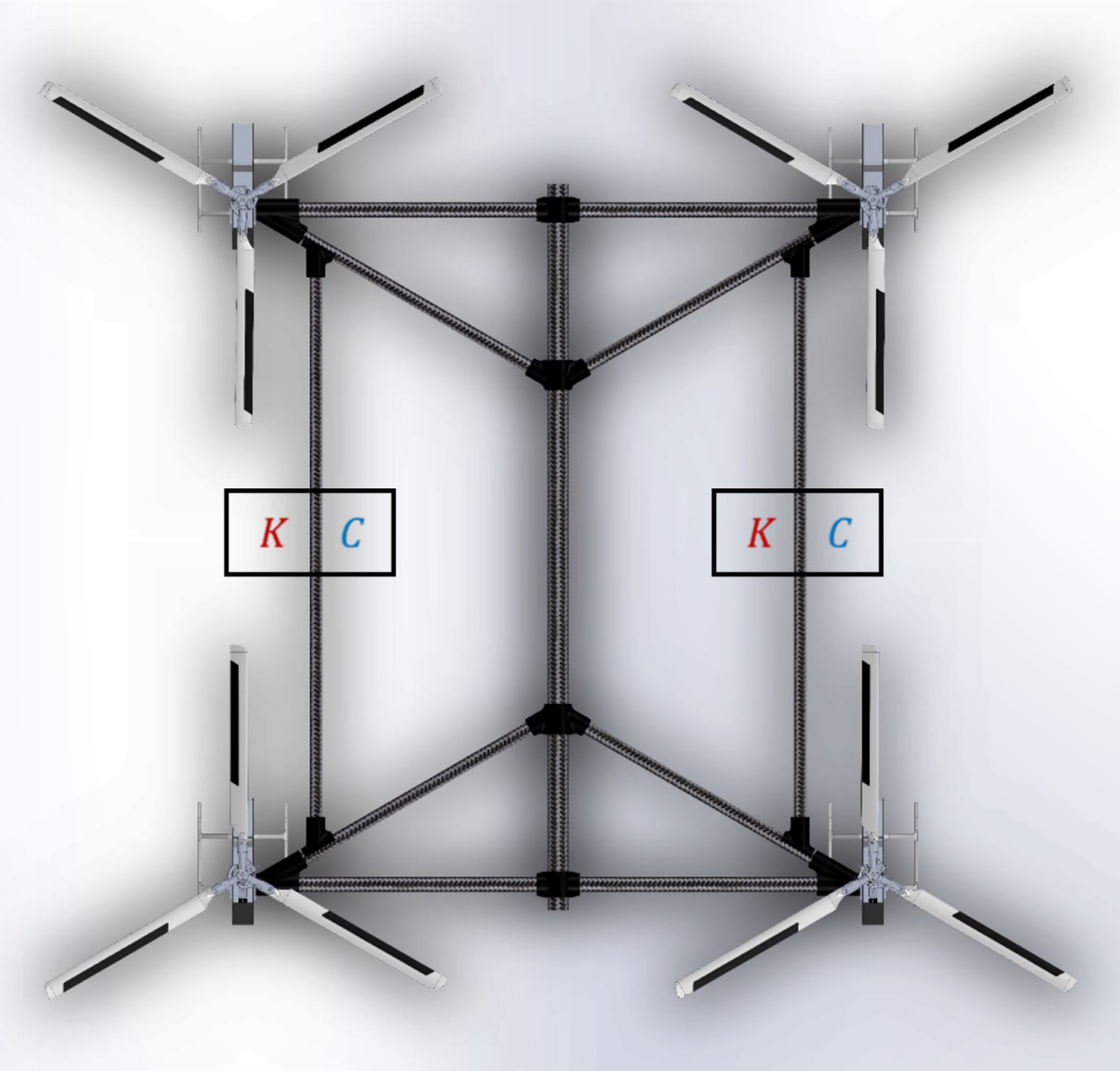

Figure 4.18: Frame with Proposed Locations for Spring & Damper Elements

opposing each other. If the rotors vibrate fore and aft, together symmetrically, this addition would not be effective. A proposed location for the spring-damper element specifically to modify the arms bending in plane would be in line with the arm strut brace. If the cross-section of the main structure member were not uniform, these elements would provide a means to tune the frame response while providing stiffness in the vertical direction. Because the frame structure already provides significant stiffness to the system, the damping element is the most important addition. A spring can be used to tune the frequency, however, the

spring would need to be on the order of the stiffness of the structural member it is interacting with. The damping element provides the means to absorb energy being passed through the frame. For preliminary analysis and sizing of the elements, the matrices were formed into a simple state-space feedback system.

$$\dot{X} = [A_{aug}]\, X + [B_{SD}]\, [k_{SD}]\, [C]\, X + [B_{SD}]u \tag{4.44}$$

$$k_{SD_{arm}} = -\frac{1}{M_{eqiv,arm}} \begin{bmatrix} k_{k_x} & k_{k_z} & k_{c_u} & k_{c_w} & k_{c_q} & k_{k_\theta} \end{bmatrix} \tag{4.45}$$

$$B_{SD_{arm}} = \begin{bmatrix} 1 \\ 1 \\ 1 \\ 1 \\ 1 \\ 1 \end{bmatrix} \tag{4.46}$$

The gain matrix, shown in eq. 4.45, for the frame arm, is initially set to be zero and the gain values will be determined based on the stiffness and damping requirements. The B_{SD} matrix is specific to the spring-damper element and is not the same matrix as the control derivatives. Initial values for the B_{SD} matrix are set to be 1 so that the initial gain values represent the physical required value of the spring or damping element. The value of the elements in the $[B]$ matrix could be interpreted as the number of spring or damper elements allocated for each mode and represent the activation of each element based on the geometry. For example, if the element is at an angle to the direction of the motion of the airframe component, the

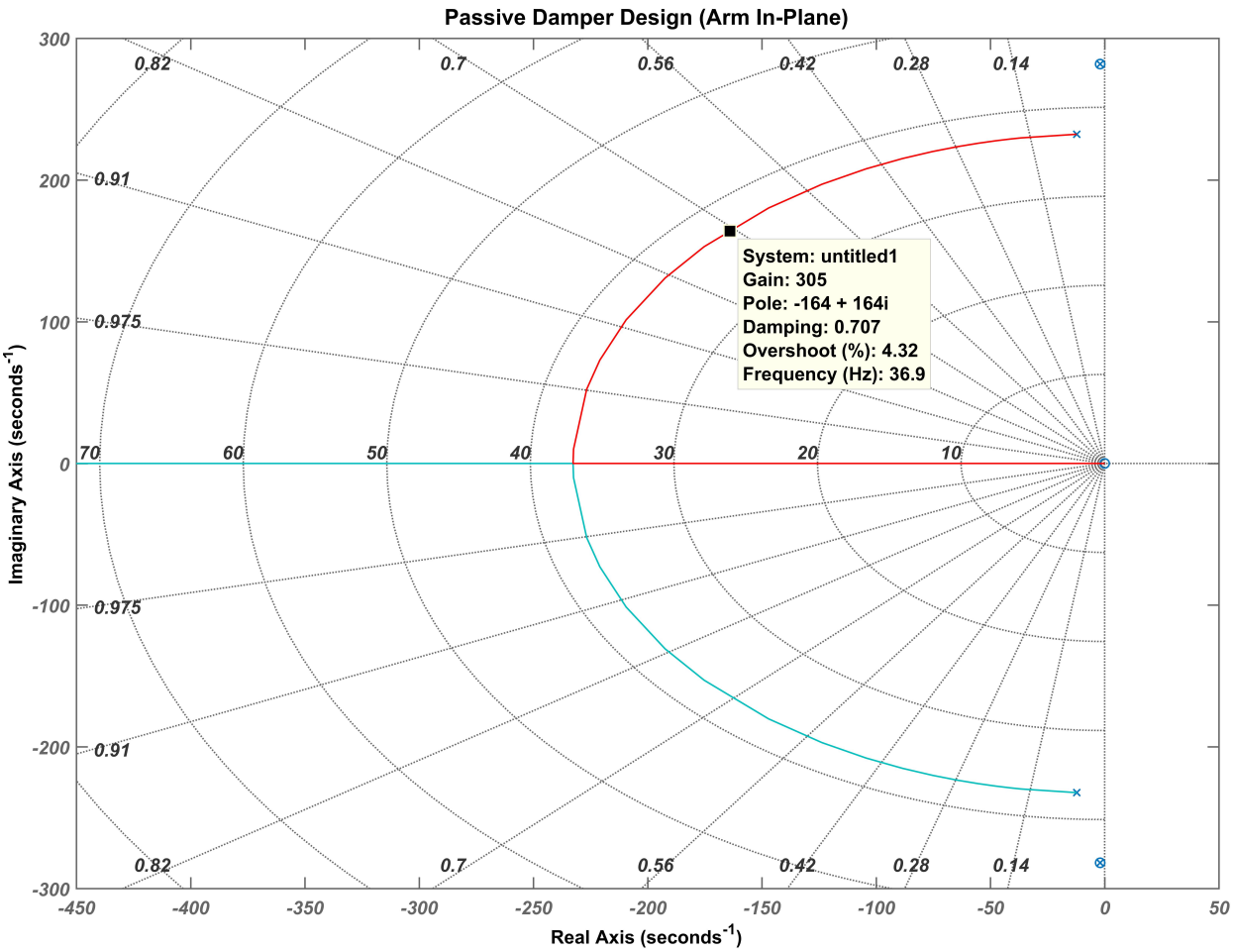

Figure 4.19: Root Locus for Passive Damper Design (Arm In-Plane)

activation would be less than 1 for that motion and the $[B]$ matrix would incorporate this factor. The inputs, $\overrightarrow{u}$ are set to zero initially to determine the values for the spring and dampers. If the spring or damping elements have active control, such as a mechanism to modify spring or damping constants as a function of the flight condition, then the control input matrix would not be zero. The MATLAB root locus tool aides in determining the gain values based on desired criteria. In this case, the gain value will represent the required spring and damping constants to achieve the prescribed response. Figure 4.19 shows an example of the root locus for the damper design for the in-plane motion of the frame arms. The initial calculated damping constants may require spring-damper elements that are not available on a scale that is consistent with this vehicle. Although not explored at this time,

a classic passive solution is the implementation of tuned masses. This type of vibration attenuation is commonly implemented on conventional helicopters. For a vehicle of this size and scale, rotor head additions such as bifilar absorbers, 'flexspring' absorbers, and pendulum absorbers may be impractical or infeasible, however, tuned masses on the fuselage may be feasible, with the main propulsion batteries being likely candidates. For more details regarding passive vibration absorbers in rotorcraft, the readers are directed to Bramwell [51] and Prouty [40, 38, 47].

4.5.2 Active Vibration Attenuation

Due to the unique control configuration of this multirotor vehicle, the vehicle is over actuated. The current control allocation scheme is described in table 2.3. This allows the ability to develop specific control schemes to minimize a given cost function and allocate control power for auxiliary functions such as vibration attenuation. Similar to using feedback control to modify the response of a free-flying aircraft, feedback control can be used to modify vibration response of the airframe by modifying the aerodynamic stiffness and damping of one or more of the individual rotor systems. Equation 4.47 describes the control law for the system. For the control derivative matrix, the vehicle was assumed to be in hover and only direct inputs to each axis were considered. Changes in cyclic input were assumed to not cause a vertical force and similarly, collective inputs were assumed to not cause in plane forces or moments; $X_{\theta_0} = M_{\theta_0} = Z_{\theta_{1s}} = 0$.

$$\dot{X} = [A_{aug}]\, X + [B]\, [k]\, [C]\, X + [B] u \tag{4.47}$$

This would be similar to higher harmonic control, which has been studied for conventional rotorcraft, but instead of using individual blade motion for vibration attenuation in the rotor units, each rotor unit would use its dynamics to attenuate vibration in the complete vehicle.

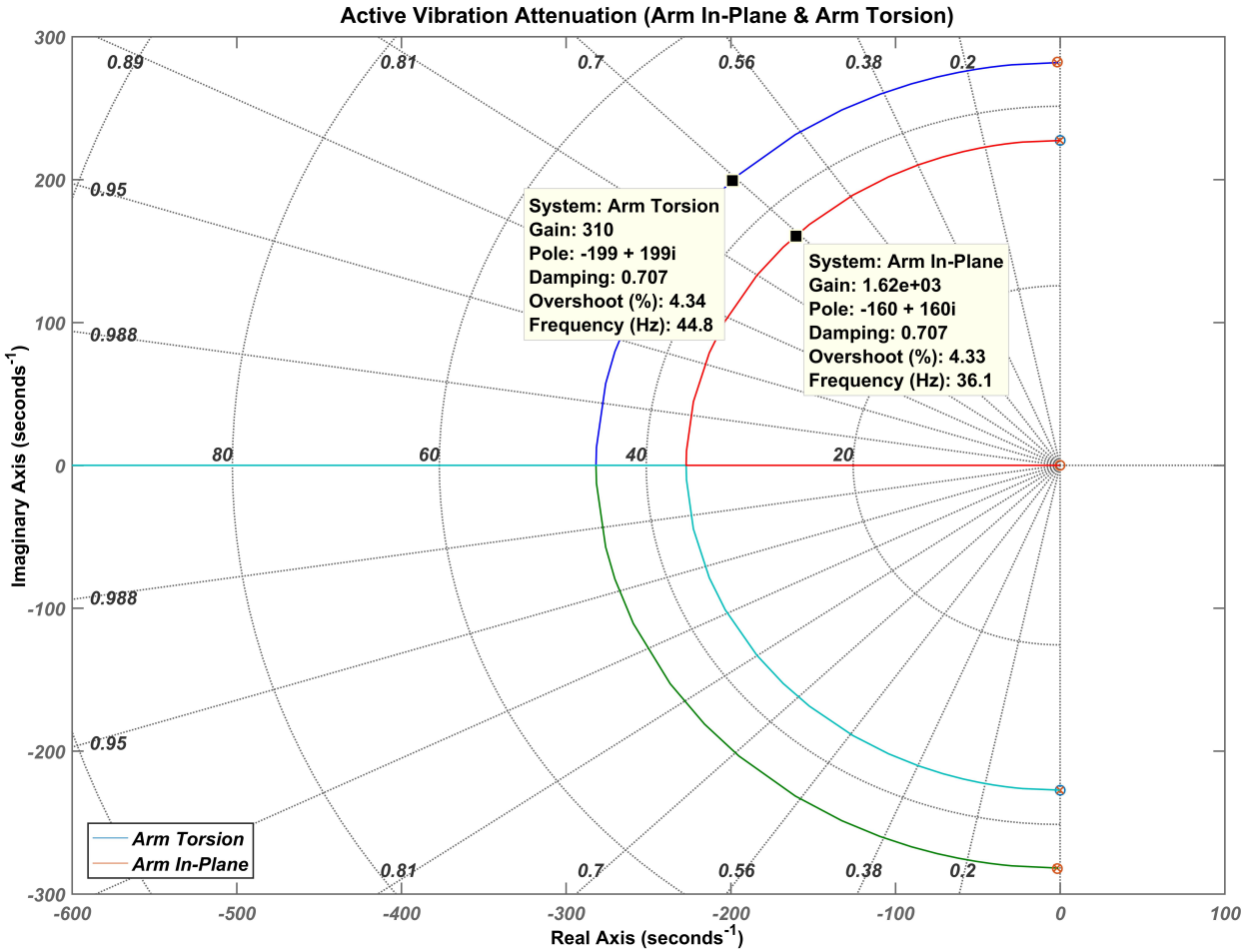

Figure 4.20: Root Locus for Active Vibration Attenuation (Arm In-Plane & Arm Torsion)

As Bramwell and Prouty describe, higher harmonic control (HCC), is an active vibration attenuation method in which individual blades are pitched at various positions during the rotation. For a conventional swashplate, an input from the fixed frame to the swashplate will result in sinusoidal pitching motion of a given blade per cycle. For higher harmonic control, high-frequency actuators, allow motion of the swashplate at various points in the cycle to pitch the blades and modify the aerodynamic loads of the blades. Individual blade control (IBC) is a high harmonic control method where individual actuators are installed, in the rotating frame, to pitch individual blades at any point during the cycle. These actuators are often placed in line between the pitch-links and the swashplate or, in some cases, in place of a swashplate entirely. A design constraint of such as system requires the actuators to operate

at high frequency, on the order of the rotor RPM, and have a large operating bandwidth. For a vehicle of this scale, it may be infeasible to find or manufacture miniature actuators that and operate at in excess of 40 hertz. The additional control power requirements would also provide constraints on the system.

For this current test vehicle, the idea of higher harmonic control is reimagined to instead use the entire rotor to modify the vibration response of the fuselage. While frequency requirements still provide limitations, because the actuators would remain in the non-rotating frame, there are more choices of actuators. While traditional higher harmonic control schemes could be used to modify vibrations from transient blade loads, the current proposed method is to apply cyclic and collective pitch, at each rotor unit, to modify the response in the airframe. This would be realized as changes to the aerodynamic damping of the rotors as well as the application of the forces out of phase from the frame harmonic vibration motion. In a traditional helicopter, oscillating the cyclic and collective pitch would not provide direct control of the vibration response in the fuselage, however, because the multirotor frame is more like a large 'tuning fork', there exists the opportunity to apply forcing that is phased to suppress frame vibrations. Additionally, the over-actuated configuration allows the possibility to modulate the RPM, while still balancing forces and moments to reduce vibrations near sensitive frequencies. This scheme could be implemented in the flight controller or using an auxiliary micro controller. Sensors on the airframe would measure accelerations and vibrations of specific components and depending on the mode shape and frequency, the vibration data would be translated into an input that would be added with the commanded input from the pilot or flight controller to output blade pitch. The result would be high-frequency os-

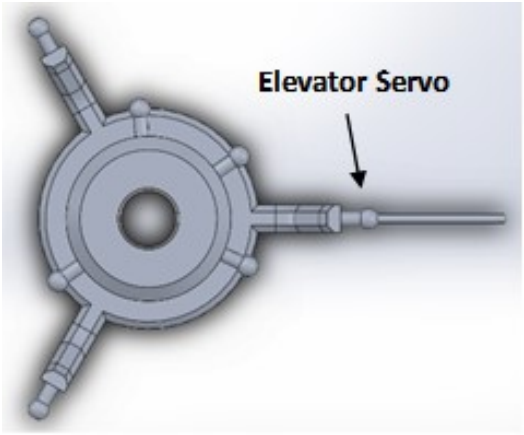

Figure 4.21: Arm Out-of-Plane Bending with Fuselage Motion

cillations of blade pitch overlayed on the lower-frequency pilot commands. There is another interesting implementation. The dominant vibration modes are the arms vibrating in plane, the arms vibrating in torsion, the fuselage vibrating in plane, and the fuselage vibrating in torsion. Three of these four modes can be controlled through fore and aft cyclic pitch. One of the most common swashplate configurations is 120° CCPM (Cyclic-Collective Pitch Mixing). In this configuration, to control elevator input, two servo actuators provide an input in one direction while the other single servo applies an input in the opposite direction. A common model aircraft gyro sensor used for helicopter tail rotor control accepts the pilots commanded input and then modifies the output based on the yaw motion of the helicopter. This only controls one servo actuator at a time. Installing a gyro sensor or accelerometer in line with the elevator servo could sense the motion of the rotor at the end of the frame arm and apply an input to just the elevator servo. Applying a small amplitude, high frequency elevator command could modify the vibration response and either change the resonant frequency or attenuate the vibration. Applying only an elevator input, while holding the position of the other swashplate actuators stationary will cause a change in collective pitch as well, in 120° CCPM configuration. However, with a high frequency, low amplitude application of the elevator servo input for vibration modifications, this would be unlikely to cause a significant change in altitude due to the lag nature of thrust changes to change in altitude. Figure 4.21 shows the location of the elevator servo and a typical swashplate with 120° CCPM arrangement.

A better solution would be to use one gyro sensor for each servo with two operating the in the same direction and the other operating in the opposite direction. As mentioned before, even though this would only be able to control fore and aft cyclic, this would be able to modify the vibration response for the in-plane motion of the arms and fuselage, as well as the torsional response of the fuselage arms. To modify the out-of-plane motion of the arms and torsional motion of the fuselage, separate sensors would be needed. The analysis of the aero-structural interaction showed that the out-of-plane arm and fuselage bending modes were less likely

to be excited during operation. If this control is desired, the best implementation would be to have a central computer and fuselage accelerometers that would feed a command to the flight computer.

A potential limitation to use of active vibration attenuation is the bandwidth requirement of the actuators. The servo actuators need to be able to operate in the range of a few hertz (pilot inputs) to at least the upper bound of the RPM range to cover most problem frequencies. If actuator bandwidth cannot extend to the upper limits of the operational RPM, this higher harmonic control can still attenuate low frequency vibrations while RPM modulation and passive vibration absorption can be used to address frequencies out of range.

A variation of the active vibration attenuation method is to employ a semi-active vibration attenuation method. In this method, actuators would be incorporated into spring & damping elements to adjust the physical geometry of the elements, changing the spring & damping constants. As the vehicle operating conditions change, the elements can be modulated to modify the response of the airframe. This can also be accomplished with a brushless DC motor attached to a transmission. Using a motor controller, the motor can be modulated to change the rate at which energy is dissipated. This is already used in model aircraft for wheel brakes. The benefit of semi-active vibration attenuation is potential easing of actuator bandwidth requirements. It is unlikely that the elements would need to be modulated at the same rate as a true active vibration attenuation method because the elements would change based on operating conditions as opposed to a direct response to airframe motions. The method may be able to blend together the benefits of an active method that can adapt to a wider range of operating conditions with some of the simplicity of a passive method and a reduction of actuator requirements.

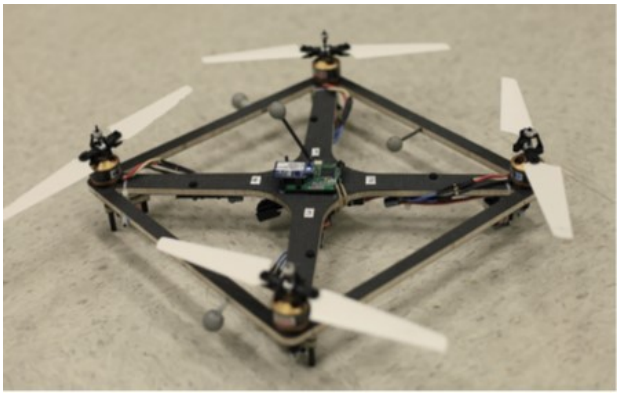

(a) Frame Design from Cutler [52]

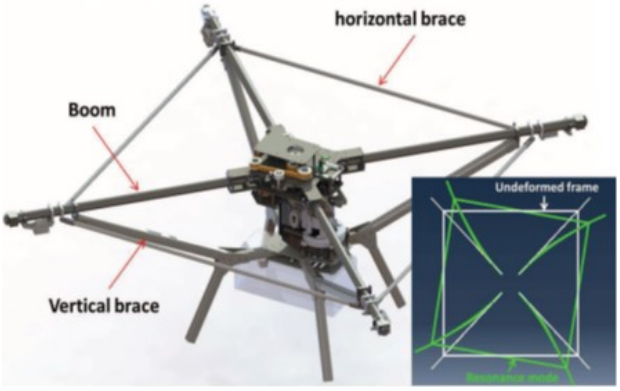

(b) Frame design from Pang et. al [3]

(c) Frame design from Wu [21]

Figure 4.22: Example Frames Showing Similar Fuselage Bracing

4.5.3 Additional Considerations

An interesting point should be noted. Each iteration of the frame seemed to be converging on a single shape. Regardless if the initial configuration starts with an X-shape or an H-shape, as the frame is modified to combat structural vibrations, a similar geometry is realized. The X-shape frame would need lateral and longitudinal struts to stabilize the arms. The H-shape frame needs longitudinal struts and cross-braces to stabilize the arms. The aircraft from Cutler et. al [52], Pang et. al [3], and Wu [21], Fig. 4.22a, Fig. 4.22b, & Fig. 4.22c, respectively, show a similar trend. The frame from Cutler is a square with cross-braces. The author states, "[t]he square shape is designed to minimize vibrations induced by the propellers, motors, and servos because the vibrations cause the attitude estimate by the on-

board sensors to quickly deteriorate." [52]. It should also be noted that, Cutler appears to have had an early version of the frame that that was more like a convention X-shape frame [53]. The author discusses that the cross-braces were added for vibration considerations. Cutler also notes that other attempts at variable-pitch configurations experienced significant vibration problems. The frame from Pang et. al shows structural considerations for the vibration problems discussed in their work. The H-shape frame from Wu does not appear to have to have lateral struts but does have the arms strut-braced to the landing gear. Similar to Pang et. al, Wu discussed significant vibration problems during flight.

Chapter 5

Vehicle Stability & Control Allocation

5.1 Vehicle Stability & Control Derivatives

Extending the stability and control derivatives presented in Chapter 4, a set of stability and control derivatives were derived for the complete vehicle. In Chapter 4, the derivatives were focused on a single rotor and only the longitudinal derivatives were considered as this was sufficient to characterize the vibrations of the arms and the fuselage. Due to the high degree of symmetry of the rotor, most of the lateral-directional derivatives have the same derivation and similar values to the longitudinal derivatives, except for appropriate sign changes. $Y_v = X_u$, $Y_p = -X_q$, $L_p = M_q$, and $L_v = -M_u$. If the longitudinal and lateral inertia, I_{yy} & I_{xx}, differ significantly, the derivative values will change by the ratio of the inertia values. The values differ due to the differences of moment of inertia on each axis. Only derivatives due to the rotor are considered and effects from the frame are neglected. Additionally, the directional derivatives due to yaw rate are significantly different, when compared to most conventional helicopters because the tail rotor and fuselage provide significant contributions on this axis. For the rotor alone, there is no yaw contribution due to yaw rate. When

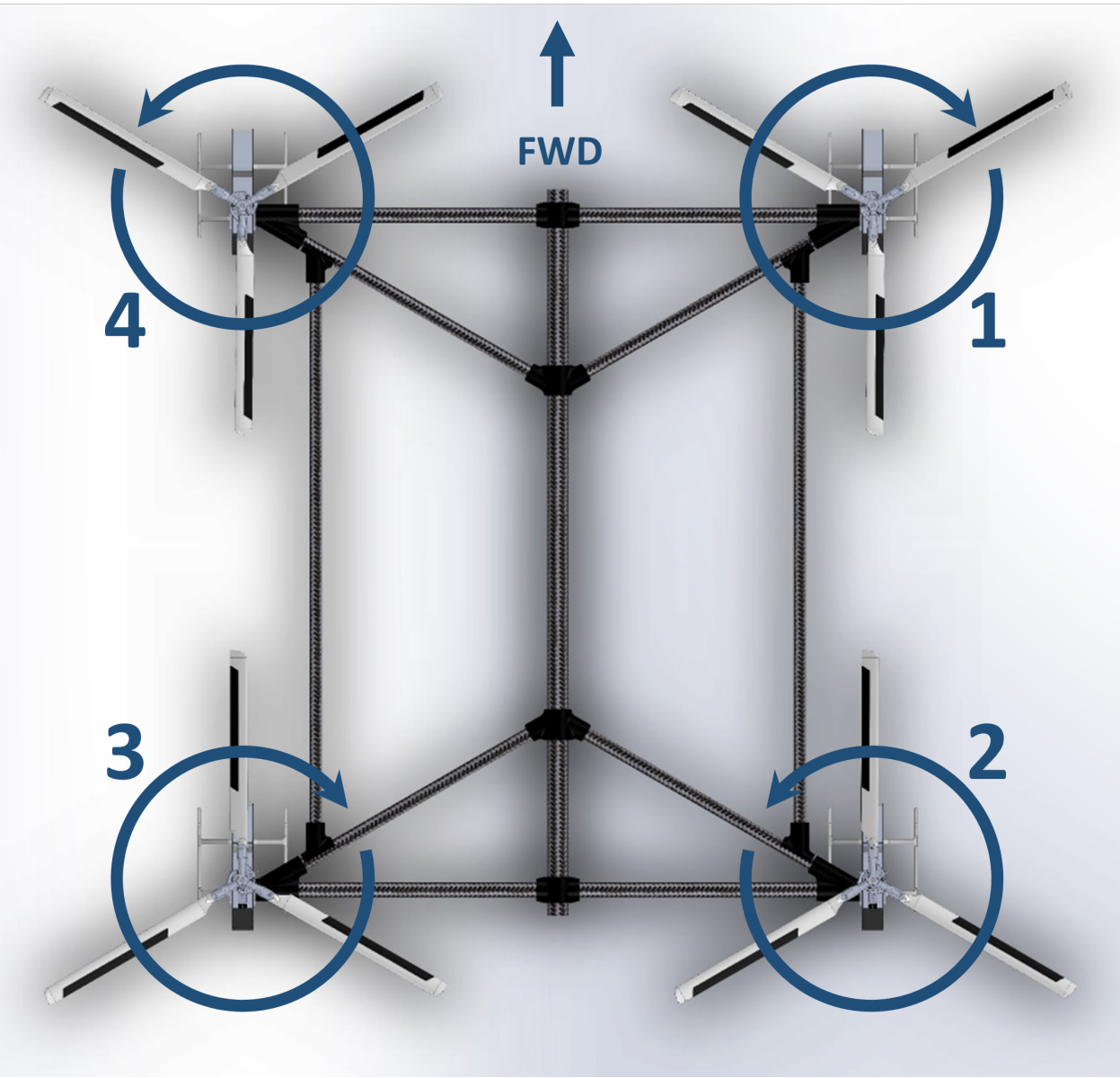

Figure 5.1: Rotor Layout and Rotation Direction

extended to the entire vehicle, the in-plane forces provide a contribution. The vehicle is only analyzed in hover for the current research, however future work should include stability and control at forward speed.

To compute the derivatives for the complete vehicle, the derivatives are first computed for the single rotor using the estimated moments of inertia, mass, and predicted thrust for the rotor unit only. When extended to the complete vehicle, the derivatives are first multiplied

by the single rotor mass and moments of inertia, then normalized by the mass and moments of inertia for the complete vehicle as shown eqs. 5.2 & 5.3. The force derivatives for the complete vehicle are the summation of the contributions of each rotor. The roll and pitch moment derivatives for the complete vehicle are the sum of the combination of each rotor plus the sum the heaving contribution of each rotor at is respective distance from the center of gravity, on each axis. The heaving derivative provides a major contribution to the pitch and roll damping derivatives. This is analogous to the tandem rotor configuration except this occurs on both axes as opposed to the single pitch or roll axis for the longitudinal tandem or lateral tandem configuration, respectively. The yaw moment derivative, N_r, shown in eq. 5.1, is the sum of the contribution of each rotor in-plane force derivatives, X_u, at the diagonal distance from the center of gravity (C.G.), $l = \sqrt{(l_y/2)^2 + (l_x/2)^2}$.

$$N_r = \sum_{i=1}^{N} \frac{1}{I^*_{zz}} (l^2 X_u)_i \tag{5.1}$$

Table 5.1: Vehicle Stability Derivatives

Longitudinal Derivatives		*Lateral-Directional Derivatives*	
Stability Derivative	***Value***	***Stability Derivative***	***Value***
X_θ	-g	Y_ϕ	g
X_u	-0.0343	Y_v	-0.0343
X_q	0.1916	Y_p	-0.1916
M_q	-3.7371	L_p	-5.6473
M_u	0.0997	L_v	-0.1587
Z_w	-1.3569	N_r	-0.0553
$M_{\Delta w}$	-1.1360	-	-

$$X_{u,_{Vehicle}} = \sum_{i=1}^{N} \frac{1}{M^*_{Vehicle}} M^*_{Rotor,i} X_{u,_{Rotor,i}} \tag{5.2}$$

$$M_{u,_{Vehicle}} = \sum_{i=1}^{N} \frac{1}{I^*_{yy,_{Vehicle}}} I^*_{yy,_{Rotor,i}} M_{u,_{Rotor,i}} \tag{5.3}$$

The reason for this convolution is to keep the stability and control derivatives general for a single rotor for ease of comparison with published data for other rotorcraft. Unfortunately, the published data for the stability and control derivatives of multirotor vehicles is sparse. This has created some difficulties in validating the extension to the complete vehicle. Comparing the directional derivatives of the vehicle to that of a tandem-rotor configuration, from Franklin [43], can help provide a basis for validation. The analysis of the stability and control derivatives from Chapter 4 is still valid in this section, for a single rotor. A brief comparison is presented to included additional contributions such as yaw rate stability and control derivatives. Additionally, the values for the complete vehicle are compared with data from Niemiec & Gandhi [54] where stability and control of a fixed-pitch multirotor is considered. Comparing the predictions with the published data, shown in table 5.2, some of the stability derivatives have good agreement while others have poor agreement. This is due, in part, to the geometry, size, and operating conditions of the vehicles, but may also be due to poor predictions and simplified models. The prediction of M_q has good correlation with Niemiec & Gandhi [54] while the correlation with Franklin [43] is poor. The heaving derivative plays a large role in the pitch and roll damping of a tandem and multirotor configuration. The heave derivative has a similar value between the current study and the quadrotor from Neimiec & Gandhi, while there is a large deviation from the CH-47B. The effect would be a reduction in pitch damping due to rotor heaving. The quadrotor from Niemiec & Gandhi is assumed to have the same longitudinal and lateral moment of inertia so there is symmetry between the pitch and roll derivatives. The current vehicle does not have the same longitudinal and

Table 5.2: Vehicle Stability Derivatives Comparison

Vehicle Stability Derivatives			
Stability Derivative	***Prediction***	***Quadrotor from [54]***	***CH-47B from [43]***
$X_u \quad [sec^-1]$	-0.0343	-0.0413	-0.021
$X_q \quad [ft/sec/rad]$	0.1916	-	2.59
$M_q \quad [sec^-1]$	-3.7371	-3.9454	-1.23
$M_u \quad [rad/ft-sec]$	0.0997	2.6228	0.0093
$Z_w \quad [sec^-1]$	-1.3569	1.1813	-0.3
$M_{\Delta w} \quad [rad/ft-sec]$	-1.1360	-	0.0023
$Y_v \quad [sec^-1]$	-0.0343	-0.0413	-0.14
$Y_p \quad [ft/sec/rad]$	-0.1916	-	-1.49
$L_p \quad [sec^-1]$	-5.6473	-3.9454	-0.72
$L_v \quad [rad/ft-sec]$	-0.1587	-2.6228	-0.0065
$L_{\Delta w} \quad [rad/ft-sec]$	-1.7131	-	-
$N_r \quad [sec^-1]$	-0.0553	-0.1557	-0.047

lateral moment of inertia which affects the symmetry of the values. The yaw damping on all three vehicles is due to the in-plane derivative, X_u at a distance from the C.G. It is not clear why there is a large discrepancy between the prediction and Niemiec & Gandhi. There were some other questions regarding values from Niemiec & Gandhi such as the value for M_u, which is orders of magnitude higher than what is typically found in most rotorcraft. The authors also included a value for M_θ (not shown) which, in this case, is not a control derivative, but rather a stability derivative, representing a restoring moment due to changes in pitch angle. They do not provide a basis for calculation of the value, however, this value is typically zero (or very small) for most helicopters and aircraft. The thrust line going through the C.G. provides no moment with pitch angle. If this were the case, a hovering helicopter would maintain level attitude, and with the pitch and roll damping, it would be quite stable. This, however, is not typical of a helicopter, which requires constant pilot inputs to hover

and maintain attitude. Regardless of this, there is some correlation and validation of the predicted values for the current configuration.

Similar to the stability derivatives, the contributions of each rotor are summed together to obtain each control derivative for the complete vehicle. To preserve the various methods of control, a separate control derivative matrix is developed for each control allocation method. Two implementations of the control derivatives are used depending on the context. In the context of control of the vehicle from the pilot's perspective, the control derivatives also include the transfer function of pilot's control input to blade angle or swashplate angle output, like that shown in fig. 4.1. From the pilot's perspective, there are four main controls: fore/aft cyclic, lateral cyclic, collective pitch, and rudder control. For a conventional rotorcraft, the main rotor RPM is typically maintained in a narrow range, by an engine governor, and not typically considered a pilot control. The control derivative summation accounts for this and the control derivative matrix is formed so the control input vector are these four controls. In the context of the control allocation study, the control derivatives are no longer taken from the pilot's perspective but rather in terms of each control input directly at the rotor blades or swashplate. The four main controls are then: fore/aft cyclic, lateral cyclic, collective pitch, and RPM control. These derivatives do not include the transfer function from the pilot's controls to the swashplate, however, they are multiplied by the maximum value of each control, i.e. blade angle or RPM to normalize the values for the control allocation study. This is discussed in more detail in a later section.

For cyclic pitch control, a method of altitude control must be employed by either incorporating collective pitch or RPM control, however, these controls are only used for vertical control and the forces and moments about the other axes are the summation of the forces and moments developed by the rotors much like a conventional helicopter. The only exception is the directional stability and control derivatives which come from the rotor contributions of

X_u and X_θ with a moment arm equal to the longitudinal or lateral distance from the C.G, $l_y/2$ or $l_x/2$, respectively.

For collective pitch control of forces and moments about the center of gravity, the force derivative Z_θ is applied at each rotor and the moments about the respective axes come from the longitudinal or lateral distance from the C.G. The yaw moment control derivative arises from the changes in torque of the rotors due to changes in blade angle. The main contribution to the changes in torque come from tilting of the lift vector due to the change in the blade angle. While changes in section drag due to change in angle of attack would contribute to this, the section drag is assumed constant for this current study. Equation 5.5 shows the derivation for the dimensional value of the yaw moment due to blade angle for a single rotor from Johnson [37]. Extending this to the vehicle, the rotor contributions are summed together and normalized by the vehicle inertia, with the method shown in eq. 5.3.

Table 5.3: Rotor Control Derivatives

Control Derivative	***Value***
Z_{θ_0} $[ft/sec^2/in]$	-8.3323
Z_Ω $[ft/sec^2/(rad/sec)]$	-0.3657
X_{θ_s} $[ft/sec^2/in]$	0.5891
M_{θ_s} $[rad/sec^2/in]$	-6.2566
Y_{θ_c} $[ft/sec^2/in]$	0.5891
L_{θ_c} $[rad/sec^2/in]$	7.3515
N_{θ_0} $[rad/sec^2/in]$	4.7257
N_Ω $[rad/sec^2/(rad/sec)]$	0.2448

$$N_{\theta_0} = \sum_{i=1}^{N} \frac{1}{I_{zz}} \frac{\partial Q}{\partial \theta_{0\,i}} \tag{5.4}$$

$$N_{\theta_{0_{rotor}}} = \left(\frac{1}{6}\right) \frac{2\gamma\sqrt{C_T/2}}{I^*_{zz_{rotor}}} \Omega^2 \tag{5.5}$$

For RPM control of forces and moments about the center of gravity, the force derivative Z_Ω is applied at each rotor and the moments about the respective axes come from the longitudinal

or lateral distance from the C.G., similar to collective pitch control. The derivation of the dimensional derivative for Z_Ω is shown in eq. 5.7. The yaw moment control derivative arises from the changes in torque of the rotors due to changes in RPM. For the rotor, $P = Q\ \Omega$ and when normalized, $C_Q = C_P$, as discussed by Johnson [37]. The changes in torque due to changes in RPM come from the increase drag of the blade due to increased dynamic pressure and due to tilting of the lift vector from changes in angle of attack. Equation 5.9 shows the derivation for the dimensional value of the yaw moment due to RPM for a single rotor. Extending this to the vehicle, the rotor contributions are summed together and normalized by the vehicle inertia, with the method shown in eq. 5.3.

$$Z_\Omega = \sum_{i=1}^{N} \frac{1}{M} \frac{\partial T}{\partial \Omega_i} \tag{5.6}$$

$$Z_{\Omega_{rotor}} = -\frac{2C_T\gamma}{\sigma a} \frac{1}{M^*_{rotor}} 2\Omega R \tag{5.7}$$

$$N_\Omega = \sum_{i=1}^{N} \frac{1}{I_{zz}} \frac{\partial Q}{\partial \Omega_i} \tag{5.8}$$

$$N_{\Omega_{rotor}} = \frac{2C_Q\gamma}{\sigma a} \frac{1}{I^*_{zz_{rotor}}} 2\Omega \tag{5.9}$$

The control derivative matrix shown in eq. 5.12 is from the pilot's perspective, as discussed previously. Once a control allocation scheme is developed, the complete vehicle control derivatives are estimated and the B matrix created. The four control inputs from the pilot are fore/aft cyclic, lateral cyclic, vertical control, and rudder. The control matrix does not

provide information on the specific implementation as the pilot does not consider this when flying, but rather cares about the how the vehicle responds. For example, when the pilot modulates the collective lever, the blade angles may change, the RPM may change, or both, but the pilot will only respond to the acceleration and rate of the vehicle.

$$\dot{\mathbf{x}} = [A]\,\mathbf{x} + [B]\,\mathbf{u} \tag{5.10}$$

$$A = \begin{bmatrix} X_u & 0 & X_q & -g & X_v & X_p & 0 & 0 \\ 0 & Z_w & 0 & 0 & 0 & 0 & 0 & 0 \\ M_u & M_{\Delta w} & M_q & 0 & M_v & M_p & 0 & 0 \\ 0 & 0 & 1 & 0 & 0 & 0 & 0 & 0 \\ Y_u & 0 & Y_q & 0 & Y_v & Y_p & g & 0 \\ L_u & L_{\Delta w} & L_q & 0 & L_v & L_p & 0 & 0 \\ 0 & 0 & 0 & 0 & 0 & 1 & 0 & 0 \\ 0 & 0 & 0 & 0 & N_v & N_p & 0 & N_r \end{bmatrix} \begin{bmatrix} \Delta u \\ \Delta w \\ \Delta q \\ \Delta \theta \\ \Delta v \\ \Delta p \\ \Delta \phi \\ \Delta r \end{bmatrix} \tag{5.11}$$

$$B = \begin{bmatrix} 0 & X_{\theta_s} & 0 & 0 \\ Z_{\theta_0} & 0 & 0 & 0 \\ 0 & M_{\theta_s} & 0 & 0 \\ 0 & 0 & 0 & 0 \\ 0 & 0 & Y_{\theta_c} & 0 \\ 0 & 0 & L_{\theta_c} & 0 \\ 0 & 0 & 0 & 0 \\ 0 & 0 & 0 & N_{\theta_p} \end{bmatrix} \begin{bmatrix} \delta_0 \\ \delta_s \\ \delta_c \\ \delta_p \end{bmatrix} \tag{5.12}$$

The value of the control derivative that governs this motion will be determined by the allocation of the available controls, but the pilot's action will be the same for each implementation. Assessing the maximum movement of the cyclic stick, rudder pedals, and collective lever from an array of rotorcraft, there is consistency between vehicles. This makes sense because regardless of the vehicle size or configuration, the pilot will 'expect' the feel of the controls and the behavior of the vehicle to be similar. Table 5.4 shows the MATLAB code predictions

Table 5.4: Directional Rotor Control Derivatives Validation

Aircraft	***BO-105C***	***Puma SA330***	***Lynx ZD559***	***UH-1H***
(Hover, at SL)	N_{θ_0} $[rad/s^2/in]$	N_{θ_0} $[rad/s^2/in]$	N_{θ_0} $[rad/s^2/in]$	N_{θ_0} $[rad/s^2/in]$
NASA	0.5650	-	-	0.4364
Padfield[††]	19.7319	-12.1328	17.3054	-
Franklin	0.57	-	-	0.44
MATLAB	0.4573 (16.8462[††])	-12.7617[††]	16.9695[††]	0.2960

versus published data for the derivative, N_{θ_0}, discussed in this section. Unfortunately, there is no readily available data, from the presented sources, for yaw moment due to change in RPM, N_Ω, with RPM as a control. As this validation is a continuation of the validation presented in Chapter 4, the remaining lateral-directional derivatives are not shown because they have a similar derivation to their longitudinal counterparts and mainly differ by the moment of inertia. The validation of the longitudinal derivatives should be sufficient.

Tables 5.5, 5.6, and 5.7 show the control derivatives for the complete flight test vehicle. These are presented in terms of the different methods of control. The control derivatives are shown without the transfer function of the pilot's controls to the servo actuator or the servo actuator to blade pitch. Comparing collective control with RPM control, there is a fairly consistent ratio of 20. This suggests that a change of approximately $20rad/s(190RPM)$ is roughly equivalent to 1 degree change of collective pitch. This is around 11% of the maximum available (1680 RPM) available for control if the vehicle hovers at roughly 50% throttle. Comparing collective pitch control with cyclic pitch control, the ratio is 4-5.

This suggests that 4 degrees change in blade angle from cyclic pitch is equivalent to 1 degree change in collective pitch. With the maximum available blade pitch for control being approximately 14 degrees, this is roughly 30% of available cyclic pitch available. While this has not been experimentally verified, the approximations seem reasonable. Changes to airframe and rotorhead geometry would impact these ratios. This assessment does not include any information about control latency between the methods.

Table 5.5: Vehicle Control Derivatives - Cyclic Control

Longitudinal Derivatives		*Lateral-Directional Derivatives*	
Control Derivative	***Value***	***Control Derivative***	***Value***
$Z_{\theta_0} \quad [ft/sec^2/in]$	-8.3323	-	-
$X_{\theta_s} \quad [ft/sec^2/in]$	0.5891	$Y_{\theta_c} \quad [ft/sec^2/in]$	0.5891
$M_{\theta_s} \quad [rad/sec^2/in]$	-1.7996	$L_{\theta_c} \quad [rad/sec^2/in]$	2.8636
-	-	$N_{\theta_s} \quad [rad/sec^2/in]$	-0.4376

Table 5.6: Vehicle Control Derivatives - Collective Control

Longitudinal Derivatives		*Lateral-Directional Derivatives*	
Control Derivative	***Value***	***Control Derivative***	***Value***
$Z_{\theta_0} \quad [ft/sec^2/in]$	-8.3323	-	-
$X_{\theta_s} \quad [ft/sec^2/in]$	0	$Y_{\theta_c} \quad [ft/sec^2/in]$	0
$M_{\theta_s} \quad [rad/sec^2/in]$	-6.9761	$L_{\theta_c} \quad [rad/sec^2/in]$	10.5197
-	-	$N_{\theta_p} \quad [rad/sec^2/in]$	-0.9567

A brief comparison of the control derivatives is shown in tables 5.8 and 5.9. The quadrotor from Niemiec & Gandhi uses RPM control only. Additionally, their data only provides a numerical value for M_Ω, however, if this value has good correlation, this should validate Z_Ω as well. The CH-47B uses collective pitch for generating pitching moments, M_{θ_0}, and vertical forces, while using cyclic pitch for lateral moments, L_{θ_c}, and yaw moments N_{θ_p}. Yaw

Table 5.7: Vehicle Control Derivatives - RPM Control

Longitudinal Derivatives		*Lateral-Directional Derivatives*	
Control Derivative	***Value***	***Control Derivative***	***Value***
Z_{θ_0} $[ft/sec^2/(rad/sec)]$	-0.3657	-	-
X_{θ_s} $[ft/sec^2/(rad/sec)]$	0	Y_{θ_c} $[ft/sec^2/(rad/sec)]$	0
M_{θ_s} $[rad/sec^2/(rad/sec)]$	-0.3062	L_{θ_c} $[rad/sec^2/(rad/sec)]$	0.4617
-	-	N_{θ_p} $[rad/sec^2/(rad/sec)]$	-0.0496

moment due to collective pitch is nearly zero for the CH-47B because of the tandem configuration. Data from Franklin [43] and Padfield [42] is provided for additional comparison. Extrapolating between the various aircraft, there seems to be reasonable correlation with the current configuration, where applicable.

Table 5.8: Vehicle Control Derivatives Comparison (Set 1)

Control Derivatives			
Vehicle Control Derivative	***Prediction***	***Quadrotor [54]***	***CH-47B [43]***
Z_{θ_0} $[ft/sec^2/in]$	-8.3323	N/A	-8.06
Z_Ω $[ft/sec^2/(rad/sec)]$	-0.3657	-	N/A
X_{θ_s} $[ft/sec^2/in]$	0.5891	N/A	0.114
M_{θ_s} $[rad/sec^2/in]$	-1.7996	N/A	See M_{θ_0}
M_{θ_0} $[rad/sec^2/in]$	-6.9761	N/A	0.33
M_Ω $[rad/sec^2/(rad/sec)]$	-0.3062	0.42	N/A
$N_{\theta_{s/c}}$ $[rad/sec^2/in]$	-0.4376	N/A	0.2
N_{θ_0} $[rad/sec^2/in]$	-0.9567	N/A	-0.0004
N_Ω $[rad/sec^2/(rad/sec)]$	-0.0496	-	N/A

[††]Padfield [42] does not provide linkage data for control input/output ratio. Ratio is set to 1:1 for the analysis. Additionally, the Padfield control derivatives do not have units per inch.

Table 5.9: Vehicle Control Derivatives Comparison (Set 2)

Control Derivatives			
Control Derivative	***Prediction***	***BO-105 [7]***	***Lynx [42]***
Z_{θ_0} $[ft/sec^2/in]$	-8.3323	-9.8810	-93.9179 $[m/sec^2 rad]$
Z_Ω $[ft/sec^2/(rad/sec)]$	-0.3657	N/A	N/A
X_{θ_s} $[ft/sec^2/in]$	0.5891	N/A	-9.2860 $[m/sec^2 rad]$
M_{θ_s} $[rad/sec^2/in]$	-1.7996	-0.9727	26.4011 $[1/sec^2]$
M_{θ_0} $[rad/sec^2/in]$	-6.9761	N/A	N/A
M_Ω $[rad/sec^2/(rad/sec)]$	-0.3062	N/A	N/A
$N_{\theta_{s/c}}$ $[rad/sec^2/in]$	-0.4376	N/A	N/A
N_{θ_0} $[rad/sec^2/in]$	-0.9567	0.5651	17.3054 $[1/sec^2]$
N_Ω $[rad/sec^2/(rad/sec)]$	-0.0496	N/A	N/A

5.2 Hovering Flight Modes

The analysis of the vehicle in hover shows similar behavior when compared with a conventional rotorcraft. The vehicle has 4 first-order lag modes representing the pitch, roll, yaw, and vertical subsidence modes of the vehicle. The vehicle also has 2 oscillatory modes that are low frequency and slightly unstable. These modes represent a phugoid-like modes arising from a speed instability from the pitch and roll moment due to speed stability derivatives.

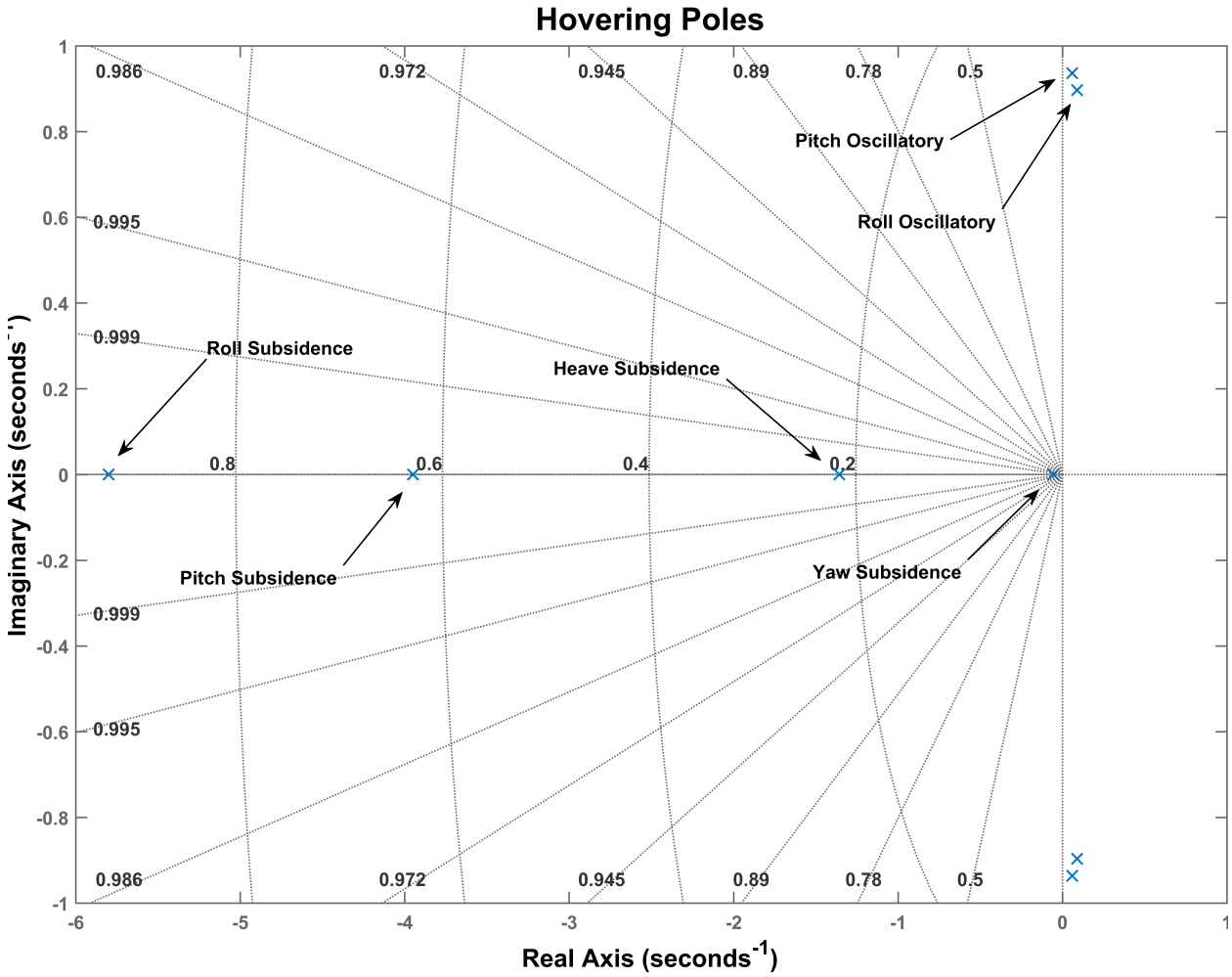

Figure 5.2: Hovering Flight Poles for the Complete Vehicle

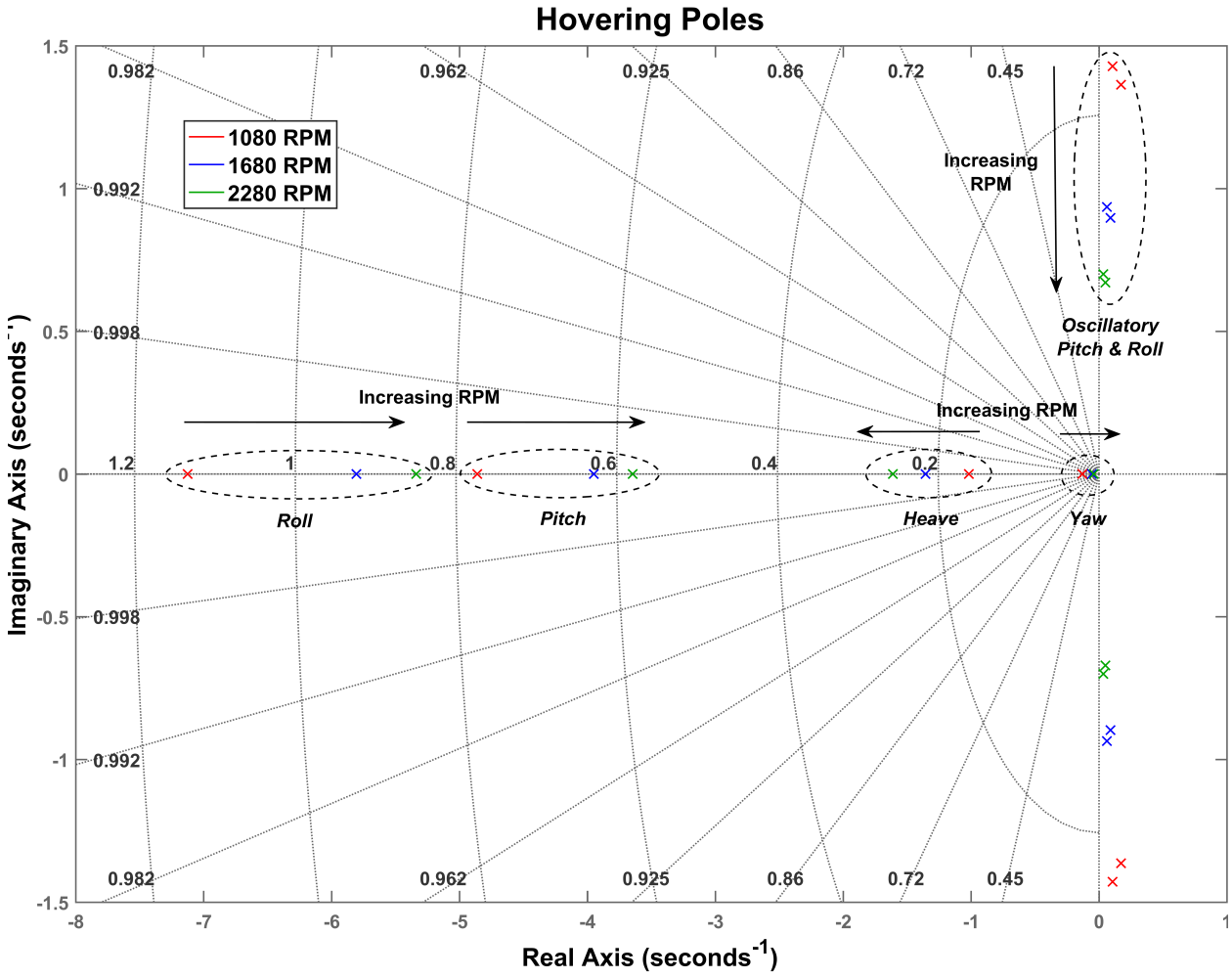

Figure 5.3: Root Locus for Hovering Flight Poles with Changes in RPM

The two unstable poles have a small, positive real component, shown in table 5.10. The predicted time-to-double for these modes is on the order of ~ 10 seconds. While pilot workload would be high, the vehicle could hover without feedback control. These oscillatory modes would not be the only source of high pilot workload. During hover, the 4 subsidence modes only have damping but there is no mechanism to bring the vehicle back to a trimmed position. Maintaining altitude, pitch & roll-attitude, and combating the low-frequency oscillations would be quite challenging. Incidentally, the vehicle has 'flown' in this configuration. The flight controller has different modes that can be selected from the pilot's controls. In the basic stabilized mode, the pilot control rates of the vehicle. This would be similar to flying

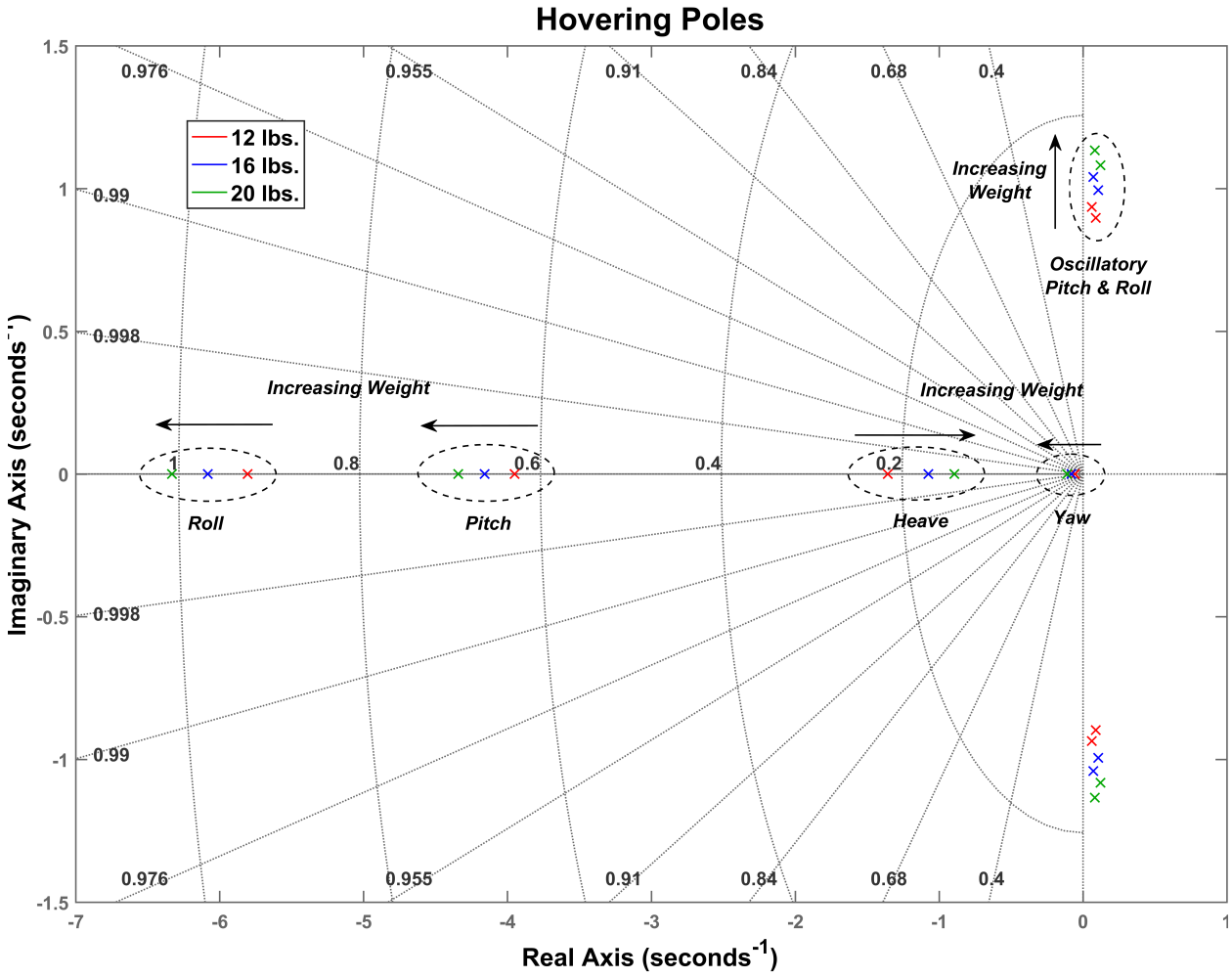

Figure 5.4: Root Locus for Hovering Flight Poles with Changes in Vehicle Weight

an aircraft with natural stability or flying a conventional model helicopter with a simple stability system. The another mode of flight is to control position, speed, and angle, instead of rates. This is generally preferred by novice pilots because it requires less skill/experience. The pilot's controls modulate speeds and the vehicle will generally maintain a stabilized, fixed position when the pilot controls are released. The flight controller also allows the vehicle to be flown open loop where the commands are essentially passed through the controller. Unfortunately, the pilot can takeoff in this mode if the toggle switch is bumped or mistakenly left in this position. On at least one occasion, this switch was left in the 'open-loop' configuration prior to takeoff. The vehicle was extremely difficult to control, but it was not

'impossible' to achieve a semi-stabilized hover. This was not tested extensively, but this would seem to be validated, in part, that the time to double was sufficiently large.

Table 5.10: Vehicle Poles & Time Constants/Time to Double

Mode	***Pole***	***Time Constant***	***Time to Double***
Roll Subsidence	$-5.80e{+}00$	$0.17s$	-
Pitch Subsidence	$-3.95e{+}00$	$0.25s$	-
Heave Subsidence	$-1.36e{+}00$	$0.74s$	-
Yaw Subsidence	$-5.53e{-}02$	$18.1s$	-
Pitch Oscillatory	$8.90e{-}02 \pm 8.97e{-}01i$	-	$7.8s$
Roll Oscillatory	$6.17e{-}02 \pm 9.36e{-}01i$	-	$11.2s$

5.3 Control Allocation

Compared with a conventional fixed-pitch multirotor, this configuration, with cyclic pitch, collective pitch, and RPM control, is significantly over-actuated. While an intuitive guess can establish a reasonable control allocation, it is not immediately clear if there is an 'optimal' method of control. An 'optimal' method would be judged based on specific cost functions that may change depending on the mission or flight condition. For example, the vehicle could be controlled by modulating RPM, however this may have higher control latency, and with fixed-pitch, the vehicle would not be able to achieve some flight attitudes, such as inverted flight. By adding collective pitch, control latency could be reduced and the vehicle could achieved sustained inverted flight. If maneuverability is a strict criterion, the cost function would likely eliminate fixed-pitch rotors with RPM control as a good candidate. If mechanical simplicity and robustness is a paramount requirement, then fixed-pitch rotors with RPM control would likely exceed collective pitch, although mechanical simplicity is more difficult to quantify and a simple cost function may not be able to be determined.

As discussed previously, by adding cyclic pitch, the vehicle flight envelope can be expanded for flight conditions such as autorotation, which would likely need cyclic pitch to maintain adequate yaw authority. During an autorotation, it would also be necessary to use collective pitch to control decent and rotor RPM. If autorotation was a necessary flight condition, this would eliminate a combination of controls that did not include collective pitch control. A specific cost function has not be developed a this time, however a comparison of the size of the reachable sets is presented as a first analysis of the benefit of adding an addition control method.

The control derivative matrix used for the control allocation study has a different arrangement. The complete control derivative matrix, eq. 5.13, is a concatenation of the control matrix contribution of each individual rotor, with size $8X4N_{rotor}$. The individual rotor control matrix, shown in eq. 5.14, considers all methods of control for each rotor; cyclic pitch, collective pitch, and RPM control. This does not account for the pilot's inputs but rather the inputs directly at the rotor. As described previously, when considering the individual rotors, moments are developed from changes in thrust by either collective pitch or RPM control. Taking the derivative M_{θ_0}, for example, from the pilot's perspective, application of collective pitch should not produce appreciable moments, however, from an individual rotor perspective, the change in thrust does produce a moment by the distance of the rotor from the C.G. The appropriate signs for each derivative is based on the rotor location, with the convention shown in fig. 5.1. The complete control matrix is parsed to include varying combinations of control allocations to assess the size of the reachable set utilizing each method. Equations 5.15-5.17 show the three basic combinations of these control inputs. For pure cyclic, it can be seen that there is no direct method to control altitude. A 'pure' cyclic method will need an additional control, either collective pitch or RPM, to control altitude. For both collective pitch control and RPM control, the longitudinal and lateral side-force derivatives are zero. Without tilting/inclination of the thrust line, variation of thrust can only generate moments, except in the vertical direction. The three base cases shown are combined to form the seven

control matrices for the control allocation study.

$$B_{vehicle} = \left[B_{rotor_1} \mid \; B_{rotor_2} \mid \; B_{rotor_3} \mid \; B_{rotor_4} \right] \tag{5.13}$$

$$B_{rotor} = \begin{bmatrix} X_{\theta_0} & X_{\theta_s} & X_{\theta_c} & X_{\Omega} \\ Z_{\theta_0} & Z_{\theta_s} & Z_{\theta_c} & Z_{\Omega} \\ M_{\theta_0} & M_{\theta_s} & M_{\theta_c} & M_{\Omega} \\ 0 & 0 & 0 & 0 \\ Y_{\theta_0} & Y_{\theta_s} & Y_{\theta_c} & Y_{\Omega} \\ L_{\theta_0} & L_{\theta_s} & L_{\theta_c} & L_{\Omega} \\ 0 & 0 & 0 & 0 \\ N_{\theta_0} & N_{\theta_s} & N_{\theta_c} & N_{\Omega} \end{bmatrix} \begin{bmatrix} \delta_0 \\ \delta_s \\ \delta_c \\ \delta_{\Omega} \end{bmatrix} \tag{5.14}$$

$$B_{cyclic} = \begin{bmatrix} 0 & X_{\theta_s} & X_{\theta_c} & 0 \\ 0 & 0 & 0 & 0 \\ 0 & M_{\theta_s} & M_{\theta_c} & 0 \\ 0 & 0 & 0 & 0 \\ 0 & Y_{\theta_s} & Y_{\theta_c} & 0 \\ 0 & L_{\theta_s} & L_{\theta_c} & 0 \\ 0 & 0 & 0 & 0 \\ 0 & N_{\theta_s} & N_{\theta_c} & 0 \end{bmatrix} \begin{bmatrix} 0 \\ \delta_s \\ \delta_c \\ 0 \end{bmatrix} \tag{5.15}$$

$$B_{collective} = \begin{bmatrix} 0 & 0 & 0 & 0 \\ Z_{\theta_0} & 0 & 0 & 0 \\ M_{\theta_0} & 0 & 0 & 0 \\ 0 & 0 & 0 & 0 \\ 0 & 0 & 0 & 0 \\ L_{\theta_0} & 0 & 0 & 0 \\ 0 & 0 & 0 & 0 \\ N_{\theta_0} & 0 & 0 & 0 \end{bmatrix} \begin{bmatrix} \delta_0 \\ 0 \\ 0 \\ 0 \end{bmatrix} \tag{5.16}$$

$$B_{RPM} = \begin{bmatrix} 0 & 0 & 0 & 0 \\ 0 & 0 & 0 & Z_\Omega \\ 0 & 0 & 0 & M_\Omega \\ 0 & 0 & 0 & 0 \\ 0 & 0 & 0 & 0 \\ 0 & 0 & 0 & L_\Omega \\ 0 & 0 & 0 & 0 \\ 0 & 0 & 0 & N_\Omega \end{bmatrix} \begin{bmatrix} 0 \\ 0 \\ 0 \\ \delta_\Omega \end{bmatrix} \tag{5.17}$$

Before comparing the control allocations together, it is necessary to normalize the derivatives by the maximum input available for each control input, at the rotor. This normalization is necessary because the control derivatives vary in magnitude depending on the control allocation. Comparing changes in force due to blade pitch and RPM, for example, a 1 degree change in blade angle could require an order(s) of magnitude different change in RPM to generate the same force. If the control input lies between $u(t) \in [u_{\min}, u_{\max}]$ with $u_{\max}$ being the maximum control input, i.e. maximum blade angle or maximum RPM, and

the trim value is u_0, we apply the transformation, $\tilde{u} = \frac{u-u_0}{u_{\max}-u_0}$. As such, $\tilde{u} <= 1$ and $\tilde{u} \in [0, 1]$. To obtain the normalized control derivative, the natural control derivative is multiplied by $u_{\max} - u_0$. The trim value, u_0 of each control input is estimated. For the blade angle, this value corresponds to a level swashplate at a position halfway up the mast. For the RPM control, this value corresponds to the the hovering RPM. It is common for multirotor vehicles to hover at 50% throttle to maintain sufficient overhead for control. The derivatives can then be more fairly compared with one another when assessing the maximum reachable set. The size of the reachable sets are quite sensitive to the estimated maximum control input value, $u_{\max} - u_0$ and constraints on maximum control input will affect the combination that achieves the largest reachable set. Further analysis should be performed to validate the estimated values. The maximum value, $u_{\max} - u_0$, beyond the trim value, for

Table 5.11: Maximum Value of Control Inputs

Control Input	***Maximum Input Value***, $u_{\max} - u_0$	***Maximum Input Value***, (at 12 lbs., 1680 RPM)
θ_0	$(18 - \theta_{trim})$ deg	12.6 deg
θ_s	7.5 deg	7.5 deg
θ_c	7.5 deg	7.5 deg
Ω	$(3540 - \Omega_{trim})$ RPM	1860 RPM

each control input is shown in table 5.11. The maximum values for collective pitch and cyclic pitch have been measure on the test flight vehicle. Full positive collective pitch is measured at approximately 18 degrees from flat pitch and maximum longitudinal or lateral cyclic is measured at approximately 7.5 degrees from flat pitch at the blade azimuthal location where the respective input is maximum. The maximum RPM is estimated based on the nominal input voltage of the battery, the motor Kv, and the gearing. The hovering collective pitch, θ_{trim}, is governed by eq. 5.18 from Johnson[37].

$$\theta_{.75} = \frac{(1 + \frac{3}{2}\mu^2)(\frac{6C_T}{\sigma a} + \frac{3}{8}\mu^2\theta_{tw}) + \frac{3}{2}\lambda_{TPP}(1 - \frac{1}{2}\mu^2)}{1 - \mu^2 + \frac{9}{4}\mu^4} \tag{5.18}$$

To compare different control allocations, we compare the size of the reachable set of the vehicle associated with each control allocation strategy, as a metric. Following Humbert & Faruque [55], the controllability gramian can be used to provide a measure of the volume of the reachable set of the vehicle. This, in turn, can provide insight into necessary control effort. As described by Humbert & Faruque, by choosing actuator combinations that maximize the size of the reachable set, this combination has the possibility to minimize control effort and possibly reduce the number of actuators. Humbert & Faruque formulate the problem by starting with the controllability operator $x_0 = \Psi_C u$, where Ψ_C maps control input history $u(t)$ to the final state x_0. The mapping of $\Psi_C u$ can be represented as a set in an N-dimensional space, where N is the number of states. The controllability gramian, X_C, can provide an estimate of the size of this set in the N-dimensional space, representing the reachable set. The controllability gramian is defined as

$$X_C = \Psi_c {\Psi_c}^* = \int_0^\infty e^{A\tau} B B^* e^{A^*\tau} d\tau \geq 0 \tag{5.19}$$

and can be computed by solving the Lyapunov equation

$$A X_C + X_C A^* + B B^* = 0 \tag{5.20}$$

The eigenvectors of $X_C^{1/2}$ are the principle axes of an ellipsoid in the N-dimensional space and the eigenvalues represent length along each principal axis. Moving along one of the principle axes describes how large the states could be or essentially how 'far' the vehicle could move with a unit input of control energy. Maximizing the principle axes can lead to minimizing the control power of the vehicle and the number of actuators. Computing the determinant of the controllability gramian matrix characterizes the volume, and therefore the size of the reachable set. The Frobenius norm of $X_C^{1/2}$ is also used to characterize the size of the reachable set.

The A-matrix is invariant to the choice of control scheme for this configuration, however, 7 variations of B-matrix are compared for the study of reachable sets. These variations are derived from the 3 main control allocation strategies: cyclic pitch, collective pitch, and RPM control. Table 5.12 shows the control allocations for each configuration.

Table 5.12: Control Input Configurations

Control Configuration	***Cyclic***	***Collective***	***RPM***
Cyclic Only	**X**	-	-
Collective Only	-	**X**	-
RPM Only	-	-	**X**
Cyclic & RPM	**X**	-	**X**
Collective & RPM	-	**X**	**X**
Cyclic & Collective	**X**	**X**	-
Cyclic, Collective, & RPM	**X**	**X**	**X**

The first control allocation with only cyclic pitch is used a method of validation in the comparison. With only cyclic pitch, there is no method to control altitude. This is expected to have a very small reachable set, which can be seen in the results. This provides some confirmation of the method.

Figures 5.5 & 5.6 show the values of the determinant of $X_C^{1/2}$ and the first Forbenius norm of $X_C^{1/2}$, respectively. These are computed at hovering conditions at approximately 1680 RPM. Analysis of the results show consistent trends using both criteria. Interestingly, there is a pronounced increase in the reachable set from the addition of collective pitch. While cyclic pitch alone does not provide a controllable vehicle, RPM alone does. This is the method employed by most conventional multirotor vehicles. The combination of RPM and cyclic pitch enhances the reachable set from cyclic alone as the vertical direction is now controllable, however, the increase from RPM control alone is minimal. The introduction

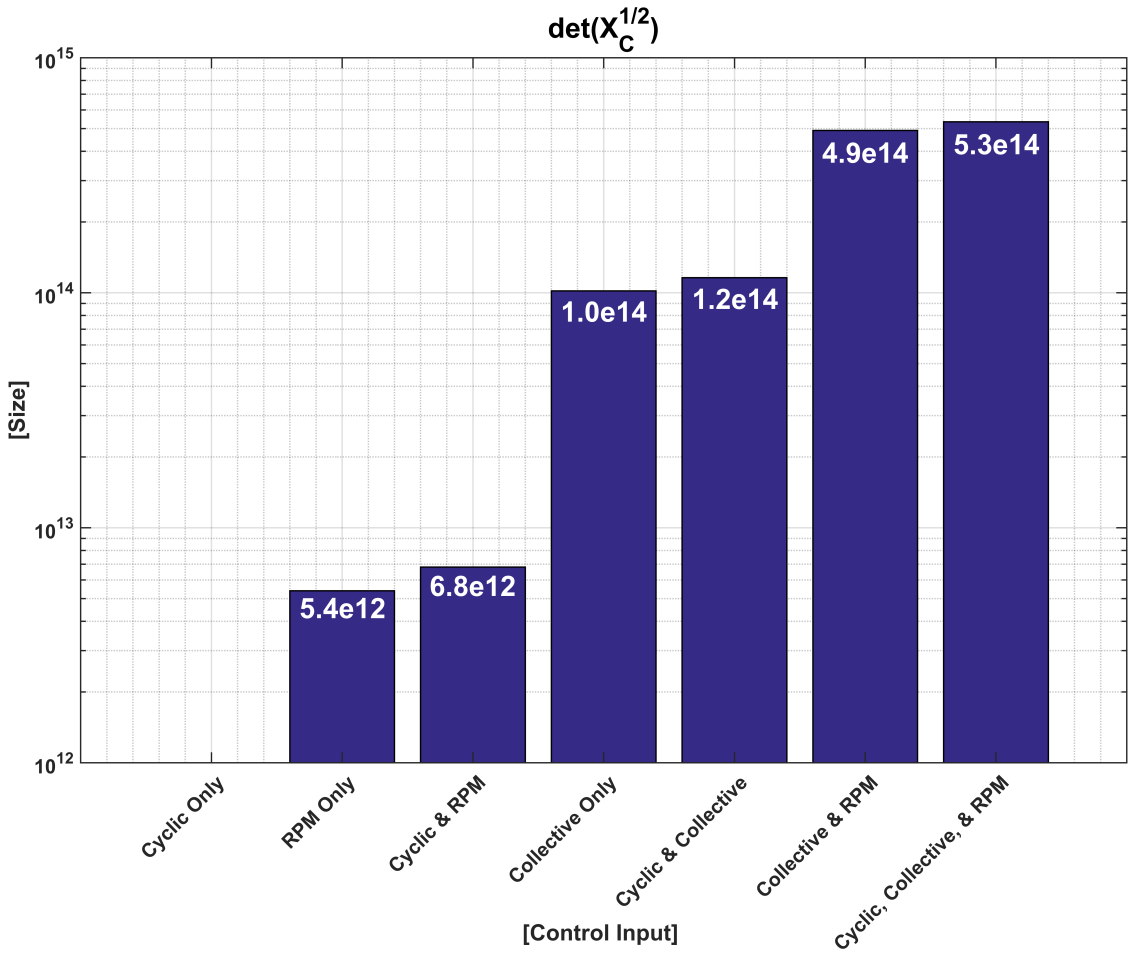

Figure 5.5: Comparison of $det(X_C^{1/2})$ Values for Each Control Allocation (at 12 lbs., 1680 RPM)

of collective pitch further increases the size of the first Frobenius norm when compared with RPM control alone. The addition of collective pitch control to RPM control provided a major improvement over RPM control alone, however, adding RPM control to collective pitch control provides a smaller benefit over collective pitch control alone. Three combinations with collective pitch control were considered: collective pitch alone, collective pitch with cyclic pitch, and collective pitch with RPM control. Of the three combinations, the combination of collective pitch with RPM control has a pronounced benefit over collective pitch alone or collective & cyclic pitch. The combination of collective pitch plus cyclic pitch control is the current control allocation employed on the test vehicle. Finally, the combination of

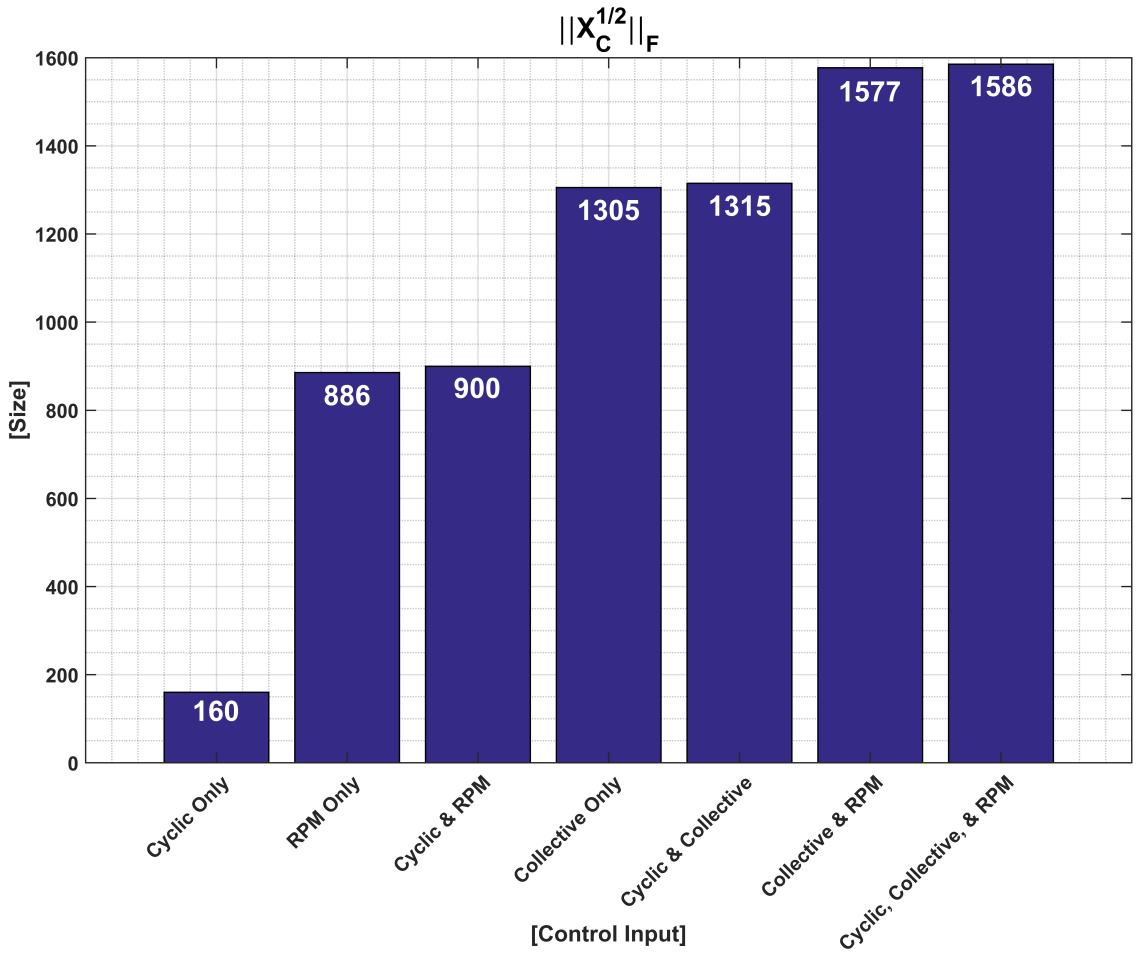

Figure 5.6: Comparison of $\|X_C^{1/2}\|_F$ Values for Each Control Allocation (at 12 lbs., 1680 RPM)

all three mechanisms, collective pitch, cyclic pitch, and RPM control, is considered. While this control allocation method produces the largest size of the reachable set and there is a increase in the size of the reachable set over the collective pitch & RPM control method, the increase may not justify the added complexity.

Figures 5.7 & 5.8 display the values of the determinant and the first Frobenius norm, for each control allocation method, respectively, as a function of RPM. The results show a general increase in the size of the reachable set as RPM increases, with the exception of pure RPM control and RPM plus cyclic pitch control. Because of the battery voltage and limitations with the propulsion system, the vehicle has a maximum RPM limit. As the vehicle hovering

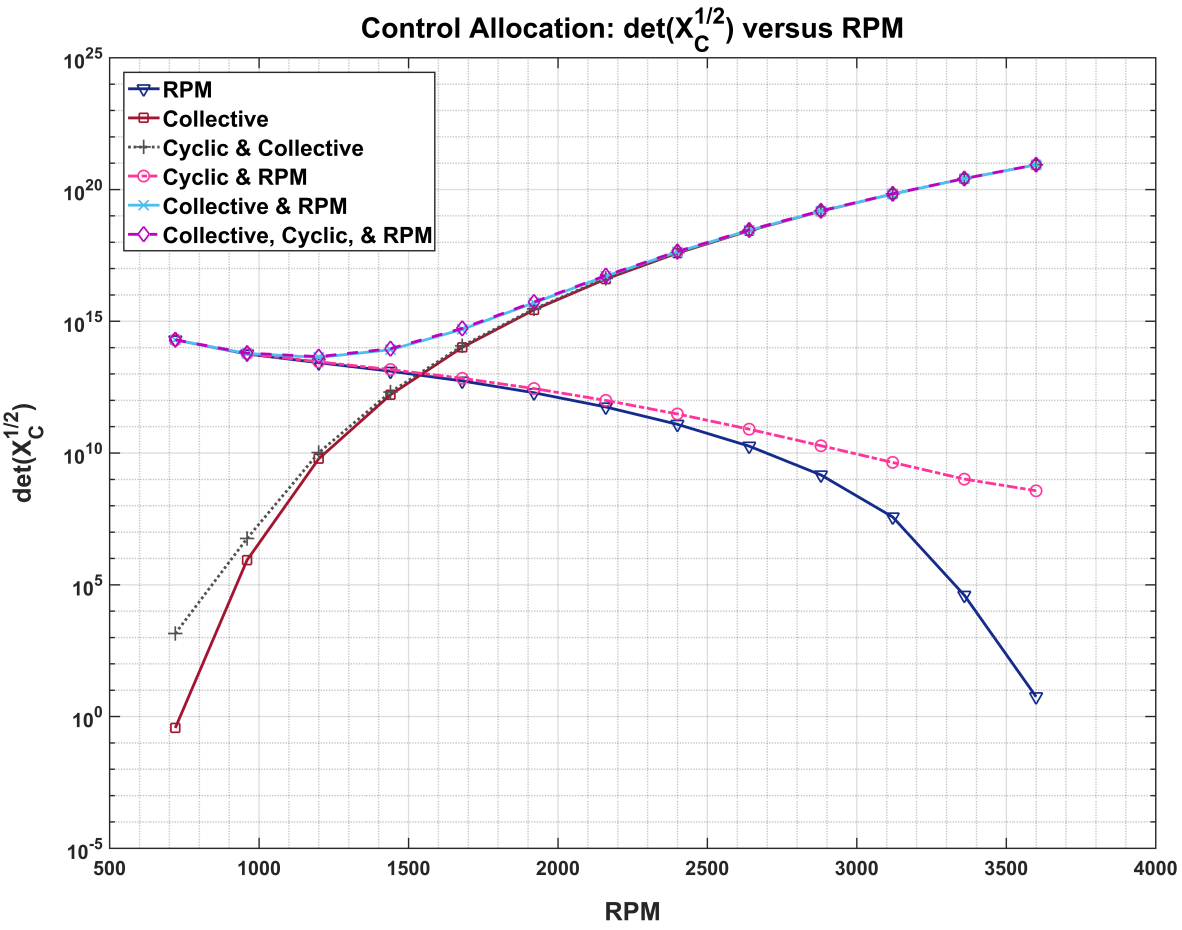

Figure 5.7: $det(X_C^{1/2})$ Values for Each Control Allocation with varying RPM

RPM increases, the RPM control overhead for maneuvering decreases, reducing the size of the reachable set. A similar explanation can be made for why the size of the reachable sets for the collective control methods are reduced at low RPM. As the RPM decreases, the blade angle increases to maintain thrust to trim the vehicle in hover. The maximum blade angle is limited by mechanical and aerodynamic constraints. As the blade angle approach the maximum value, the collective pitch overhead for control is reduced, reducing the size of the reachable set. The combinations of collective pitch and RPM control alleviates some of the degradation in the low RPM range and provides the ability to increase the size of the reachable set at the high RPM range. The collective & RPM control allocation and the collective, cyclic, & RPM control allocation are essentially identical as the addition of cyclic

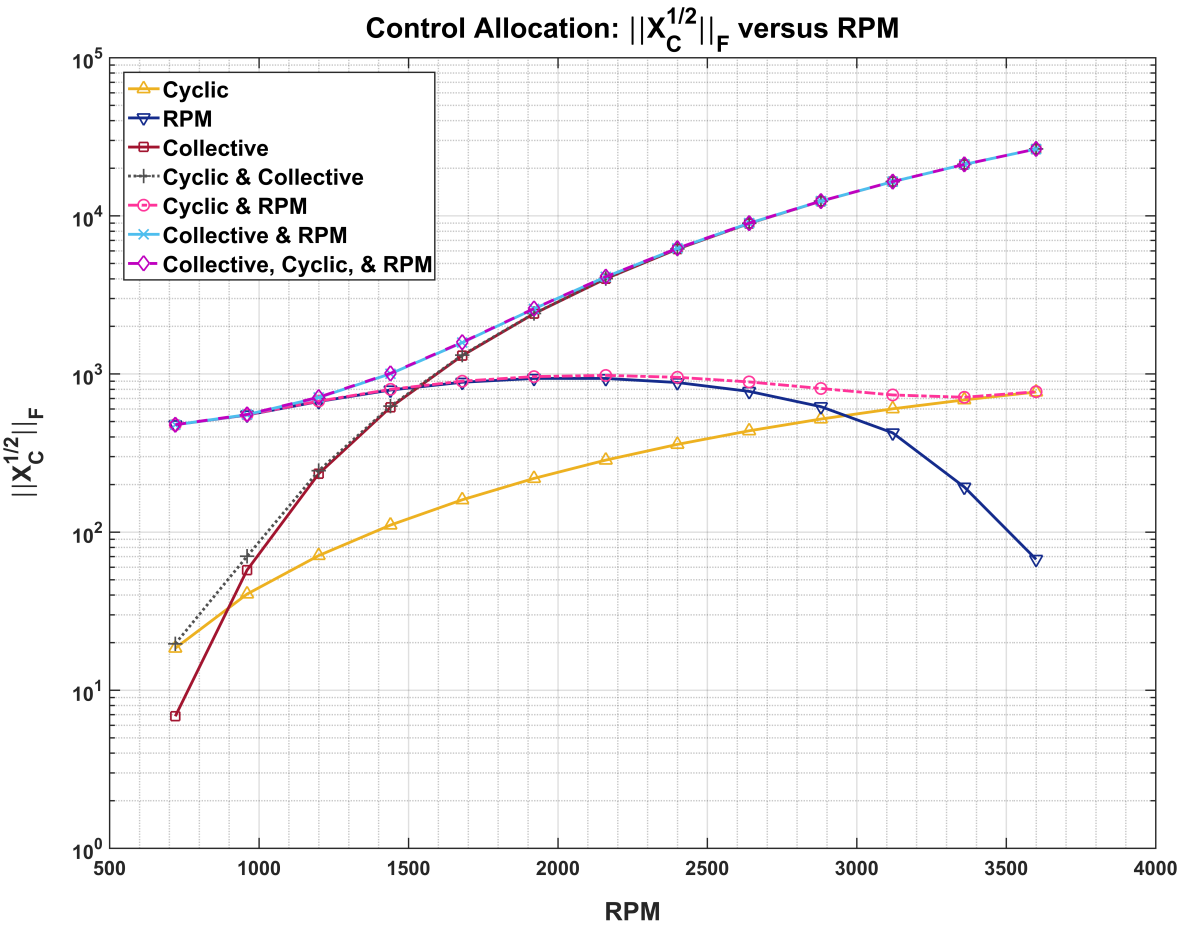

Figure 5.8: $\|X_C^{1/2}\|_F$ Values for Each Control Allocation with varying RPM

pitch control provides only a minor increase in the reachable set, which can be seen in figs. 5.5 & 5.6. Both the determinant and the first Frobenius norm show that between approximately 1200-2400 RPM, the collective & RPM control allocation and the collective, cyclic, & RPM control allocation have an advantage over the other control allocation methods. Above approximately 2200 RPM, the size of the reachable sets, for the strategies using collective pitch control, merge together. If the goal is only to achieve the largest reachable set, above this RPM, there is virtually no advantage to incorporating additional controls methods beyond collective pitch control. The first Frobenius norm also shows that the pure RPM control allocation method has the largest reachable set at approximately 2000 RPM which is close to 50% of the maximum RPM. As discussed previously, it is very common for fixed-

pitch multirotor vehicles to hover at approximately 50% of maximum RPM to leave sufficient RPM overhead for control. These results may show that this is, in fact, the optimum setup. for the RPM control allocation, to obtain the largest reachable set, although this has not be experimentally verified. For any control allocation method using collective and/or cyclic pitch control, the size of the reachable set increases with RPM. This makes sense as the rotor control derivatives, Z_{θ_0} & N_{θ_0}, increase in magnitude with increasing RPM while the trim blade angle, θ_{trim} decreases with RPM, leaving more available overhead for control. This would suggest that a vehicle wanting to maximize the size of the reachable set should be operated at or near the maximum RPM. As an example, aerobatic model helicopters tend to operate in this way. Pilots wanting to perform extreme aerobatic maneuvers often setup the vehicle so the RPM is held near the maximum value and the blade pitch is modulated for the maneuvers. When pilots want to perform more 'gentle' aerobatic maneuvers, the RPM is usually lowered. Operating in this lower RPM regime makes the maneuvers appear more precise, however, this reduces the type of maneuvers that can be performed and the speed at which they are performed. These results seem to confirm this method of operating aerobatic model helicopters. The idea of increasing the size of the reachable set should be balanced against performance and power consumption. While operating the vehicle at the highest RPM increases the size of the reachable set, this may not always result in the lowest power consumption, longest endurance, or longest range. A balance must be found depending on the mission requirements. It seems, a priori, that a reasonable balance between the size of the reachable set and potential reduction in endurance may be found around 50% of maximum RPM.

Interestingly, this analysis displays the benefits of collective and cyclic pitch control without considering control latency. One of the main justifications for the use of collective pitch as opposed to RPM control is the control latency associated with changing RPM. Cutler et al. [53] show that there is a significant reduction in control latency by using blade pitch control as opposed to RPM control. This resulted in reduced tracking error and an expanded

flight envelope because the blades can be actuated to produced negative thrust. The results presented show improvement in the reachable set before these additional benefits are considered.

As mentioned previously, constraints such as reduced mechanical complexity may provide difficulty in quantifying a cost function. The simplest actuation method is the use of RPM control only, however the size of the reachable set is significantly smaller when compared to the more complex method of collective pitch control. While collective pitch control requires a more complex rotor head, the complexity can be reduced by not including cyclic pitch. A simple pitch-change mechanism, such as that used on a conventional tail rotor, can be used. This eliminates the need for a swashplate and reduces the number of servo actuators from 3 to just 1 per rotor. While RPM control is not necessary, it is important to maintain constant RPM during operation. The reduced requirement for high-frequency, individual rotor RPM control would allow possibilities such as a large, single motor used by Pang et al.[3] and Wu[21], more choices of motors & motor controllers, as well as different frame geometries and a potential reduction in the moments of inertia for more agile maneuvering.

Although the addition of cyclic pitch is the most complex, it does provide some notable enhancements. Not only is the reachable set the largest of all the combinations, but the flight envelop is also increased. Considering two distinct failure modes, cyclic pitch can achieve a controllable vehicle where other actuation methods may not. In the context of a quadrotor specifically, if damage to a single rotor were to occur, without cyclic pitch, the vehicle would be uncontrollable. To maintain pitch and roll attitude, the rotor diagonally across from the damaged rotor would need to be actuated to produce zero net thrust. This would, however, cause the vehicle to go into a spin about the vertical axis as the torque of the rotors would no longer be balanced. With the addition of cyclic pitch, the operational rotor that was modulated to produce zero net thrust could still be used to produce a yaw

moment to counter the torque imbalance. The vehicle could then be safely landed, under control, using this now auxiliary rotor for torque balance and supplemental control.

A different failure mode involving simultaneous power failure of all the drive motors would render any actuation method involving RPM control useless. With collective pitch control and cyclic pitch control, the vehicle could enter and autorotation. During autorotation flight, maintaining rotor RPM is critical and this is accomplished through control of collective pitch. Having only collective pitch would likely cause unwanted pitch, roll, and yaw commands while maintaining & adjusting rotor RPM, which could lead to loss of control of the vehicle. An additional complication arises from the use of collective pitch for yaw control. Rotorcraft using differential torque for control, through changes in collective pitch, can have a noticeable reduction in yaw authority when the rotors are lightly loaded. This effect is made worse when the vehicle is in an autorotation as the yaw control reverses. A cursory assessment of rotorcraft that use this method for control will show that these vehicles typically have large vertical stabilizers with controllable rudders due to the reduction of yaw authority in certain operating conditions. A multirotor using only collective pitch would likely encounter this same problem, however, with cyclic pitch control, yaw authority can be maintained through differential cyclic pitch. Collective pitch would be used to maintain rotor RPM while cyclic pitch would be used for attitude and directional control.

The controllability & reachable set analysis presented only addresses the maximum size of the reachable set, but does not account for specific maneuvers or control latency. Gillula et al. [56] addresses the idea of reachable sets in their analysis using a specific 'backflip' maneuver. Their reachable set analysis allows them to design the segments of the maneuver and derive unsafe sets so that they can determine certain vehicle states that would result in a failed maneuver. Applying a similar analysis with the alternative control allocations and specific maneuvers could help to assess optimal control strategies and provide more physical examples of the flight envelop to determine appropriate control allocations. Adding actuator

dynamics would enhance the analysis by further constraining the reachable sets and flight envelop. It will also be important for future work to include airframe flexible modes in the stability & control allocation analysis. Depending on the structural configuration of the airframe, certain control methods may prove to be more optimal when the structure is not assumed to be rigid.

This work explores the stability & control allocation of a multirotor vehicle with cyclic and collective-pitch control. While a major benefit of a conventional multirotor is the mechanical simplicity, additional methods of actuation can enhance the control of the vehicle and expand the flight envelope. The overall stability & control of the configuration is similar to a large, conventional multirotor, however when comparing the volume of the reachable sets of each control allocation method, there is a noticeable increase in the volume of the reachable sets where collective and cyclic-pitch control is employed. From a vehicle with pure RPM control, adding collective-pitch control significantly increases the volume of the reachable set. Subsequent addition of actuation methods yields a benefit, although the increase in size of the reachable set is less significant. These benefits are realized even before taking into account the control latency inherent to each control method. The cost of the added complexity is not directly quantifiable, however, qualitatively, it could be argued that the additional complexity can increase the robustness of the vehicle and expand the flight envelope. The requirements of the vehicle would direct this conclusion. If the goal is to reduce the number of actuators while increasing the volume of the reachable set, the likely conclusion would be using collective pitch and a simple pitch-change mechanism. This may also provide some vibration benefits when compared with the more complex system using cyclic pitch control.

The presented analysis is modelled around the hovering flight condition. This was chosen for ease of analysis and because the flight test data was largely acquired during hovering flight. Forward flight may bring about additional phenomena that would impact stability, control, and vibration. Changes to the stability and control derivatives are necessary to

account for forward flight. The airframe aerodynamics should also be estimated and incorporated if the proposed effect would be significant. More aggressive flight testing will certainly show additional issues that need to be addressed for vehicle robustness. Further work on this project should start with experimental validation of the stability and control derivatives of the vehicle as these values are integral to the vibration characteristics, the ability to utilize active vibration attenuation, and the conclusion of the control analysis. The stability and control derivatives are sensitive to numerous parameters making it difficult to completely validate the predicted values based on estimated geometries. Extensions to the complete vehicle bring additional uncertainties with aircraft geometry, flexible dynamics, mass properties, and aerodynamics. Non-linearities such as the blade section drag versus alpha, C_{d_α} should be considered for the methods of control. Better estimates of the control derivatives will enhance the comparison of the proposed control methods and provide better recommendations for future aircraft.

Chapter 6

Future Work

6.1 Control Validation & Forward Flight

Further work on this project should start with experimental validation of the stability & control derivatives for the vehicle. The values are integral to the vibration characteristics, the ability to utilize active vibration attenuation, and the assessment of the vehicle stability & control allocation. The stability and control derivatives are sensitive to numerous parameters making it difficult to completely validate the predicted values based on estimated geometries. Extensions to the complete vehicle bring additional uncertainties with aircraft geometry, flexible dynamics, aerodynamics, and mass properties. Non-linearities such as the variation of blade section drag with changes in alpha, C_{d_α}, should be considered for performance and control. Better estimates of the control derivatives will enhance the comparison of the proposed control allocations and provide better recommendations for future aircraft. The controllability & reachable set analysis presented only addresses the maximum size of the reachable set, but does not account for specific maneuvers or control latency. Gillula et al. [56] addresses the idea of reachable sets in their analysis using a specific 'backflip' maneuver.

The reachable set analysis performed allows them to design the segments of the maneuver and derive unsafe sets so that they can determine certain vehicle states that would result in a failed maneuver. Applying a similar analysis with the alternative control allocations and specific maneuvers could help to assess optimal control strategies and provide more physical examples of the flight envelop to determine appropriate control allocations. Adding actuator dynamics would enhance the analysis by further constraining the reachable sets and flight envelope. It will also be important for future work to include airframe flexible modes in the stability & control analysis. Depending on the structural configuration of the airframe, certain control allocation methods may prove to be more optimal when the structure is not assumed to be rigid. The presented analysis is modelled around the hovering flight condition. This was chosen for ease of analysis and because the flight test data was largely acquired during hovering flight. Forward flight may bring about additional phenomena that may impact stability, control, and vibration. Additional terms and derivatives of the stability & control derivatives are necessary to account for forward flight. The airframe aerodynamics should also be estimated and incorporated if the proposed effects would be significant, such as lift, drag, and moments of the airframe. More aggressive flight testing will certainly show additional issues the need to be addressed for vehicle robustness.

6.2 Frame Design & Rotorhead

With knowledge gained through flight testing and vibration analysis, some frame design changes are proposed. From the first frame design to the current frame design, vibration characteristic were driving the design to have longer strut braces and the addition of lateral braces. As mentioned in previously, this seemed to be a common trend when researching variable-pitch multirotor vehicles. Most multirotor vehicles have a planar design and cantilever appendages. The strut braces and lateral braces can mitigate in-plane bending

compliance for the appendages, however these braces will only provide a minor effect for out-of-plane bending modes. While the out-of-plane bending modes have higher damping and seem to be less prone to damage, it is still possible for these modes to be problematic. It was argued that certain control allocation arrangements using collective pitch for roll, pitch, and yaw may have the potential to excite the low-frequency fuselage torsional mode. To combat this tendency, a proposed frame design would incorporate a 3D-space frame and truss-like structures for the arm appendages and fuselage. A tentative example is shown in fig. 6.1. By first modifying the fuselage frame to have substantial thickness or structural components vertically out of the plane, the arm appendage strut braces could be connected to the fuselage at the top or bottom of the fuselage, bring the attachment point out of the plane. Figure 4.22c from Wu [21] shows a similar arrangement. This would provide some bracing of the out-of-plane modes in addition to the in-plane bending mode of the arms. Developing the fuselage and arm appendages as truss structures would offer potential benefits in terms of stiffness and the ability to tune the frequency response. This, however, should be balanced against increases in weight, down-load from the rotor wash, complexity, and manufacturability.

The 3-bladed rotor head was chosen for vibration characteristics. Because vibrations from the main rotor are generally dominated by the RPM and $N \cdot RPM$, 2-bladed rotor systems can have high vibrations at $1 \cdot RPM$ and $2 \cdot RPM$, both of which are at lower frequencies and prone to exciting the airframe resonant frequencies. Higher blade count can help to reduce the high-energy vibrations at low frequencies. This should be balanced against overall rotor performance as more blades can effect the rotor power. Unfortunately, there are limited choices for off-the-shelf rotor head components in this size of aircraft. It is possible to find 'scale' rotor heads with 4, 5, and possibly 6 blades. A 5-bladed rotor system would have an advantage of vibration energy being prominent at $1 \cdot RPM$ and $5 \cdot RPM$. For this aircraft, $5 \cdot RPM$ would likely be well above of the troublesome structural resonant frequencies. Additionally, different blade counts can produce different acoustic signatures.

Figure 6.1: Example 3D space frame

A noise requirement in the design may also warrant different blade counts. Higher blades counts, however, have challenges with mechanical complexity, blade tracking, and obtaining balanced sets of blades. The 3-blades rotor heads of the current configuration were more challenging to set up and maintain versus the more common 2-bladed rotor heads found on most model helicopters. While a 3-bladed system was chosen to help mitigate low-frequency vibrations, it is not clear if the impact was positive or negative to the overall system. This particular rotor head design lacked stiffness that is typically found in these small model helicopter rotors. Even though a 2-bladed rotor can suffer from vibration as $2 \cdot RPM$, the stiffness of the feathering shaft connection through the rotor head would likely change the vibration characteristics and may be more beneficial to the overall system. As discussed in section 3.3, during flight testing, the blades chosen may have complicated the vibration issues from a stiffness and balance standpoint. It is easy to find a variety of blades for 2-bladed systems that are matched to each other. As the number of blades increases, the choices of blades rapidly diminishes and the likelihood of having out-of-balance blades increases significantly. If cost is a major consideration, higher blade counts will increase the

cost. From communications with Pang [57], the vehicle described in chapter 1 did have a successful flight with 2-bladed rotor heads. It is recommended to test a 2-bladed system and assess the vibration deficiencies prior to increasing the blade count.

6.3 Vibration Attenuation

To implement the active vibration attenuation described in Chapter 4, the flight control architecture must be redesigned. The test vehicle is currently limited by the number of output channels from the Pixhawk 2.1 flight controller. The throttle signal is fed through directly from the receiver to the motor controller and an internal governor maintains RPM. Control over vehicle RPM from the flight controller is recommended for vibration considerations and expanded flight envelope operations. For autorotation flight, the RPM will be a critical value to monitor. Most electronic speed controllers monitor RPM while the motor is powered, however, since the rotor disengages from the main drive gear though a one-way bearing or sprag clutch during autorotation, the RPM should be measure directly through the main shaft or other drive train components, such as a gear/pulley, that has a direct connection to the main shaft. For both characterization of vibrations during testing and to implement active vibration attenuation methods, accelerometers should be installed on critical points on the frame. An accelerometer at the end of each arm appendage as well as locations along the fuselage would allow local vibrations to be measured. During testing, this data could be stored and later reduced to validate FEA predictions and the physics model. During flight, this information would be passed to a microcontroller that would characterize the vibrations and decide what action should be taken to mitigate airframe vibration modes that are at risk, depending on the flight phase. This information could be fed to the flight controller which would then output a command to the actuators or the flight controller output (without vibration attenuation compensation) could be sent to the micro-controller

which would combine the recommend disturbance rejection command with the flight control command, directly to the actuators. Considerations of actuator bandwidth, flight control & microcontroller sampling rate will be critical to active vibration attenuation. Because of the possible bandwidth limitations of active vibration attenuation, a possible alternative is a hybrid active-passive system. This hybrid system may provide a unique alternative where a passive spring-damper unit could be adjusted by an actuator to tune the operation to problem frequencies. This would also likely reduce the bandwidth requirements on the actuator because tuning the passive element can occur at a lower frequency than providing active damping through the rotor. These active-passive systems can be mechanical springs and dampers that are adjusted by an actuator or by using a geared brushless motor to apply damping by modulating the motor controller through a process similar to 'regenerative braking'.

6.4 Autorotation

Another promising aspect of this multirotor configuration is the ability for the vehicle to autorotate in the event of main propulsion power loss. Initial research would suggest that the vehicle will need cyclic and collective pitch to operate in this flight regime, which would be a distinguishing feature of this configuration. Although low level autorotation landings have been performed, the vehicle control system will need to be modified to perform higher altitude autorotation descents. In an autorotation, the pilot must carefully modulate the collective pitch to first enter the autorotation, then to control the decent rate, and finally to perform the flare just prior to landing. The pilot has full control of the vehicle using cyclic and collective pitch and the vehicle can continue to autorotate as long as potential energy can be traded for energy in the blades and keeping the RPM within safe limits. The blade angle changes the driving and driven regions on the blade which are the regions of autoro-

tative forces and retarding forces, respectively. This is described in more detail in [30]. The importance of modulating the collective pitch leads to potential concerns regarding the sole use of collective pitch for control during a multirotor autorotation. The necessity of large or abrupt control inputs may be limited by and/or reduce the rotor RPMs, which could lead to loss of control. The addition of cyclic pitch control may be the only means to perform a controlled autorotation. As Prouty [38] discusses, coaxial helicopters use differential collective pitch, to control yaw, much like the proposed methods for the variable-collective pitch multirotor configurations. Prouty goes on to say that while "differential collective pitch works well in powered flight... in autorotation, however, differential collective pitch has the opposite [control] effect." Prouty provides an anecdote related to this. According to Prouty, during the first autorotation test that Stanley Hiller performed with his first helicopter, a coaxial configuration, the helicopter began spinning and was not controllable, even though the pilot was providing what they thought were the 'correct' inputs. "As he approached the ground, he decided he had nothing to lose by reversing control—and it worked." [38] Amer and Gustafson confirm this in their research in which they state, "[t]he charts confirm the reduction or reversal of yawing control which is understood to be encountered in low-powered flight and autorotation in coaxial and synchropter-type helicopters when differential torque, as obtained by means of differential collective pitch, is employed as the only source of yawing control." [58] This gives reason to believe the same issue would be encountered in a configuration with only variable collective-pitch rotors. This is counter to the patent claim by Gonzalez et al. [33] that suggests collective pitch control, alone, would be sufficient, for a multirotor, during autorotation. This should be carefully evaluated. In addition to the possible increases in control, during forward flight, Prouty discusses how a tandem rotor configuration with only different collective pitch has undesirable trim behavior. The rotor blades want to flap back with forward airspeed requiring large body angles to trim and higher drag. By incorporating cyclic pitch, the vehicle can trim with reduced body angles. Increased control of the body angle would have aerodynamic benefits as well as benefits to

payloads and mission objectives. This is an aside but another benefit of incorporating cyclic pitch. While expanded flight envelope testing is an area of research that is very interesting, it is also one of the most difficult and potentially hazardous. To validate the predictions and claims, flight testing of the full configuration would ultimately be necessary. A prudent approach would be to begin with analytical predictions and computational methods to first explore any unforeseen behavior that could result in loss of the vehicle. A subscale wind-tunnel model would be an intermediate step to validate predictions and explore the vehicle behavior in the autorotation regime. This vehicle would need to be powered and have full cyclic-collective mechanics for each rotor. The subscale vehicle would likely introduce scaling issues specifically with blade Lock number, inertia, and Reynolds number effects. Even a half scale vehicle would require a test section greater than 3ft x 3ft. This may pose a significant challenge to this experimental method. While numerical simulations would possibly provide critical data with regards to the behavior of the vehicle, it is also difficult and time expensive. Ultimately, the proof of flight in this regime would provide a significant benefit for considering the additional complexity of this configuration.

6.5 Conclusion

Summary of Vehicle Features

1. Benefits
    - Unusual attitudes
    - Autorotation
    - Reduced control latency
    - Expanded reachable set/reduced control power
    - Gust alleviation and vibration attenuation

2. Challenges

    - Unproven configuration
    - Mechanically complex
    - Airframe vibrations
    - Control allocation

Exploration of new vehicle designs can lead to unique control schemes and the ability to widen the operational envelope. The new multirotor vehicle design explored in this research shows feasibility of this type of configuration, but also presents significant challenges that need to be addressed. The most significant challenge is the rotor-frame interaction and resulting vibrations. These vibrations caused multiple, catastrophic failures in the vehicle structure. In addition to the frame design, the rotor configuration has a significant impact on the frame vibration characteristics. In the current research, structural members were changed, and structural members were added to stiffen the vehicle as damage occurred. The additions were added to eliminate the modes of vibrations and increase the natural frequencies of the frame harmonics however, the addition of these structural members has decreased the overall performance of the vehicle. A reduction in aerodynamic damping combined with a frame that is stiffer may cause excess vibrations to be transferred to the flight controller and impact the ability to tune the system gains and impacts the vehicle stability. Finite element analysis in addition to a aerodynamic-structural coupled physics model allows the assessment of the resonant frequencies of the airframe and the impact of the aerodynamic damping on the vibration transmissibility. The study suggests that the in-plane bending modes of the arms and fuselage are more susceptible to vibration damage due to lower aerodynamic damping. While the airframe should be tailored to move resonant frequencies away from known sources of vibrational energy, if a vehicle requirement is to operate at different RPMs, this would not be feasible for every flight condition. The ability to attenuate vibration would be critical. This over-actuated configuration may allow

the implementation of active vibration attenuation by modulating the cyclic and collective pitch, at high frequencies, to modify the vibrations that are transferred, from the rotors, through the airframe. This would have some analogies to studies on Higher Harmonic Control for conventional rotor craft. Active vibration attenuation combined with passive methods such as vibration dampers incorporated into fuselage structural members would decrease the susceptibility of vibration damage and make this configuration more robust. A robust vehicle can expand the flight envelope and explore flight regimes typically off limits to most conventional multirotor vehicles.

Assessment of the stability & control allocation of the vehicles shows that additional methods of actuation can enhance the control of the vehicle and expand the flight envelope. The overall stability & control of the configuration is similar to a large, conventional multirotor, however when comparing the volume of the reachable sets of each control allocation method, there is a noticeable increase in the volume of the reachable sets where collective and cyclic-pitch control is employed. Adding collective-pitch control significantly increases the volume of the reachable set from using RPM control as the sole method. These benefits are realized even before taking into account the control latency inherent to each control method. While fixed-pitch multirotor vehicles have a significant benefit in terms of mechanical simplicity, it could be argued that the additional complexity can increase the robustness of the vehicle and expand the flight envelope.

Even though this configuration has unique challenges relating to the unconventional design, there are potential benefits that could make this a viable commercial design for future eVTOL aircraft. The valuable lessons learned in this study can help build intuition for the future of Urban Air Mobility.

Figure 6.2: Colin Sledge with the Test Vehicle

Bibliography

[1] Frank N. Piasecki and Donald N. Meyers. Multiple helicopter lift system, apr 1972.

[2] C. Venkatesan and P. P. Friedmann. Aeromechanical stability analysis of a hybrid heavy lift multirotor vehicle in hover. *Journal of Aircraft*, 22(11):965–972, nov 1985.

[3] Tao Pang, Kemao Peng, Feng Lin, and Ben M. Chen. Towards long-endurance flight: Design and implementation of a variable-pitch gasoline-engine quadrotor. In *2016 12th IEEE International Conference on Control and Automation (ICCA)*. IEEE, jun 2016.

[4] Dario Brescianini and Raffaello D'Andrea. An omni-directional multirotor vehicle. *Mechatronics*, 55:76–93, nov 2018.

[5] Ali Junaid, Alejandro Sanchez, Javier Bosch, Nikolaos Vitzilaios, and Yahya Zweiri. Design and implementation of a dual-axis tilting quadcopter. *Robotics*, 7(4):65, oct 2018.

[6] Admin. Stingray 500 – cj youngblood ent., apr 2016.

[7] Robert K. Heffley, Wayne F. Jewell, John M. Lehman, and Richard A. Van Winkle. A compilation and analysis of helicopter handling qualities data, volume one: Data compilation, aug 1979.

[8] Rock West Composites. Rock west composites - engineered carbon fiber, fiberglass & kevlar, 2021.

[9] LLC. Clearwater Composites. Properties of carbon fiber, 2017.

[10] Performance Composites Ltd. Mechanical properties of carbon fibre composite materials, 2009.

[11] Frank N. Piasecki. Helicopter and balloon aircraft unit, nov 1961.

[12] Frank N. Piasecki and Donald N. Meyers. Vectored thrust airship, may 1986.

[13] National Transportation Safety Board. Nyc86fhd01: Pa-97 helistat accident, july 1, 1986 in lakehurst, nj.

[14] W. BREWER. Structural response of the heavy lift airship /HLA/ to dynamic application of collective pitch. In *2nd Lighter Than Air Systems Technology Conference*. American Institute of Aeronautics and Astronautics, aug 1977.

[15] Ronald G.E. Browning. A preliminary design study of a hybrid airship for flight research, jul 1981.

[16] C. Venkatesan and P. Friedmann. Aeroelastic effects in multi-rotor vehicles with application to a hybrid heavy lift system, part i: Formulation of equations of motion, aug 1984.

[17] C. Venkatesan and P. Friedmann. Aeroelastic effects in multirotor vehicles, part ii: Methods of solution and results illustrating coupled rotor/body aeromechanical stability, feb 1987.

[18] Johann Borenstein. The hoverbot - an electrically powered flying robot, 1992.

[19] Colin A. Sledge, Haitham E. Taha, and Robert H. Liebeck. Design and flight testing of a multirotor vehicle with cyclic-collective pitch control. In *AIAA Scitech 2021 Forum*. American Institute of Aeronautics and Astronautics, jan 2021.

[20] Tao Pang. Design, prototyping and autonomous control of gasoline-engine variable-pitch quadcopter. Master's thesis, may 2016.

[21] Xiaonan Wu. Design and development of variable pitch quadcopter for long endurance flight. Master's thesis, Oklahoma State University, may 2018.

[22] Mark Cutler. Design and Control of an Autonomous Variable-Pitch Quadrotor Helicopter. Master's thesis, Massachusetts Institute of Technology, Department of Aeronautics and Astronautics, aug 2012.

[23] MIT Aerospace Controls Lab. Mit acl - variable pitch quadrotor, jul 2011.

[24] Robert Porter, Bijan Shirinzadeh, and Man Ho Choi. Experimental analysis of variable collective-pitch rotor systems for multirotor helicopter applications. *Journal of Intelligent & Robotic Systems*, 83(2):271–288, nov 2015.

[25] Bill Crowther, Alexander Lanzon, Martin Maya-Gonzalez, and David Langkamp. Kinematic analysis and control design for a nonplanar multirotor vehicle. *Journal of Guidance, Control, and Dynamics*, 34(4):1157–1171, jul 2011.

[26] Svein Rivli Napsholm and Skavhaug Amund. Prototype of a tilt rotor helicopter: A helicopter comprising a multi-rotor system with individual collective and cyclic pitch control. Master's thesis, apr 2013.

[27] A. Nemati and M. Kumar. Modeling and control of a single axis tilting quadcopter. In *2014 American Control Conference*. IEEE, jun 2014.

[28] Pau Segui-Gasco, Yazan Al-Rihani, Hyo-Sang Shin, and Al Savvaris. A novel actuation concept for a multi rotor UAV. *Journal of Intelligent & Robotic Systems*, 74(1-2):173–191, nov 2013.

[29] Mark W. Mueller and Raffaello D'Andrea. Stability and control of a quadrocopter despite the complete loss of one, two, or three propellers. In *2014 IEEE International Conference on Robotics and Automation (ICRA)*. IEEE, may 2014.

[30] Mark Mueller. Stability and control of a quadrocopter despite the complete loss of one, two, or three propellers, apr 2015.

[31] Alexander Lanzon, Alessandro Freddi, and Sauro Longhi. Flight control of a quadrotor vehicle subsequent to a rotor failure. *Journal of Guidance, Control, and Dynamics*, 37(2):580–591, mar 2014.

[32] Vladimir Kvitnevskiy. Controlling rotary wing aircraft, mar 2016.

[33] Eric R. Gonzalez and Frank B. Stamps. Multirotor aircraft with collective for autorotation, nov 2020.

[34] Roberto Navoni. Hg3 the era of quad variable pitch has begun!, 08 2010.

[35] Drone Dance. Variable pitch quadcopter - autopilot system & upside-down flight, aug 2010.

[36] Mauro Gatti, Fabrizio Giulietti, and Matteo Turci. Maximum endurance for battery-powered rotary-wing aircraft. *Aerospace Science and Technology*, 45:174–179, sep 2015.

[37] Wayne Johnson. *Helicopter theory*. Dover, 1994.

[38] Raymond W Prouty and Shawn Coyle. *Helicopter aerodynamics*, volume II. Eagle Eye Solutions, 2009.

[39] R C Hibbeler. *Mechanics of materials*. Prentice Hall, eighth edition, 2011.

[40] Raymond W Prouty and Shawn Coyle. *Helicopter aerodynamics*. Eagle Eye Solutions, 2009.

[41] William J Palm. *System dynamics*. Mcgraw-Hill Higher Education, 2005.

[42] Gareth D Padfield. *Helicopter Flight Dynamics : The Theory and Application of Flying Qualities and Simulation Modeling*. American Institute Of Aeronautics And Astronautics ; Oxford, Uk, second edition, 2007.

[43] James A. Franklin. V/stol dynamics, control, and flying qualities, oct 2000.

[44] Kathryn B. Hilbert. A mathematical model of the uh-60 helicopter, apr 1984.

[45] Aaron J. Ostroff, David R. Downing, and William J. Rood. A technique using a non-linear helicopter model for determining trims and derivatives, may 1976.

[46] Benton H. Lau, Alexander W. Louie, Nicholas Griffiths, and Costantinos P. Sotiriou. Performance and rotor loads measurements of the lynx xz170 helicopter with rectangular blades, may 1993.

[47] Raymond W Prouty. *Helicopter aerodynamics Volume 3 Ray Prouty's Vertiflite Magazine columns 1990-2013*. Charlotte, Vt Eagle Eye Solutions, Llc, 2016.

[48] Raymond L Bisplinghoff, Holt Ashley, and Robert L Halfman. *Aeroelasticity*. Dover Publications, 1996.

[49] LLC Horizon Hobby. H3050 mid-torq ultra-spd micro heli cyclic servo (spmsh3050): Spektrum - the leader in spread spectrum technology, 2014.

[50] Mario Paz and William Leigh. *Structural Dynamics - Theory and Computation*. Springer Science, fifth edition, 2004.

[51] A R S Bramwell, George Done, and David Balmford. *Bramwell's helicopter dynamics*. American Institute Of Aeronautics And Astronautics ; Jordan Hill, Oxford, Uk, second edition, 2001.

[52] Mark Cutler and Jonathan P. How. Analysis and control of a variable-pitch quadrotor for agile flight. *Journal of Dynamic Systems, Measurement, and Control*, 137(10), jul 2015.

[53] Mark Cutler, Nazim-Kemal Ure, Bernard Michini, and Jonathan How. Comparison of fixed and variable pitch actuators for agile quadrotors. In *AIAA Guidance, Navigation, and Control Conference*. American Institute of Aeronautics and Astronautics, jun 2011.

[54] Robert Niemiec and Farhan Gandhi. Multirotor controls, trim, and autonomous flight dynamics of plus- and cross-quadcopters. *Journal of Aircraft*, 54(5):1910–1920, sep 2017.

[55] J. Sean Humbert and Imraan Faruque. Analysis of insect-inspired wingstroke kinematic perturbations for longitudinal control. *Journal of Guidance, Control, and Dynamics*, 34(2):618–623, mar 2011.

[56] Jeremy H Gillula, Haomiao Huang, Michael P Vitus, and Claire J Tomlin. Design of guaranteed safe maneuvers using reachable sets: Autonomous quadrotor aerobatics in theory and practice. In *2010 IEEE International Conference on Robotics and Automation*. IEEE, may 2010.

[57] Tao Pang. Vibration of gasoline engine-powered quadcopters, jan 2021.

[58] Kenneth B. Amer and F. B. Gustafson. Charts for estimation of longitudinal-stability derivatives for a helicopter rotor in forward flight, 03 1951.

[59] M. B. Tischler and I. L. Ashkenas. Helistat simulation studies, nov 1982.

[60] Usa. Federal Aviation Administration and Usa. Flight Standards Service. *Helicopter flying handbook ; [FAA-H-8083-21A]*. Skyhorse Publ, 2013.

[61] Jan R. Wright and Jonathan E. Cooper. *Introduction to Aircraft Aeroelasticity and Loads*. American Institute Of Aeronautics And Astronautics, Inc, 2007.

[62] Mark B. Tischler, Robert F. Ringland, and Henry R. Jex. Heavy-lift airship dynamics. *Journal of Aircraft*, 20(5):425–433, may 1983.

[63] Rogers Corporation. Materials design: Vibration isolation and damping, the basics, 2012.

[64] William L. Brogan. *Modern Control Theory, Third Edition*. Prentice Hall, 1991.

[65] Pierre-Jean Bristeau, Philippe Martin, Erwan Salaun, and Nicolas Petit. The role of propeller aerodynamics in the model of a quadrotor UAV. In *2009 European Control Conference (ECC)*. IEEE, aug 2009.

[66] Gabriel Hoffmann, Haomiao Huang, Steven Waslander, and Claire Tomlin. Quadrotor helicopter flight dynamics and control: Theory and experiment. In *AIAA Guidance, Navigation and Control Conference and Exhibit*. American Institute of Aeronautics and Astronautics, jun 2007.

[67] R. Ritz, M. Hehn, S. Lupashin, and R. D'Andrea. Quadrocopter performance benchmarking using optimal control. In *2011 IEEE/RSJ International Conference on Intelligent Robots and Systems*. IEEE, sep 2011.

[68] P. Pounds and R. Mahony. Design principles of large quadrotors for practical applications. In *2009 IEEE International Conference on Robotics and Automation*. IEEE, may 2009.

[69] European Rotorcraft Forum. *The role of collective pitch in multi rotor UAV aerodynamics*. University of Manchester, 2010.

[70] Samir Bouabdallah and Roland Siegwart. Full control of a quadrotor. In *2007 IEEE/RSJ International Conference on Intelligent Robots and Systems*. IEEE, oct 2007.